Structural, Chemical, And Electrochemical Evolution of Binary and Ternary Transition Metal Oxides with Enhanced Fe Content: Amorphous Vs. Spinel Oxides for OER Catalysis

Bibisomaia Rezaee

A thesis submitted to the faculty of Graduate Studies in partial fulfillment of the requirement for the degree of Master of Science

GRADUATE PROGRAM IN CHEMISTRY

YORK UNIVERSITY

TORONTO, ONTARIO

JUNE 2025

Abstract

This work investigates the design of electrocatalysts for the oxygen evolution reaction (OER) using binary iron-cobaltites and ternary cobaltites containing Fe, Ni, and/or Cu, all synthesized by thermal decomposition in both the amorphous and spinel phases. The catalysts were characterized by numerous characterization methods to study their structure, composition, and morphology, while their surface area and electrochemical properties were also examined and corrected for the ohmic drop and film surface area. The catalytic activity and OER kinetics were also evaluated. Structural analysis confirmed the successful formation of amorphous and spinel oxides, where for the latter the crystallite sizes were in agreement across techniques. Electron microscopy and composition analysis demonstrated textural differences and stoichiometric consistency, while X-ray photoelectron Spectroscopy revealed distinct surface species and oxidation states. Overall, Fe incorporation enhanced the catalytic activity, whereas Ni-doping reduced the catalyst performance.

Acknowledgement

In the name of Allah, the Most Gracious, the Most Merciful.

First and foremost, I am deeply thankful to **Allah (SWT)** for granting me the strength, patience, and guidance throughout this journey. Without His blessings and mercy, this achievement would not have been possible.

I extremely grateful to my supervisor, **Prof. Sylvie Morin**, for her exceptional guidance, patience, and unwavering support throughout the course of not only this thesis but all my works done at her group. His insight, encouragement, and constructive feedback not only increased the quality of this research but also greatly shaped my growth as a graduate student.

I am also incredibly thankful to the members of my thesis committee, **Prof. Rene Fournier** and **Prof. Jennifer Chen**, for being part of my committee and for their valuable suggestions, critical discussions, and thoughtful questions which contributed meaningfully to the development of this work.

I would like to also express my sincere thanks to my lab colleagues, particularly **Dr. Sreena Thekkoot**, **Dinithi Rajaguru**, **Owen Gray**, and **Tian Jiayue** for their support during my research work. I would like to thank **Magdalena Jaklewicz** at York University, Faculty of Science, Imaging Facility for SEM and EDX measurements; **Victoria Jarvis**, MAX Diffraction Facility, for XRD measurements and pattern analysis; **Dr. Mark Biesinger,** Surface Science Western university, for XPS measurements; **Wajdi Alnoush** and **Dr. Drew Higgins** for TEM measurements, McMaster University. I would like to also thank lab technicians **Ha B. Au** and **Kevin Patel** for their kind support during the times that some instruments were down in our lab.

To my dearest **family**, thank you for being my source of strength and love. **Mom and Dad**, my sister (**Saida**) and my brothers (**Jawad and Hossein**) thank you for your unconditional love, sacrifices, and faith in me. Your support has been my foundation, and I dedicate this accomplishment to you.

To my beloved **husband (Ruhi)**, words will never be enough to express what your support has meant to me. Thank you for standing by me through every challenge, for your patience during the most stressful days, and for always believing in my potential—even when I doubted myself. Your calmness, encouragement, and quiet strength have been my anchor through this journey.

To my precious **son (Parsa)**, your smile gave me hope on the hardest days, and your presence reminded me why this journey mattered. Though you are too little to understand this now, your existence brought meaning to everything I was working toward. You are my greatest inspiration and my proudest reason for finishing what I started.

I would like to thank the **Department of Chemistry and Faculty of Graduate Studies at York University,** which provided me with a stimulating academic environment and access to excellent facilities. I am especially grateful to all my teachers, instructors and mentors at this department specially **Dr. Thomas Baumgartner** and **Dr. Gino Lavoie** for their support and kindness throughout my studies at York. Finally, I would like to thank the Natural Science and Engineering Research Council (**NSERC**) of Canada and Ontario Graduate Scholarship (**OGS**) for their financial support through scholarships and grants respectively awarded to Prof. Morin and this research.

Publications and Presentations

The work described in this thesis is in preparation for publications:

1. S. Thekkoot, B. Rezaee, D. Rajaguru, T. Jiayue, O. Gray, Sylvie Morin, Transition metal oxides for oxygen evolution reaction: A comparative study between amorphous and crystalline materials, manuscript in preparation.
2. B. Rezaee, S. Thekkoot, D. Rajaguru, T. Jiayue, O. Gray, Sylvie Morin, Systematic study of effect of iron in mixed transition metal spinel oxides as oxygen evolution electrocatalysts - electrochemistry and material properties, manuscript in preparation.

This work has also been presented at various conferences in the form of talks and posters and my work was recognized by an award:

1. B. Rezaee, S. Thekkoot, D. Rajaguru, O. Gray, S. Morin, Transition Metal Oxides for Oxygen Evolution Reaction: a Comparative Study Between Amorphous and Crystalline Materials, International Symposium on Electrochemistry and Surface Science in Honour of Professor Jacek Lipkowski's 80th Birthday (ISESS2024), Guelph, August 2024 (oral presentation)
2. B. Rezaee, S. Thekkoot, S. Morin, Transition Metal Oxides for Oxygen Evolution Reaction: a Comparative Study Between Amorphous and Crystalline Materials, 73rd Annual Meeting of International Society of Electrochemistry (ISE), September 2022. (oral presentation)
3. B. Rezaee, S. Thekkoot, O. Gray, T. Jiayue, S. Morin, A Comparative Study Between Amorphous and Crystalline Transition Metal Oxides as Catalysts for the Oxygen Evolution Reaction, 3rd Commonwealth Chemistry Posters, September 2022. (poster was recipient of an award in the Green Chemistry and Catalysis section)
4. B. Rezaee, S. Thekkoot, S. Morin, Characterization and Electrocatalytic Performance of Amorphous Transition Metal Oxides, 24th Chemistry and Biochemistry Graduate Research Conference (CBGRC), November 2021. . (oral presentation)
5. B. Rezaee, S. Thekkoot, S. Morin, Characterization and Electrocatalytic Performance of Amorphous Transition Metal Oxides, ECS Canada Section Fall 2021 Symposium, November 2021. (poster)

Contents

List of Figures

List of Tables

List of Acronyms

GHGs	Green house gasses
IPCC	International panel on climate change
PM	Particulate matter
OER	Oxygen evolution reaction
HER	Hydrogen evolution reaction
RHE	Reversible hydrogen electrode
XPS	X-ray photoelectron spectroscopy
EDX	Energy dispersive x-ray spectroscopy
XRD	X-ray diffraction
TEM	Transmission electron microscopy
SEM	Scanning electron microscopy
EIS	Impedance electron spectroscopy
CV	Cyclic voltammetry
LSV	Linear sweep voltammetry
PMOD	Photochemical metal organic decomposition
XAS	X-ray absorption spectroscopy
BET	Brunauer-Emmett-Teller
SPM	Scanning probe microscopy
AFM	Atomic force microscopy
SCE	Saturated calomel electrode
E	Potential
NIR	Near infrared
FTO	Fluorine-doped tin oxide
BSE	Backscattered electrons
UHV	Ultra-high vacuum
HRTEM	High resolution transmission electron microscopy
SAED	Selected area diffraction
CPE	Constant phase element
DFT	Density functional theory

RDS	Rate determining step
RDE	Rotation disk electrode
EPR	Electron paramagnetic resonance spectroscopy

List of Mathematical Symbols

E	Potential
C_{dl}	Double layer capacitance
R_f	Roughness factor
τ	Time constant
R	Resistance
C	Capacitance
I	Current
V	Voltage
Z	Impedance
ω	Radian frequency
f	Frequency
j	Imaginary number
ϕ	Phase angle
λ	Wavelength
θ	Diffraction angle
d	Distance
E_B	Binding energy
E_K	Kinetic energy
CI	Current interrupt
R_s	Solution resistance
R_{ct}	Charge transfer resistance
W	Warburg element
R^2_{adj}	adjusted coefficient of determination

Chapter 1: Introduction

1.1 Water electrolysis a potential candidate for hydrogen production

The over usage of fossil fuels has made a significant contribution to global warming and air pollution, giving rise to profound environmental and health consequences. Fossil fuels release a large amount of carbon dioxide (CO_2) and other greenhouse gases (GHGs) when burned, which trap heat in the Earth's atmosphere. This causes an enhanced greenhouse effect and global temperature rise. According to the Intergovernmental Panel on Climate Change (IPCC), the amount of CO_2 present in atmosphere has risen by over 40% since the pre-industrial era, mainly due to fossil fuel combustion[1]. This warming has come along with increased frequency and severity of extreme weather events, such as heatwaves, droughts, and heavy precipitation, impacting ecosystems and human societies around the globe.

Air pollution from fossil fuel combustion further aggravates these problems. Sulfur dioxide (SO_2), nitrogen oxides (NO_x), and particulate matter (PM) are generated as an outcome of fossil fuel combustion, which contribute to the formation of smog and acid rain. Their negative impacts on both human health and the environment have been reported in many scientific studies. For instance, SO_2 and NO_x can lead to respiratory diseases, cardiovascular problems, and reduced lung function, as well as contribute to the formation of ground-level ozone, which irritates the respiratory system[2]. Furthermore, PM can penetrate deep into the lungs and enter the bloodstream, leading to heightened mortality rates from heart and lung diseases[3]. The interaction between air pollution and climate change is complex, as pollutants can also influence atmospheric processes and feedback mechanisms, further complicating efforts to address these intertwined issues.

While renewable energy sources provide great advantages in cutting down GHGs emissions and toning down climate change, they also bring some challenges. Reliability of sources such as solar and wind is one major issue, which can give rise to unreliable power supply if no energy storage solutions or grid improvements are present. Moreover, the development of renewable energy technologies and their installation also involve considerable usage of resources, and they can have a significant environmental impact. One instance is the impact of wind turbines on local ecosystem. Another one is related to the manufacturing of solar panels that requires rare minerals from great depth of the earth. Furthermore, transitioning to renewable energy systems often requires significant investments and infrastructure changes, which can be economically and logistically challenging for many regions[4]. These factors highlight the complexity of fully addressing global warming and air pollution through renewable energy sources alone, which has led to failure in producing large amounts of green energy required to support the world's needs. This has given rise to a focused attention towards chemical reactions capable of producing and storing energy without CO_2 emission.

Hydrogen gas is more and more being recognized as a promising renewable energy carrier with great potential to contribute to sustainable energy systems globally. It is considered a clean fuel since its main byproduct is water when oxidized in fuel cells. Therefore, hydrogen gas is perceived as an alternative to fossil fuels that are responsible for GHG emissions and air pollution. The versatility of hydrogen gas results in its potential use across different sectors, such as transportation, industry, and power generation, therefore making it a viable pathway to decarbonize various sectors that are traditionally facing many decarbonization challenges[5].

The electrochemical water splitting reaction can produce hydrogen gas, which in fact is the energy stored in the H-H chemical bond. Water electrolysis has various advantages as a hydrogen production method. One important advantage is that it can be directly integrated with renewable energy sources, converting non-steady power (generated by renewable sources) into a storable and transportable form of energy. This capability is specifically important when solar or wind power is used since they do not always produce electricity when demand is there. By storing energy in the form of hydrogen gas, it can be used later to generate electricity during periods of low power output by the renewable sources. Therefore, it improves the reliability and resilience of the power grid (efficiency of 30-40%)[5]. Water electrolysis is scalable as it can be used in the forms of small, distributed units to large, centralized plants. Therefore, it can provide flexibility in the way it is being used, making it suitable for both local and large-scale energy production[6].

Hydrogen gas is perceived as a highly promising alternative fuel for the future, which is currently produced via steam methane reforming process that is accompanied by CO_2 emission[7]. Water electrolysis offers a means to overcome this issue. However, a notable challenge in this process lies in bypassing the significant overpotential associated with the oxygen evolution reaction (OER), which occurs at the anode, while the hydrogen evolution reaction (HER) represents the reduction component at the cathode[7]. Below are the reactions that are taking place in acidic[8] and in alkaline media[9].

Acidic media:

OER: $2H_2O\ (l) \rightarrow O_2\ (g) + 4H^+\ (aq) + 4e^-$ (1.1)

HER: $4H^+\ (aq) + 4e^- \rightarrow 2H_2\ (g)$ (1.2)

Alkaline media:

OER: $4OH^-\ (aq) \rightarrow O2\ (g) + 2H_2O\ (l) + 4e^-$ (1.3)

HER: $4H_2O$ (l) + $4e^-$ → $2H_2$ (g) + $4OH^-$ (aq)   (1.4)

Overall: $2H_2O$ (l) → O_2 (g) + $2H_2$ (g)   (1.5)

In the OER, the formation of the oxygen double bond involves 4 e- and it makes the water electrolysis sluggish and slow[10]. As a result, a high overpotential (> 1.23 V vs. RHE) is needed to activate OER[11]. Overpotential is defined as the potential that a reaction needs to drive at a significant rate beyond its thermodynamic (onset) potential. This potential is usually reported versus Reversible Hydrogen Electrode (RHE) for consistency. In an RHE the potential is directly associated with the pH of the electrolyte solution and the partial pressure of hydrogen gas through the Nernst equation (equation 2.2). Since the potential is pH dependent it is considered a versatile reference for both acidic and alkaline conditions[12].

The high overpotential required to activate OER causes the efficiency of the overall process to be reduced. Therefore, developing a catalyst for OER is of high importance to be able to activate the rate limiting step and to reduce the overpotential. Some general requirements for a good OER catalyst are high electrical conductivity and intrinsic activity, high surface area and porosity, mechanical and chemical stability, low cost and ease of fabrication.

In alkaline solution the OER pathway is identified as the following steps:

M + OH^- → MOH + e^- (1.6)

MOH + OH^- → MO + H_2O + e^- (1.7)

2MO → 2M + O_2 (1.8)

MO + OH^- → MOOH + e^- (1.9)

MOOH + OH^- → M + H_2O + O_2 + e^- (1.10)[13]

where ''M'' represents the active site on the surface of the catalyst. In general, the rate limiting step depends on the material however reaction 1.10 has been identified as the common rate limiting step in the literature[13]. It should be noted that the reaction 1.8 only take place at high MO coverage where the rate of OER is low. At higher rate, where the MO coverage is low, there would be a slim chance of two MO species to be present close to each other[13].

To date, catalysts for the OER have mainly comprised precious metal oxides, such as iridium (utilized in both acidic and alkaline media) and ruthenium (utilized in acidic media mainly) oxides. Although, the industrial utilization of these catalysts for mass production remains unrealistic due to their scarcity and high costs[14], extensive research efforts have been dedicated to identifying alternative 3d transition metals that are abundant and low-priced. Among the various candidates, cobalt, iron, and nickel oxides have demonstrated remarkable efficiency owing to their capacity to transition between different valence states[15]. The Morin research group, for instance, has previously synthesized ternary and binary spinel oxides involving these transition metals and investigated their catalytic properties under alkaline conditions[16]. However, transition metal oxide can mostly be stable in alkaline media and their deployment requires other technological advances, such as the development of stable ion-conducting membranes.

1.2 Review of prior research

In the Morin group, multiple binary and ternary compositions containing cobalt, nickel, copper, and iron ($Cu_xCo_{3-x}O_4$ ($0 \leq x \leq 1$), $Ni_{1-x}Cu_xCo_2O_4$ ($0 \leq x \leq 0.75$), $Fe_yCu_{x-y}Co_{3-x}O_4$ ($x = 1, 0.5$), ($y = 0.1, 0.15$), $Fe_yNi_{x-y}Co_{3-x}O_4$ ($x = 1, 0.5$), ($y = 0.1, 0.15$)) have been synthesized through thermal decomposition method and have been characterized[16,17]. The surface compositions of these metal oxides have been investigated by XPS. The X-ray photoelectron spectroscopy led to an unusual observation, which showed that the composition of the surface differs from that of the bulk material. Moreover, the surface composition does not show a pure spinel structure and contains other phases while the major phase remains to be spinel.[17]

Table 1. Stoichiometric, bulk and surface compositions for different samples of spinel oxides

Number	Stoichiometric composition	Bulk composition	Surface composition
1	$NiCo_2O_4$	$Ni_{0.99}Co_{1.99}O_4$	$Ni_{1.95}Co_{1.05}O_4$
2	$Ni_{0.95}Cu_{0.05}Co_2O_4$	$Ni_{0.95}Cu_{0.05}Co_{2.06}O_4$	$Ni_{0.86}Co_{2.13}O_4$
3	$Ni_{0.9}Cu_{0.1}Co_2O_4$	$Ni_{0.91}Cu_{0.06}Co_{2.12}O_4$	$Ni_{0.90}Cu_{0.24}Co_{1.83}O_4$
4	$Ni_{0.75}Cu_{0.25}Co_2O_4$	$Ni_{0.74}Cu_{0.22}Co_{2.12}O_4$	$Ni_{0.48}Cu_{0.30}Co_{2.22}O_4$
5	$Ni_{0.5}Cu_{0.5}Co_2O_4$	$Ni_{0.48}Cu_{0.29}Co_{2.24}O_4$	$Ni_{0.96}Cu_{0.72}Co_{1.33}O_4$
6	$Ni_{0.25}Cu_{0.75}Co_2O_4$	$Ni_{0.29}Cu_{0.55}Co_{2.3}O_4$	$Ni_{0.30}Cu_{0.90}Co_{1.77}O_4$
7	$CuCo_2O_4$	$Cu_{1.11}Co_{1.89}O_4$	$Cu_{1.47}Co_{1.52}O_4$
8	$Cu_{0.9}Fe_{0.1}Co_2O_4$	$Fe_{0.22}Cu_{0.41}Co_{2.35}O_4$	$Fe_{0.0}Cu_{1.37}Co_{1.63}O_4$
9	$Fe_{0.15}Cu_{0.35}Co_{2.5}O_4$	$Fe_{0.21}Cu_{0.13}Co_{2.61}O_4$	$Fe_{0.0}Cu_{0.57}Co_{2.43}O_4$

Table 1 shows the stoichiometric composition, bulk composition (obtained from EDX), and surface compositions (obtained from XPS) of the spinel oxides. For almost all the compositions studied the amount of cobalt in the bulk is more than the stoichiometric value. The amount of cobalt at the surface is less than the stoichiometric for most of the oxides prepared or very similar to the stoichiometric value. According to the table, copper is present less in the bulk of the sample and more at the surface. Nickel follows the opposite trend, which is more abundant in the bulk and less at the surface. Surprisingly, no iron was detected at the surface[18].

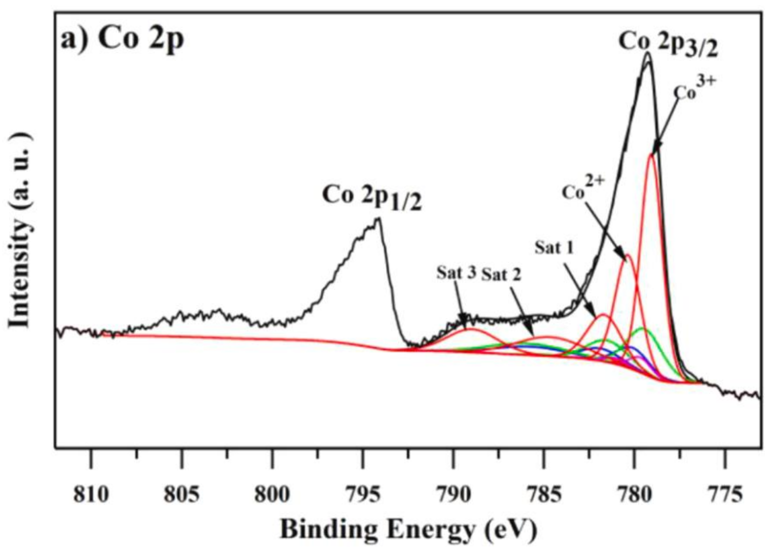

Figure 1. Core level spectrum of Co $2p_{3/2}$ in composition of $Ni_{0.5}Cu_{0.5}Co_2O_4$ (adapted from ref.16)

According to the XPS spectrum of cobalt in figure 1, the analyzed peaks represent different phases and different valences of cations of the metal being present in the sample. Cobalt has peaks at 779.4 eV and 780.7 eV, which corresponds to Co^{3+} and Co^{2+}, respectively. Their ratio was computed to be 0.92 while a stoichiometric ratio of 0.5 was calculated for these cations due to occupying one eighth of a tetrahedral site by Co^{2+} and one half of an octahedral site by Co^{3+} in general definition of a spinel structure. This higher ratio can indicate that Co^{2+} is also occupying octahedral site which further improves the electron transfer between different cations and conductivity[16].

1.3 Structure of the thesis

Due to the differences observed between the bulk and surface compositions and inconsistencies with the composition of a pure spinel oxides, we hypothesized that the surface of the materials may be amorphous. Moreover, another hypothesis concerns the role of iron in increasing the OER current density. The addition of larger amounts of Fe may further enhance the properties of these electrocatalytic materials for the OER. It has been observed that incorporating Fe into binary compositions such as CuCo or NiCo – to form $Fe_yCu_{x-y}Co_{3-x}O_4$ and $Fe_yNi_{x-y}Co_{3-x}O_4$ (for y = 0.1 or 0.15 and x = 1 or 0.5), led to improve catalytic performance [17].

Hence, the objective of this research is to investigate the proposed hypotheses through preparing and characterizing iron rich amorphous and spinel metal oxides as thin films. For this purpose, various novel binary and ternary compositions of amorphous and spinel cobalt-rich oxides were prepared ($Cu_{0.5}Fe_{0.5}Co_2O_4$, $Ni_{0.5}Fe_{0.5}Co_2O_4$, $Fe_{0.5}Co_{2.5}O_4$, $Cu_{0.5}Fe_{0.5}Co_2O_x$, $Fe_{0.5}Co_{2.5}O_x$, $Cu_{0.5}Fe_{0.5}Co_2O_x$) and characterized by X-ray diffraction (XRD), energy dispersive X-ray spectroscopy (EDXS), transmission electron spectroscopy (TEM), X-ray photoelectron spectroscopy (XPS), and scanning electron microscopy (SEM) to confirm their amorphous/crystalline nature, their stochiometric compositions and to determine the surface morphology for these metal oxides. Moreover, to investigate their catalytic properties cyclic voltammetry, impedance electron spectroscopy (EIS), Tafel slope analysis, and differential capacitance measurements were conducted. The results of surface characterization and electrochemical performances of the amorphous cobalt oxides were compared to the results obtained for spinel materials of the same composition.

This thesis is presented in five chapters. Chapter 1 is the introduction and discusses the air pollution and global warming and why it is important to take action to remediate them. It also talks about the hydrogen being viewed as a potential energy carrier in the future. Downsides of renewable energy sources and advantages of water electrolysis are the next topics in this chapter. Moreover, it has a review on the prior research being conducted in Prof. Morin's group.

Chapter 2 discusses the background context and theoretical framework. It includes an overview of literature on amorphous oxides, their preparation methods and their catalytic performance. It also includes an introduction to spinel materials and their electrocatalytic activity. Next, it reviews the ways to measure the surface of the electrode which include cyclic voltammetry (CV), impedance electron spectroscopy (EIS) and linear sweep voltammetry (LSV). It moves on to talk about the method and background of CV, EIS and LSV.

Chapter 3 presents the experimental techniques. This includes presentations of the fundamentals and instrumentation of the characterization techniques that are used in this research. Chapter 4 shows the results and discussion. It is divided into 3 sub-chapters that discuss the physical, chemical and electrochemical characterization of the materials and their electrocatalytic properties, respectively. Chapter 5 summarized the significant outcomes of the research and highlights the future pathway for the research.

1.4 References:

(1) Intergovernmental Panel on Climate Change. *Climate Change 2021: The Physical Science Basis*. Intergovernmental Panel on Climate Change. https://doi.org/10.4324/9781315071961-11.

(2) World Health Organization. *Ambient (outdoor) air pollution*. World Health Organisation Geneva. https://www.who.int/news-room/fact-sheets/detail/ambient-(outdoor)-air-quality-and-health (accessed 2024-08-23).

(3) Pope, C. A.; Dockery, D. W. Health Effects of Fine Particulate Air Pollution: Lines That Connect. *J Air Waste Manage Assoc* **2006**, *56* (6), 709–742. https://doi.org/10.1080/10473289.2006.10464485.

(4) Stokes, L. C. The Politics of Renewable Energy Policies: The Case of Feed-in Tariffs in Ontario, Canada. *Energy Policy* **2013**, *56*, 490–500. https://doi.org/10.1016/j.enpol.2013.01.009.

(5) Staffell, I.; Scamman, D.; Velazquez Abad, A.; Balcombe, P.; Dodds, P. E.; Ekins, P.; Shah, N.; Ward, K. R. The Role of Hydrogen and Fuel Cells in the Global Energy System. *Energy and Environmental Science*. 2019, pp 463–491. https://doi.org/10.1039/c8ee01157e.

(6) Glenk, G.; Reichelstein, S. Economics of Converting Renewable Power to Hydrogen. *Nat Energy* **2019**, *4* (3), 216–222.

(7) Kim, J. S.; Kim, B.; Kim, H.; Kang, K. Recent Progress on Multimetal Oxide Catalysts for the Oxygen Evolution Reaction. *Advanced Energy Materials*. **2018**, *8*, 1702774. https://doi.org/10.1002/aenm.201702774.

(8) Nørskov, J. K.; Bligaard, T.; Logadottir, A.; Kitchin, J. R.; Chen, J. G.; Pandelov, S.; Stimming, U. Trends in the Exchange Current for Hydrogen Evolution. *J Electrochem Soc* **2005**, *152* (3), J23. https://doi.org/10.1149/1.1856988.

(9) McCrory, C. C. L.; Jung, S.; Peters, J. C.; Jaramillo, T. F. Benchmarking Heterogeneous Electrocatalysts for the Oxygen Evolution Reaction. *J Am Chem Soc* **2013**, *135* (45), 16977–16987. https://doi.org/10.1021/ja407115p.

(10) Xu, D.; Stevens, M. B.; Rui, Y.; DeLuca, G.; Boettcher, S. W.; Reichmanis, E.; Li, Y.; Zhang, Q.; Wang, H. The Role of Cr Doping in Ni–Fe Oxide/(Oxy)Hydroxide Electrocatalysts for Oxygen Evolution. *Electrochim Acta* **2018**, *265*, 10–18. https://doi.org/10.1016/j.electacta.2018.01.143.

(11) McCrory, C. C. L.; Jung, S.; Ferrer, I. M.; Chatman, S. M.; Peters, J. C.; Jaramillo, T. F. Benchmarking Hydrogen Evolving Reaction and Oxygen Evolving Reaction Electrocatalysts for Solar Water Splitting Devices. *J Am Chem Soc* **2015**, *137* (13), 4347–4357. https://doi.org/10.1021/ja510442p.

(12) Jerkiewicz, G. Standard and Reversible Hydrogen Electrodes: Theory, Design, Operation, and Applications. *ACS Catal* **2020**, *10* (15), 8409–8417. https://doi.org/10.1021/acscatal.0c02046.

(13) Plevová, M.; Hnát, J.; Bouzek, K. Electrocatalysts for the Oxygen Evolution Reaction in Alkaline and Neutral Media. A Comparative Review. *J Power Sources* **2021**, *507* (March). https://doi.org/10.1016/j.jpowsour.2021.230072.

(14) Pan, L.; Wang, Q.; Li, Y.; Zhang, C. Amorphous Cobalt-Cerium Binary Metal Oxides as High Performance Electrocatalyst for Oxygen Evolution Reaction. *J Catal* **2020**, *384*, 14–21. https://doi.org/10.1016/j.jcat.2020.02.005.

(15) Wang, J.; Cui, W.; Liu, Q.; Xing, Z.; Asiri, A. M.; Sun, X. Recent Progress in Cobalt-Based Heterogeneous Catalysts for Electrochemical Water Splitting. *Advanced Materials* **2016**, *28* (2), 215–230. https://doi.org/10.1002/adma.201502696.

(16) Thekkoot, S.; Islam, R.; Gray, O.; Morin, S. Efficiency of Nanostructured CuxCo3-XO4 and NixCu1 – XCo2O4 Electrodes as Electrocatalysts for the Oxygen Evolution Reaction-Revisited. *Electrochim Acta* **2023**, *471*, 143339. https://doi.org/10.7868/s0002337x15010042.

(17) Thekkoot, S.; Islam, R.; Morin, S. Improved Oxygen Evolution Reaction Performance with Addition of Fe to Form FeyCux-YCo3-XO4 and FeyNix-YCo3-XO4 (x = 0.5, 1 and y = 0.1, 0.15) Spinel Oxides. *Electrochim Acta* **2021**, *378*, 14–16. https://doi.org/10.1016/j.electacta.2021.138116.

(18) Thekkoot, S. R. Nanostructured Mixed Transition Metal Spinel Oxide as Efficient Electrocatalysts, Master's Thesis, York University, Toronto, Canada, 2015.

Chapter 2: Background context and theoretical framework

2.1 Overview of literature on amorphous oxides

Amorphous compounds are defined as solids with no crystalline properties and no long-range order[1]. These compounds have been widely prepared using different synthesis methods such as thermal decomposition, photochemical organic metal decomposition (PMOD), and electrodeposition[2]. The main techniques used for the characterization of amorphous compounds is XRD in which an amorphous compound is identified by weak and broad XRD patterns or the absence of a pattern. However other techniques, such as XPS and SEM, can provide a better understanding of the surface chemistry and morphology, respectively.

According to Fagan et al[3] amorphous FeCoNi oxides films have high OER activity. Driess et al[4] have also reported that amorphous CoFe oxides have better performances as OER catalyst than their crystalline forms. Fagan et al[3] report the preparation of twenty-one amorphous mixed metal oxides with the general formula $Fe_{100-y-z}Co_yNi_zO_x$ (y and z = 0, 20, 40, 60, 80,100) using the PMOD technique. The EDX and XPS data confirm the elemental compositions and homogeneity of these films. This paper also investigated the kinetic parameters of these amorphous binary and ternary metal oxides using data extracted from the Tafel slope for the OER. According to this data, the compositions with 20-40% iron concentration in binary and ternary films have the lowest OER onset potential. As the amount of iron increases, the onset of OER (in 0.1M KOH) also increases until a maximum is reached for $Fe_{100}O_x$. The Tafel slope contour plot also shows a sensitivity to the iron concentration in the ternary oxides. In the absence of iron, cobalt and nickel oxides display a high Tafel slope in the range of 70-80 mV/dec when the oxide is nickel rich and a lower Tafel slope in the range of 60 mV/dec when the oxide is cobalt rich. Increasing iron concentration decreases this high Tafel slope to around 30-40 mV/dec. It can be concluded that an iron amount of 40-60% gives an optimal Tafel slope. These authors have reported some trends in the overpotential required to reach a current of 0.5 mA/cm^2. The binary oxides lacking iron require higher potential to reach to 0.5 mA/cm^2 due to their higher Tafel slope. Overall, a concentration of 20-40 % iron in the binary and ternary metal oxides gives good combination of Tafel slope, onset potential, and potential required to reach a current density of 0.5 mA/cm^2.

The paper by Bai et al[5] confirms Fagan et al[3] reports as they have determined that OER activity of monometallic CoO_x and NiO_x can be improved by adding iron and form binary metal oxides. Moreover, the overpotential required to reach the current density of 10 mA/cm^2 is much greater (336mV) for $CoNiO_x$ than $FeCoO_x$ and $FeNiO_x$. This paper reports an overpotential of 240 mV for the ternary $FeCoNiO_x$ which is higher than the previously reports (see ref. 5). Measuring the faradaic efficiency of this ternary metal oxide led to 95% efficiency which was done by gas chromatography. This confirms that the anodic current is mainly from the generation of oxygen.

2.2 Overview of literature on spinel oxides and the role of iron

Spinel oxides are present in the form of AB_2O_4, in which A is a metal in the form of A^{2+} and fills one eighths of a tetrahedral site, while B is a metal in the form of B^{3+} and fills one half of an octahedral site in a unit cell[6]. Spinel structures have been widely studied and reported, while very few reports tried to map out a systematic relationship between the surface compositions of the ternary oxides to their catalytic activity[7].

Electrochemical studies using cyclic voltammetry (figure 2) in 1M KOH solution showed that spinel cobalt oxides containing iron have the most current produced and the lowest overpotential for OER[8]. A similar trend was reported by Corrigan in which adding small amounts of iron to nickel oxides increased the catalytic activity and decreased the overpotential of OER in 5.5M KOH[9]. In Fe-Co systems, the interaction between iron and cobalt leads to a synergistic effect This interaction improves the conductivity of the catalyst and provides more active sites for OER. One reason for this promoted catalytic activity, could be that iron prefers to occupy an octahedral site in the spinel structure therefore limiting the Co to the tetrahedral site. According to Hung et. al. there is a strong relationship between the catalytic activity of the electrode towards OER and the number of Co^{2+} in tetrahedral site of the spinel[10]. This idea was also suggested by Lu et al as he attributed the high catalytic activity of $Fe_{0.1}Ni_{0.9}Co_2O_4$ to the highest Co^{2+}/Co^{3+} ratio[11]. Therefore, chemical composition plays an important role in the catalytic activity towards OER and designing a suitable combination of metal cations in spinel structure could lead to a significant increase in current density.

More recently, there are reports containing operando X-ray absorption spectroscopy (XAS) and X-ray diffraction results which provide insight into the catalytically active state of crystalline Co_3O_4. For instance, this paper by Bergmann *et al*[12] reports that during OER, a thin amorphous layer forms on the surface of the crystalline Co_3O_4. This transformation is reversible; the amorphous state turns back into its original crystalline form when the reaction stops. The amorphous $CoO_x(OH)_y$ layer, which is less than a nanometer thick, is catalytically active. It contains cobalt ions in different oxidation states (Co^{3+}/Co^{4+}) linked by di-μ-oxo bridges, enhancing the oxygen evolution process. This reversibility offers a combination of high catalytic activity (due to the amorphous state) and stability (from the crystalline form), providing an advantage over materials that degrade permanently during such reactions.

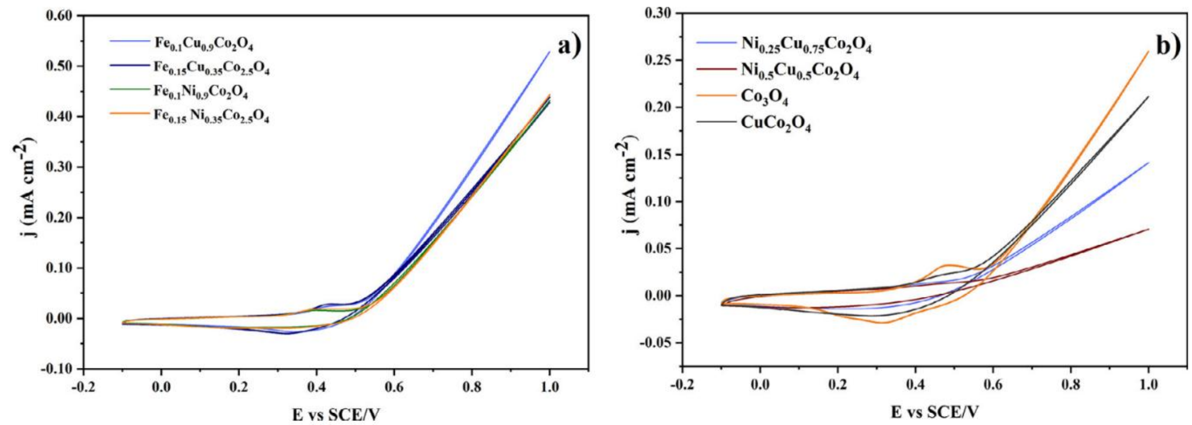

Figure 2. CVs of a) iron incorporated nickel and copper cobalt oxides and b) metal oxides without iron. The current density is corrected for their real surface area using the roughness factor (adapted from ref. 5)

2.3 Interfacial properties, electrode capacitance and their meaning in electrochemistry

Interfacial properties and electrode capacitance are important factors in electrochemical processes and have a significant influence on the performance and efficiency of electrochemical cells. Understanding these properties is essential for optimizing electrode materials and improving the functionality of electrocatalysts. Particularly, electrode capacitance is a key parameter that shows the surface area and electrochemical activity of an electrode, providing insights into its efficiency and behavior in various electrochemical reactions.

The capacitance of the electrode is often linked with the double-layer capacitance, which results from the separation of charge at the electrode-electrolyte interface. This capacitance is directly related to the surface area of the electrode. Larger surface areas typically lead to higher capacitance values. Therefore, accurate capacitance measurement is important for determining the performance of electrodes in applications such as supercapacitors, batteries, and sensors[13].

Various methods have been developed to measure and analyze the surface area and capacitance of electrodes with each of them offering their specific advantages and insights. One common technique is EIS, which provides detailed information about the impedance of an electrode over a range of frequencies. EIS can be used to extract the double-layer capacitance and determine the surface properties of the electrode by analyzing the impedance spectra [14].

Another widely used technique is CV, which measures the current response of an electrode to a linearly swept potential. By analyzing the voltammogram, the capacitance of the electrode and its electrochemical properties can be determined. The capacitance values obtained from CV are often used to evaluate the performance of electrodes in energy storage applications [15].

Surface area measurements can also be obtained from physical methods such as Brunauer-Emmett-Teller (BET) analysis, which determines the specific surface area of materials by nitrogen adsorption. This method is particularly useful for characterizing porous materials and understanding their effect on electrochemical performance[16]. Additionally, methods such as Scanning Probe Microscopy (SPM) and Atomic Force Microscopy (AFM) provide high-resolution images of electrode surfaces, giving valuable information on surface morphology and roughness[17]. However, these methods have not been employed in this work as they were not readily available. In addition, BET requires a large amount of material in a powder form. Thin films, such as ours, consisting of about 5 mg of materials cannot be characterize by BET.

Understanding interfacial properties and electrode capacitance is fundamental to the field of electrochemistry. The various methods available for measuring these properties provide a comprehensive view of electrode performance and are crucial for the development and optimization of electrochemical technologies.

2.4 Cyclic Voltammetry

Cyclic voltammetry is a technique that measures the current versus the potential difference between the reference electrode (SCE) and the working electrode (thin film) and the graphical representation of this is called cyclic voltammogram or CV. Cyclic voltammetry as the name implies, measures the current of a redox active analyte as a function of a potential sweep which cycles between two or more prespecified values. Consider a general reaction:

$$\text{Oxidant} + ne^- \rightarrow \text{Reductant} \qquad (2.1)$$

The Nernst equation for this reaction is:

$$E = E° - \frac{RT}{nF} ln \frac{[Red]}{[Ox]} \qquad (2.2)$$

where E stands for the cell potential, E° for the standard potential, R for the gas constant, T for the temperature, n for the number of electrons, and F for Faraday's constant. According to this reaction, the cell potential is related to the standard potential and the relative concentration of the oxidized and reduced analyte at equilibrium[15].

As the potential sweeps linearly between the set values, a cycle is being generated which corresponds to anodic sweep (positive currents) and cathodic sweep (negative currents). This cycle is repeated at different scan rates and the anodic or cathodic current is plotted as a function of scan rate By taking an average of the analyzed slopes of these plots, the double-layer capacitance (C_{dl}) can be determined which will then help to obtain the roughness factor (R_f). The roughness factor can be described as the real surface area divided by the geometric area[6]. Determining the roughness factor allows to compare CV's of materials with different compositions and different structures (amorphous and spinel).

The main components of a cyclic voltammogram include an electrochemical cell, a potentiostat, a converter (current to voltage), and a display device. The cell consists of the electrolyte solution and three electrodes: working (thin film of sample), reference (SCE), and counter (platinum mesh) electrodes. The electrolyte solution serves the purpose of providing ions during the process and the role of potentiostat is to measure the potential difference between the reference and the working electrode.

2.5 Overview of literature on Linear Sweep Voltammetry (LSV)

Linear Sweep Voltammetry (LSV) is a basic electrochemical technique that provides detailed information on the redox behavior of the materials. During LSV, the electrode potential is varied linearly with time, and the resulting current is recorded to produce a voltammogram. This technique is important to study reaction kinetics, to identify electroactive species, and to characterize the mechanism of the electrochemical processes[18]. LSV's adoptability results in using it in a variety of applications such as the evaluation of corrosion behavior, catalyst performance, and sensor design.

The Tafel slope, derived from Tafel plots, is an important parameter often analyzed with LSV data. It provides insights into the reaction kinetics and mechanisms by showing the relationship between the overpotential and the logarithm of the current density. The Tafel slope is especially valuable to understand the rate-determining steps in the reactions and to determine the catalytic efficiency of electrodes[19]. Analysis of the Tafel slope can lead to a deeper understanding of the factors influencing reaction rates, such as activation energy and reaction intermediates.

Recent literature reports the advantages in using the LSV and Tafel slope together. These studies have focused on optimizing the experimental conditions to improve the accuracy and reliability of Tafel slope measurements. For instance, improving the electrode materials and making modifications in the setups have led to more precise determination of kinetic parameters and a better understanding of catalytic processes[20].

There are recent reports of the exploration of novel materials and configurations that affect the Tafel slope. For instance, nanostructured and modified electrodes have shown significant improvements in catalytic activity which was obtained by the changes in the Tafel slope. This reflects an improved reaction kinetics and lower overpotentials[21].

2.6 Electrochemical impedance spectroscopy

Electrochemical impedance spectroscopy is a widely used technique to study kinetic and reaction mechanism in energy conversion and storage science. EIS basically involves the disruption of an electrochemical system that is at steady state by applying a sinusoidal signal (alternating voltage or current) over a broad range of frequencies (typically from kHz to mHz). This disruption is monitored by observing the system's sinusoidal response (either current or voltage) to the applied signal. The significance of this technique over alternative electrochemical techniques is that EIS is able to differentiate and supply extensive information regarding a variety of electrical, electrochemical, and physical processes that occur in a real system. This capability presents a significant challenge, given that these different processes may occur over very different time scales [22]. The solution resistance of the electrolyte, the charging and discharging procedures of the double layer capacitance, the relationship between the double layer capacitance, charge transfer rates and the morphology of the electrode surface, etc., all exhibit distinct time constants which is measured as $\tau = RC$

where R represents the resistance (Ohm) and C, capacitance (Farad)[23]. The EIS data conducted for an electrochemical system is often replicated through an equivalent circuit. This system is composed of typical passive components like resistances, capacitors, and inductors, alongside more intricate elements. These components are interconnected in various configurations. Essentially, each process can be linked to an equivalent electrical circuit, exhibiting a unique time constant. In order to do this circuit modeling of the electrochemical system, special software will be employed. The software used in this research is EC-Lab V11.41 (demonstration version). One of the most important things to consider when modeling the system into a circuit is to match up the components of the circuit to the individual processes using electrochemical knowledge and scientific logic. Some of these processes are hard to analyze and possess certain challenges when operating in the time-domain (cyclic voltammetry for instance). However, when operating in frequency domain across a broad spectrum of frequencies, for instance EIS has the capability to disentangle the complexity of the system by breaking it down into individual processes with distinct time constants[22]. Slower processes can be examined at lower frequencies, while faster processes can be investigated at higher frequencies. The frequency range for a particular experiment is limited by the electrochemical cell and instrumentation employed. Usually an EIS spectrum covers frequencies that range from 100 kHz to 0.1 Hz with 60 frequencies (10 per decade) and requires approximately 2 to 3 minutes to complete.

2.6.1 Deriving the RC circuit

Following the treatment of Bredar *et al* [24], a series RC circuit consists of a resistor and a capacitor connected in series. Applying an alternating current to this circuit will result in Ohm's law:

$$I = \frac{V}{Z} \qquad (2.3)$$

where I, V, and Z are the current, voltage and impedance, respectively. According to the law of charge conservation, the current stays the same passing through each component of this circuit over time. Therefore, the resistor and the capacitor have an equal current in phase and magnitude. For the voltage however, the sum of the voltages across both components are considered:

$$V(t) = VR(t) + VC(t) \qquad (2.4)$$

Considering the instantaneous current as i(t), then,

$$V(t) = i(t)R + i(t)\frac{1}{j\omega C} \qquad (2.5)$$

$$V(t) = i(t)\left(R + \frac{1}{j\omega C}\right) \qquad (2.6)$$

in which ω is called the angular frequency (radian/second) of the AC circuit and has a relationship with the frequency (Hertz):

$$\omega = 2\pi f \qquad (2.7)$$

and j is the imaginary number described as $j^2 = -1$. Therefore, we will have,

$$Z = R + \frac{1}{j\omega C} = \sqrt{R^2 + \left(\frac{1}{\omega C}\right)^2}\, e^{j\phi} \qquad (2.8)$$

in which ϕ represents phase angle and has a relationship with resistor and capacitor as[24]

$$\cos\phi = \frac{R}{\sqrt{R^2+\left(\frac{1}{\omega C}\right)^2}} \qquad (2.8)$$

To summarize, this chapter included a literature review and background context on amorphous and spinel oxides (i.e. two different morphologies). Moreover, it contains a brief review on the ways to measure the surface of the electrode including CV, EIS and LSV. These electrochemical characterization techniques as well as structural and chemical techniques will be explored and discussed in detail in the next chapter.

2.7 References

(1) Lan, S.; Zhu, L.; Wu, Z.; Gu, L.; Zhang, Q.; Kong, H.; Liu, J.; Song, R.; Liu, S.; Sha, G.; Wang, Y.; Liu, Q.; Liu, W.; Wang, P.; Liu, C. T.; Ren, Y.; Wang, X. L. A Medium-Range Structure Motif Linking Amorphous and Crystalline States. *Nat Mater* **2021**, *20* (10), 1347–1352. https://doi.org/10.1038/s41563-021-01011-5.

(2) Yan, S.; Abhilash, K. P.; Tang, L.; Yang, M.; Ma, Y.; Xia, Q.; Guo, Q.; Xia, H. Research Advances of Amorphous Metal Oxides in Electrochemical Energy Storage and Conversion. *Small* **2019**, *15* (4), 1–30. https://doi.org/10.1002/smll.201804371.

(3) Smith, R. D. L.; Prévot, M. S.; Fagan, R. D.; Trudel, S.; Berlinguette, C. P. Water Oxidation Catalysis: Electrocatalytic Response to Metal Stoichiometry in Amorphous Metal Oxide Films Containing Iron, Cobalt, and Nickel. *J Am Chem Soc* **2013**, *135* (31), 11580–11586. https://doi.org/10.1021/ja403102j.

(4) Indra, A.; Menezes, P. W.; Sahraie, N. R.; Bergmann, A.; Das, C.; Tallarida, M.; Schmeißer, D.; Strasser, P.; Driess, M. Unification of Catalytic Water Oxidation and Oxygen Reduction Reactions: Amorphous Beat Crystalline Cobalt Iron Oxides. *J Am Chem Soc* **2014**, *136* (50), 17530–17536. https://doi.org/10.1021/ja509348t.

(5) Bai, L.; Wen, X.; Guan, J. Amorphous Fe[Sbnd]Co[Sbnd]Ni Oxide for Oxygen Evolution Reaction. *Mater Today Energy* **2019**, *12*, 311–317. https://doi.org/10.1016/j.mtener.2019.02.004.

(6) Thekkoot, S.; Islam, R.; Gray, O.; Morin, S. Efficiency of Nanostructured CuxCo3-XO4 and NixCu1 – XCo2O4 Electrodes as Electrocatalysts for the Oxygen Evolution Reaction-Revisited. *Electrochim Acta* **2023**, *471*, 143339. https://doi.org/10.7868/s0002337x15010042.

(7) Zhao, Q.; Yan, Z.; Chen, C.; Chen, J. Spinels : Controlled Preparation , Oxygen Reduction / Evolution Reaction Application, and Beyond. *Chem Rev* **2017**, *117* (15), 10121–10211. https://doi.org/10.1021/acs.chemrev.7b00051.

(8) Thekkoot, S.; Islam, R.; Morin, S. Improved Oxygen Evolution Reaction Performance with Addition of Fe to Form FeyCux-YCo3-XO4 and FeyNix-YCo3-XO4 (x = 0.5, 1 and y = 0.1, 0.15) Spinel Oxides. *Electrochim Acta* **2021**, *378*, 14–16. https://doi.org/10.1016/j.electacta.2021.138116.

(9) Corrigan, D. A. Catalysis of the Oxygen Evolution Reaction by Trace Iron Impurities in Thin Film Nickel Oxide Electrodes. *J Electrochem Soc* **1987**, *134*, 377.

(10) Hung, S. F.; Hsu, Y. Y.; Chang, C. J.; Hsu, C. S.; Suen, N. T.; Chan, T. S.; Chen, H. M. Unraveling Geometrical Site Confinement in Highly Efficient Iron-Doped Electrocatalysts toward Oxygen Evolution Reaction. *Adv Energy Mater* **2018**, *8* (7), 1701686. https://doi.org/10.1002/aenm.201701686.

(11) Lu, Y. T.; Chien, Y. J.; Liu, C. F.; You, T. H.; Hu, C. C. Active Site-Engineered Bifunctional Electrocatalysts of Ternary Spinel Oxides, M0.1Ni0.9Co2O4 (M: Mn, Fe, Cu, Zn) for the Air Electrode of Rechargeable Zinc–Air Batteries. *J Mater Chem A Mater* **2017**, *5* (39), 21016–21026. https://doi.org/10.1039/C7TA06302D.

(12) Bergmann, A.; Martinez-Moreno, E.; Teschner, D.; Chernev, P.; Gliech, M.; De Araújo, J. F.; Reier, T.; Dau, H.; Strasser, P. Reversible Amorphization and the Catalytically Active State of Crystalline Co3O4 during Oxygen Evolution. *Nat Commun* **2015**, *6*, 8625. https://doi.org/10.1038/ncomms9625.

(13) Bard, A. J.; Faulkner, L. R. *Electrochemical Methods: Fundamentals and Applications*, 2nd ed.; Wiley: New York, 2001.

(14) Orazem, M.E.; Tribollet, B. *Electrochemical Impedance Spectroscopy*.; John Wiley and Sons: 2008.

(15) Elgrishi, N. N.; Rountree, K. J.; Mccarthy, B. D.; Rountree, E. S.; Eisenhart, T. T.; Dempsey, J. L. A Practical Beginner's Guide to Cyclic Voltammetry. **2017**. https://doi.org/10.1021/acs.jchemed.7b00361.

(16) Brunauer, S.; Emmett, P. H.; Teller, E. Adsorption of Gases in Multimolecular Layers. *J Am Chem Soc* **1938**, *60* (2), 309–319. https://doi.org/10.1021/JA01269A023.

(17) Binnig, G.; Quate' ', C. F.; Gi, E. L.; Gerber, C. Atomic Force Microscope. *Phys Rev Lett* **1986**, *56* (9), 930–933.

(18) aoki, K.; Tokuda, K.; Matsuda, H. Linear Sweep and Cyclic Voltammetry for Electrocatalysis at Modified Electrodes with Very Thin Films. *J Electroanal Chem Interfacial Electrochem* **1986**, *199* (1), 69–79. https://doi.org/10.1016/0022-0728(86)87042-5.

(19) Kapałka, A.; Fóti, G.; Comninellis, C. Determination of the Tafel Slope for Oxygen Evolution on Boron-Doped Diamond Electrodes. *Electrochem commun* **2008**, *10* (4), 607–610. https://doi.org/10.1016/j.elecom.2008.02.003.

(20) van der Heijden, O.; Park, S.; Vos, R. E.; Eggebeen, J. J. J.; Koper, M. T. M. Tafel Slope Plot as a Tool to Analyze Electrocatalytic Reactions. *ACS Energy Lett* **2024**, *9* (4), 1871–1879. https://doi.org/10.1021/acsenergylett.4c00266.

(21) Anantharaj, S.; Noda, S. How Properly Are We Interpreting the Tafel Lines in Energy Conversion Electrocatalysis? *Mater Today Energy* **2022**, *29*, 101123. https://doi.org/10.1016/j.mtener.2022.101123.

(22) Lazanas, A. C.; Prodromidis, M. I. Electrochemical Impedance Spectroscopy - A Tutorial. *ACS Measurement Science Au* **2023**, *3*, 162–193. https://doi.org/10.1021/acsmeasuresciau.2c00070.

(23) Palmas, S.; Ferrara, F.; Vacca, A.; Mascia, M.; Polcaro, A. M. Behavior of Cobalt Oxide Electrodes during Oxidative Processes in Alkaline Medium. *Electrochim Acta* **2007**, *53*, 400–406. https://doi.org/10.1016/j.electacta.2007.01.085.

(24) Bredar, A. R. C.; Chown, A. L.; Burton, A. R.; Farnum, B. H. Electrochemical Impedance Spectroscopy of Metal Oxide Electrodes for Energy Applications. *ACS Appl Energy Mater* **2020**, *3*, 66–98. https://doi.org/10.1021/acsaem.9b01965.

Chapter 3: Experimental techniques and instrumentation

3.1 Experimental

3.1.1 Reagents and materials

The spinel oxides were prepared via thermal decomposition using a furnace for heating. The inorganic precursors comprised iron (III) nitrate nonahydrate, cobalt (II) nitrate hexahydrate, nickel (II) nitrate hexahydrate, and copper (II) nitrate trihydrate. All the purchased chemicals were utilized without further purification.

The amorphous oxides were prepared via thermal decomposition under a near-infrared (NIR) lamp (150W). Thin films were positioned at a distance of 2cm under the lamp. The organic precursors comprised iron (III) 2-ethylhexanoate, copper (II) 2-ethylhexanoate, cobalt (II) 2-ethylhexanoate, and nickel (II) 2-ethylhexanoate. All the purchased chemicals were utilized without further purification.

3.1.2 Preparation of spinel oxide thin film

The appropriate quantities of each metal precursor were prepared by dissolving the required amounts of $Co(NO_3)_2{\cdot}6H_2O$ (A.C.S Sigma Aldrich, ≥ 98 %), $Cu(NO_3)_2$. $3H_2O$ (Sigma Aldrich, 99.0 % - 100.5 %), $Ni(NO_3)_2{\cdot}6H_2O$ (A.C.S Sigma Aldrich, ≥ 98.5 %), and $Fe(NO_3)_3{\cdot}9H_2O$ (Sigma Aldrich, ≥ 98%) in a mixture of 3:1 isopropanol to water (Millipore, Milli-Q Synthesis A10). The solutions were stirred with 10 µL of Triton X-100 for 24 hours to form the final solution of each composition (concentration of 0.3 M). The layers (each layer containing 15 µL of the salt solution) were then dropwise deposited on a piece of conductive glass (ca. 1.5 cm x 1.5 cm) coated by fluorine-doped tin oxide (FTO). The solvent was evaporated after each layer deposition by heating at 400 °C for ten minutes (Lindberg BF51732BC). The described procedure was followed five times. Finally, the samples were annealed for 2 hours at the same temperature[1,2].

3.1.3 Preparation of amorphous oxide thin film

Similar to the spinel oxides, stock solutions of 0.5 M were prepared by dissolving the required amounts of iron (III) 2-ethylhexanoate diisopropoxide (10% w/v in isopropanol, Thermo Scientific), cobalt (II) 2-ethylhexanoate (65% w/w in mineral spirits, Sigma Aldrich), nickel (II) 2-octanoate (8% Ni in in mineral spirit, Thermo Scientific), and copper (II) 2-ethylhexanoate (Sigma Aldrich) in hexane. The solutions were stirred for 2 hr to form the final solution (0.5 M) of each composition. The layers were deposited dropwise on a piece of FTO glass. The solvent was evaporated between each layer by heating under the infrared lamp for 30 minutes[3,4]. A total of three layers were deposited on each glass.

3.1.4 Sample preparation for LSV and Tafel measurements

Sample preparation involved preparing nitrate salt solutions following the procedure described in section 3.1.2 to achieve the desired final composition. These solutions were placed in crucibles, and the solvent was evaporated by heating in a furnace at 400ºC for two hours. The resulting powders were grinded with a mortar and pestle, and about 10 mg of the sample was combined with Vulcan XC-72R (Cabot), a conductive carbon powder that enhances surface area. To this mixture, 300 µl each of isopropanol and water, along with 80 µl of Nafion (as a binder), were added. The solution was thoroughly mixed and applied to the glassy carbon disk (0.196 cm^2), then allowed to dry[5].

3.2 Scanning electron microscopy

Scanning electron microscopy is a technique that uses a focused beam of electrons to produce signals as it interacts with the surface of a sample. These signals, emitted from the surface, are collected and analyzed to provide detailed information about the sample's structure, texture, chemical composition, and material orientation.

3.2.1 Fundamentals

When a high-energy electron beam strikes the surface of a sample, its energy is dissipated through various signals originating not only from the surface but also from different depths within the sample. Depending on the type of information needed, signal collection can be adjusted accordingly. One key signal is from backscattered electrons (BSE), which result from electrons being elastically scattered by atomic nuclei. These signals are valuable for creating 2D images and obtaining compositional information about the sample. Secondary electrons, produced by inelastic scattering with sample atoms, also contribute to 2D imaging by providing insights into surface topography. Additionally, characteristic X-rays and Bremsstrahlung are generated from deeper within the sample and are utilized for chemical analysis of the bulk material[6].

3.2.2 Instrumentation

The primary components of a scanning electron microscope include the electron gun, electron lenses, sample holder, detectors, and display. The electron gun serves as the source, emitting electrons that are directed towards the sample. These electrons then pass through condenser lenses, which are magnetic lenses composed of wire coils designed to focus the electron beam by compressing it. The scanning generator repeatedly deflects the electron beam, allowing it to scan across the sample's surface in a predefined pattern. The collector detects secondary electrons and can be adjusted to capture additional signals[7]. The SEM images for this study were acquired using a SEM-FEI QUANTA 3D electron microscope. For the SEM analysis, the Everhart-Thornley Detector was used to capture secondary electrons deflected from the sample. A high energy of 20 kV was applied during the analysis to ensure accurate results. These analyses were carried out at the Imaging Facility located at York University.

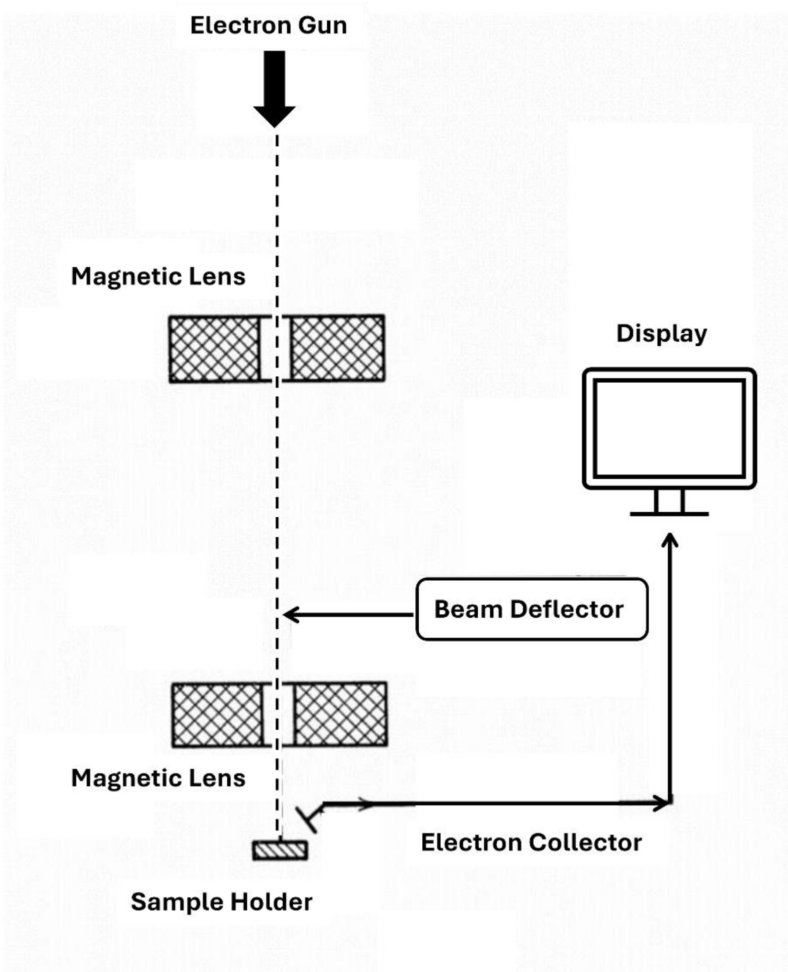

Figure 3. Schematic drawing of the scanning electron microscope

3.3 Energy dispersive X-ray

Energy dispersive X-ray spectroscopy (EDX) is an analytical technique used to determine the elemental composition of materials. Like scanning electron microscopy, this method utilizes an electron beam to excite inner shell electrons, creating vacancies. When electrons from outer shells fill these vacancies, each element emits a unique set of X-rays. These X-rays can be measured to obtain both quantitative and qualitative data on the surface composition of the sample[8].

3.3.1 Fundamentals

In quantum mechanics, the energy states of electrons around the nucleus are described by quantum numbers such as n=1, 2, 3, corresponding to the K, L, and M shells in spectroscopy. For X-ray emission to occur, electrons from the core shell (K) must be excited to higher energy levels, creating a vacancy in the lower energy shells. This vacancy is then filled by electrons transitioning from higher shells, emitting X-rays in the process. The energy and distance of these shells vary for each element due to differences in their electronic configurations[9].

3.3.2 Instrumentation

As previously mentioned, an energy dispersive spectrometer employs an electron gun to accelerate electrons towards the sample, with the electron beam being focused by electron lenses. The X-rays emitted from the specimen strike the junction plate, causing the plate's electrons to move into the conduction band. This movement generates a voltage corresponding to the incident X-rays, which is then detected[10]. The energy dispersive X-ray spectroscopy (EDX) analysis was performed using the EDAX GENESIS which includes Octane Elect Plus Detector to detect backscattered electrons. These analyses were carried out at the Imaging Facility located at York University.

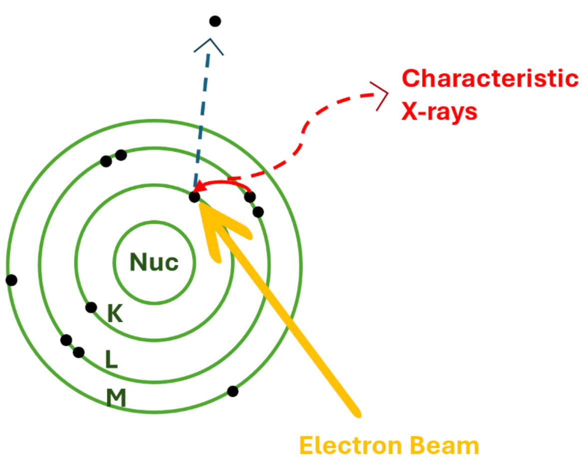

Figure 4. Schematic representation of energy dispersive x-ray principle

3.4 X-ray diffraction

X-ray diffraction is a commonly employed technique for characterizing and identifying the bulk composition of crystalline materials. Its popularity stems from its capability to measure the size, shape, and spacing between internal crystalline regions.

3.4.1 Fundamentals

A cathode ray tube generates monochromatic X-rays, which are directed towards the sample. When these X-rays interact with the crystalline structure of the sample, diffraction occurs. This diffraction is considered constructive interference when the conditions of Bragg's law are met:

$$n\lambda = 2d\sin\theta \qquad (3.1)$$

According to Bragg's law, there is a relationship between the incident wavelength (λ), the diffraction angle (θ), and the distance between layers in a crystal (d). To capture all diffraction directions, the sample is scanned over a range of 2θ, and the resulting X-rays are collected and analyzed. The distance between atomic layers in a crystal can be determined by comparing the resulting diffraction peaks with standard reference patterns, as these spacings are unique to each element[11].

3.4.2 Instrumentation

The main components of an X-ray diffractometer include the X-ray tube, sample holder, and X-ray detector. Electrons produced by a cathode ray tube are directed at the sample, and characteristic X-ray spectra are generated when the incident electrons have sufficient energy to displace inner shell electrons in the sample. In an XRD pattern, the intensity of the X-ray beam is plotted against the diffraction angle (2θ), with peaks occurring when the incident X-rays meet Bragg's conditions. These X-rays are then detected, converted, and displayed as a pattern on the monitor[12]. The X-ray diffraction patterns of the electrodes in this work were obtained at the XRD facility located at the McMaster University. These patterns were recorded using the Bruker D8 DISCOVER DAVINCI DESIGN diffractometer, utilizing Co Kα radiation with a wavelength of λ = 1.79026 Å. The high-resolution Vantec 500 (MikroGap™ technology) was utilized as a detector during this analysis. Data collection and unit cell refinements were carried out using the sophisticated DIFFRAC Measurement center version 3.0 software and Topas Version 4.0 software, respectively.

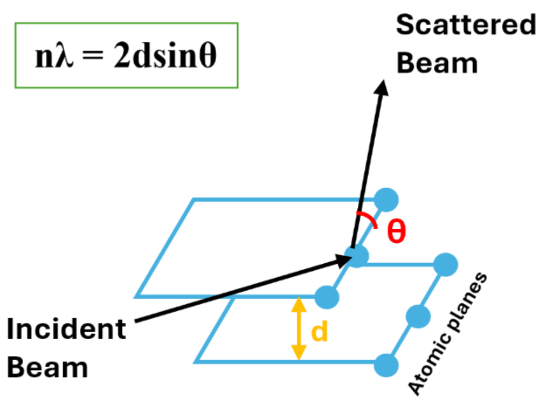

Figure 5. Schematic representation of the Bragg's law

3.5 X-ray photoelectron spectroscopy

To study surface chemistry and catalysis, a popular choice for material scientists and chemists is XPS. Since it has the ability to differentiate between different oxidation states of elements, it is considered as a powerful tool for analyzing oxides, catalysts, and metal compounds[13]. By combining elemental identification with chemical state analysis, XPS allows researchers to investigate complex surface phenomena at a molecular level.

3.5.1 Fundamentals

Fundamentals of XPS are based on the principle of the photoelectric effect, where incoming X-rays interact with atoms in a material, leading to the electrons being ejected from core-level. By measuring the kinetic energy of these ejected electrons, we can calculate their binding energy, which depends on the elements present in the sample and their chemical states[14].

The binding energy (E_B) can be calculated from the equation:

$$E_B = h\nu - E_K - \phi \qquad (3.2)$$

where $h\nu$ is the energy of the incoming X-ray, E_K is the kinetic energy of the ejected electron, and ϕ is the work function of the spectrometer. Since XPS only analyzes electrons from the outermost 1–10 nm of a sample, it provides information about the material's surface, making it ideal for surface studies such as oxidation, thin films, and catalysis[14].

3.5.2 Instrumentation

The main components of a typical XPS instrument consists of an X-ray source, an ultra-high vacuum (UHV) chamber, an electron energy analyzer, and a detector[15]. The X-ray source generates the incoming X-ray required for photoelectron emission. The UHV environment is important because it prevents inelastic scattering of ejected electrons by ambient gas molecules as well as surface contamination from species present in the atmosphere. Most importantly electrons emitted from the source have a short lifespan outside UHV, due to loosing energy quickly and being scattered off air molecules. Once the X-rays interact with the sample, electrons are ejected and directed into the electron energy analyzer (hemispherical analyzer) where they get sorted out by their kinetic energy. Thus, it allows the detector to measure their intensity as a function of energy. The XPS spectrum exhibits peaks that are correspond to the binding energies of ejected electrons from different atomic orbitals. Also, the peak areas are related to the concentration of each element[15].

X-ray photoelectron spectroscopy (XPS) was employed in this work to analyze spinel oxides. This analysis was performed using a Kratos Axis Supra Spectrometer located at Surface Science Western, London. This spectrometer is equipped with a monochromatic Ag Lα X-ray source (2984.2 eV). The calibration of the instrument's work function has led to a binding energy of 83.95 eV for the Au $4f_{7/2}$ peak. The base pressure during the analysis was maintained at 8×10^{-10} Torr. High-resolution spectra were acquired using the following parameters: measuring area approximately 300 × 700 µm, pass energy 20 eV, step size 0.1 eV, and sweep intervals 60 seconds. To correct for the charging, the C 1s peak from adventitious carbon at 284.8 eV was used. A Shirley background was subtracted from the 2p region, and the peaks were fitted using a Gaussian/Lorentzian ratio of 70:30. The accuracy of peak positions was ±0.2 eV, and peak areas were normalized using appropriate atomic sensitivity factors for quantitative analysis.

3.6 Transmission electron microscopy

Transmission electron microscopy (TEM) is a widely used technique to obtain information about the internal structure of the materials at high resolution. This technique is mainly popular in materials science and nanotechnology to study the morphology and crystallography of the sample[7].

3.6.1 Fundamentals

The fundamentals behind transmission electron microscopy are very similar to those for scanning electron microscopy and electron dispersive spectroscopy that have been described in sections 3.2 and 3.3 respectively. This technique also requires a high energy beam of electrons to hit the sample and scatter based on the atomic structure and composition of the sample. This creates an image which is magnified through special lenses. Moreover, many relaxation processes such as emitting characteristic X-rays, Auger electrons and light that are caused by inelastic scattering help in chemical analysis of the sample in TEM[16].

3.6.2 Instrumentation

The components of a TEM instrument include electron source, condenser and objective lenses, sample holder, projector lenses, detector and display. The electron source generates a high energy electron beam that is focused on the sample by condenser lens system. This system is comprised of few electromagnetic lenses that control the convergence and intensity of the beam which can be adjusted to facilitate different imaging techniques. The role of objective lenses is important in forming an initial image of the sample. The quality and alignment of these lenses can greatly impact the resolution power of the instrument. The projecting lenses magnify the image that was created by the objective lenses and project it on the detector. The final image can be viewed on the display system that could be captured using digital cameras. Modern TEM instruments usually are equipped with advanced detectors that make the system capable of performing other spectroscopy techniques such as EDX that can provide more information regarding the samples chemical and elemental composition as well as its structural image[17,18].

3.7 Cyclic voltammetry

3.7.1 Instrumentation

The key elements of a cyclic voltammogram setup include an electrochemical cell, a potentiostat, a current-to-voltage converter, and a display device. The electrochemical cell contains an electrolyte solution and three electrodes: a working electrode (with a thin film of the sample), a reference electrode (SCE), and a counter electrode (platinum mesh). The electrolyte solution provides ions during the experiment, while the potentiostat monitors the potential difference between the reference and working electrodes[19].

In this work cyclic voltammetry experiments were performed at room temperature using a 1 M KOH solution and VoltaLab 80 equipment, which included a PGZ402 potentiostat and Volta-master 4 software. A standard three-electrode setup was used, consisting of a working electrode (thin film), a reference electrode (saturated calomel electrode (SCE)), and a counter electrode (platinum wire). The sample was carefully placed at the bottom of the Teflon cell, with an opening size of 0.98 ± 0.01 cm², ensuring uniform surface exposure to the electrolyte. The electrochemical surface area of the electrodes was determined by analyzing double-layer charging curves via cyclic voltammetry in the 1 M KOH solution. The cyclic voltammograms were recorded in a limited potential window of –50 mV to 50 mV (vs. SCE) at scan rates ranging from 10 mV s^{-1} to 100 mV s^{-1}. Additionally, the redox behavior and electrocatalytic activity of the electrodes for the Oxygen Evolution Reaction (OER) were examined by recording CVs from -100 mV to 1000 mV at scan rate 50 mV s^{-1}.

3.8 LSV and Tafel measurements

3.8.1 Instrumentation

To measure LSV and Tafel slope analysis in this work, a Pine Research Wave Driver 200 potentiostat was used along with the MSRX speed control unit from Pine Instrument Company. Data analysis was performed using Aftermath software, version 1.6.1020. the three-electrode setup was employed including a glassy carbon electrode with the sample on it, a platinum mesh (counter electrode) and a SCE (reference electrode). The Tafel plot was recorded at 3000 rpm in 0.1M KOH, and argon gas was used to purge the electrolyte during the experiments.

3.9 Impedance measurements

3.9.1 Instrumentation

For this project the double-layer capacitance of the samples was assessed using Electrochemical Impedance Spectroscopy (EIS) with the Voltalab 80 system, which included a PGZ402 potentiostat and Voltamaster 4 software. These measurements were carried out at room temperature, maintaining a potential of 0 V vs. SCE in a 1 M KOH solution, using the previously described experimental setup. A frequency range from 0.1 Hz to 100 kHz was applied, with a potential perturbation of ±10 mV. The impedance data were then analyzed using EC-Lab V11.41 software for accurate interpretation. Additionally, differential capacitance measurements were performed on the samples over a potential range of -100 to 600mV, with a 50mV interval.

3.10 iR drop correction- theory and background

iR correction means compensating for the voltage drop caused by the electrolyte resistance (R) and other components between the working electrode and the reference electrode in an electrochemical system. When a current goes through the electrolyte solution, it causes an ohmic drop (iR) because of the solution's internal resistance. This drop can bias the measurements, especially for electrocatalysis which requires high current. Therefore, it is very important to correct for iR drop because neglecting this resistance can lead to inaccurate determination of overpotentials, Tafel slopes, and kinetic parameters, leading to a false interpretation of catalytic activity[20].

The theoretical background comes from Ohm's law, which states that the measured potential (V) is a contribution from both the electrochemical reaction and the resistance in the circuit. This causes some inaccuracies when the true potential of an electrode is being determined. Technically, iR correction compensates this voltage loss, usually using two methods: positive feedback (done during the experiment) and after the scan method (a manual data adjustment post-experiment) therefore ensuring accurate measurements of catalytic activity during studies like OER. However, it is crucial to avoid improper compensation which can lead to inaccurate data[21].

This drop can be compensated for usually through software tools like Electrochemical Impedance Spectroscopy (EIS) and the Current Interrupt (CI) technique. Using these tools, the resistance can be measured. EIS is especially effective since it determines the ohmic resistance by fitting the impedance data to an equivalent circuit model. The resistance obtained from this can then be used to correct the potential in experiments. Another technique is current interrupt which measures the instantaneous voltage drop when current is interrupted therefore provides a direct measurement of the iR drop[22].

3.11 Summary

To summarize, this chapter includes experimental and preparation techniques for both transition metal spinel and amorphous oxides. All of the reagents and materials used are mentioned. Moreover, a brief explanation of the fundamentals and instrumentation for each characterization technique is included. In addition, the specific experimental conditions and parameters of the instruments-that were used to characterize the samples are listed. Next chapter will include the results of these structural, chemical, and electrochemical characterizations and will be accompanied by a detailed result discussion and their correlations.

3.12 References

(1) Thekkoot, S.; Islam, R.; Morin, S. Improved Oxygen Evolution Reaction Performance with Addition of Fe to Form FeyCux-YCo3-XO4 and FeyNix-YCo3-XO4 (x = 0.5, 1 and y = 0.1, 0.15) Spinel Oxides. *Electrochim Acta* **2021**, *378*, 14–16. https://doi.org/10.1016/j.electacta.2021.138116.

(2) Marsan, B.; Fradette, N.; Beaudoin, G. Physicochemical and Electrochemical Properties of CuCo2 O 4 Electrodes Prepared by Thermal Decomposition for Oxygen Evolution. *J Electrochem Soc* **1992**, *139* (7), 1889–1896. https://doi.org/10.1149/1.2069516/XML.

(3) Salvatore, D. A.; Dettelbach, K. E.; Hudkins, J. R.; Berlinguette, C. P. Near-Infrared-Driven Decomposition of Metal Precursors Yields Amorphous Electrocatalytic Films. *Sci Adv* **2015**, *1* (2), 2–23. https://doi.org/10.1126/sciadv.1400215.

(4) Xu, D.; Stevens, M. B.; Rui, Y.; DeLuca, G.; Boettcher, S. W.; Reichmanis, E.; Li, Y.; Zhang, Q.; Wang, H. The Role of Cr Doping in Ni–Fe Oxide/(Oxy)Hydroxide Electrocatalysts for Oxygen Evolution. *Electrochim Acta* **2018**, *265*, 10–18. https://doi.org/10.1016/j.electacta.2018.01.143.

(5) Pauric, A. D.; Easton, E. B.; MacLean, B. J. Fe-N/C Oxygen Reduction Catalysts Prepared by Surface Functionalization of Carbon Black with 5,6-Diamino,1-10-Phenanthroline. *ECS Trans* **2010**, *28* (23), 55–62. https://doi.org/10.1149/1.3502337.

(6) A. Mohammed; A. Abdullah. Scanning Electron Microscopy (SEM): A Review. *Proceedings of 2018 International Conference on Hydraulics and Pneumatics - HERVEX* **2018**, 77–85.

(7) Nixon, W. C. The General Principles of Scanning Electron Microscopy. *Philosophical Transactions of the Royal Society of London. B, Biological Sciences* **1971**, *261* (837), 45–50. https://doi.org/10.1098/rstb.1971.0035.

(8) Prencipe, I.; Dellasega, D.; Zani, A.; Rizzo, D.; Passoni, M. Energy Dispersive X-Ray Spectroscopy for Nanostructured Thin Film Density Evaluation. *Sci Technol Adv Mater* **2015**, *16* (2), 25007. https://doi.org/10.1088/1468-6996/16/2/025007.

(9) Allen, L. J.; D'Alfonso, A. J.; Freitag, B.; Klenov, D. O. Chemical Mapping at Atomic Resolution Using Energy-Dispersive X-Ray Spectroscopy. *MRS Bull* **2012**, *37* (1), 47–52. https://doi.org/10.1557/mrs.2011.331.

(10) Hodoroaba, V. D.; Procop, M. A Method to Test the Performance of an Energy-Dispersive X-Ray Spectrometer (EDS). *Microscopy and Microanalysis* **2014**, *20* (5), 1556–1564. https://doi.org/10.1017/S1431927614001652.

(11) Nasir, S.; Hussein, M. Z.; Zainal, Z.; Yusof, N. A.; Mohd Zobir, S. A.; Alibe, I. M. Potential Valorization of By-Product Materials from Oil Palm: A Review of Alternative and Sustainable Carbon Sources for Carbon-Based Nanomaterials Synthesispotential Valorization of by-Product Materials from Oil Palm: A Review of Alternative and Sustaina. *Bioresources* **2019**, *14* (1), 2352–2388. https://doi.org/10.15376/biores.14.1.Nasir.

(12) Bunaciu, A. A.; Udriştioiu, E. gabriela; Aboul-Enein, H. Y. X-Ray Diffraction: Instrumentation and Applications. *Crit Rev Anal Chem* **2015**, *45* (4), 289–299. https://doi.org/10.1080/10408347.2014.949616.

(13) Siegbahn, K. Electron Spectroscopy for Atoms, Molecules and Condensed Matter - an Overview. *Rev Mod Phys* **1982**, *54* (3), 709–727. https://doi.org/10.1016/0368-2048(85)80013-X.

(14) Krishna, D. N. G.; Philip, J. Review on Surface-Characterization Applications of X-Ray Photoelectron Spectroscopy (XPS): Recent Developments and Challenges. *Applied Surface Science Advances* **2022**, *12* (November), 100332. https://doi.org/10.1016/j.apsadv.2022.100332.

(15) Cushman, C. V.; Chatterjee, S.; Major, G. H.; Smith, N. J.; Roberts, A.; Linford, M. R. Trends in Advanced XPS Instrumentation. I. Overview of the Technique, Automation, High Sensitivity, Imaging, Snapshot Spectroscopy, Gas Cluster Ion Beams, and Multiple Analytical Techniques on the Instrument. *Vacuum Technology & Coating* **2016**, No. 11, 2–9.

(16) Sigle, W. Analytical Transmission Electron Microscopy. *Annu Rev Mater Res* **2005**, *35*, 239–314. https://doi.org/10.1146/annurev.matsci.35.102303.091623.

(17) Miti, Ž.; Stoli, A.; Stojanovi, S.; Najman, S.; Ignjatovi, N.; Nikoli, G.; Trajanovi, M. Instrumental Methods and Techniques for Structural and Physicochemical Characterization of Biomaterials and Bone Tissue : A Review. *Materials Science and Engineering C* **2017**, *79*, 930–949. https://doi.org/10.1016/j.msec.2017.05.127.

(18) Yang, Q.; Li, X.; Zhao, L.; Wang, G.; Guo, Z.; Niu, K.; Jiang, S.; Hou, F.; Lin, J.; Yang, Q.; Li, X.; Zhao, L.; Wang, G.; Guo, Z.; Niu, K.; Jiang, S.; Hou, F.; Lin, J. Unified Transmission Electron Microscopy with the Glovebox Integrated System for Investigating Air-Sensitive Two-Dimensional Quantum Materials. *The Innovation* **2025**, *6* (1), 100751. https://doi.org/10.1016/j.xinn.2024.100751.

(19) Elgrishi, N. N.; Rountree, K. J.; Mccarthy, B. D.; Rountree, E. S.; Eisenhart, T. T.; Dempsey, J. L. A Practical Beginner's Guide to Cyclic Voltammetry. **2017**. https://doi.org/10.1021/acs.jchemed.7b00361.

(20) Anantharaj, S.; Noda, S. IR Drop Correction in Electrocatalysis: Everything One Needs to Know! *J Mater Chem A Mater* **2022**, *10* (17), 9348–9354. https://doi.org/10.1039/D2TA01393B.

(21) Zheng, W. IR Compensation for Electrocatalysis Studies: Considerations and Recommendations. *ACS Energy Lett* **2023**, *8*, 1952–1958. https://doi.org/10.1021/acsenergylett.3c00366.

(22) Son, Y. J.; Marquez, R. A.; Kawashima, K.; Smith, L. A.; Chukwuneke, C. E.; Babauta, J.; Mullins, C. B. Navigating IR Compensation: Practical Considerations for Accurate Study of Oxygen Evolution Catalytic Electrodes. *ACS Energy Lett* **2023**, *8* (10), 4323–4329. https://doi.org/10.1021/acsenergylett.3c01658.

Chapter 4: Results and discussion

4.1 Materials physical and chemical characterization

The synthesis and characterization of materials used as electrocatalysts for the OER are critical in understanding their efficiency and catalytic activity. In this study, materials prepared through thermal decomposition (described in section 3.1, chapter3) have been investigated. Thermal decomposition is a versatile technique that enables the formation of nanostructured materials with enhanced surface area, which is essential for electrocatalytic processes[1]. The prepared materials are subjected to a comprehensive set of physical, structural, and chemical characterizations, including but not limited to XRD for phase identification, SEM for morphological analysis, EDX for composition analysis, and XPS to study the oxidation states of active sites. These characterizations not only provide insights into the crystal structure and surface morphology but also reveal the chemical composition and active phases crucial for OER.

4.1.1 SEM results: film morphology

The surface texture of the amorphous and spinel oxides was analyzed by scanning electron microscopy. SEM images were obtained at three different positions on the surface of the thin film on FTO glass with various magnifications. As observed from SEM images (figure 6 and 7), the spinel oxides have a grainy and porous surface while their amorphous counterparts have a very smooth surface with the exception of large cracks that have formed in the film upon drying.

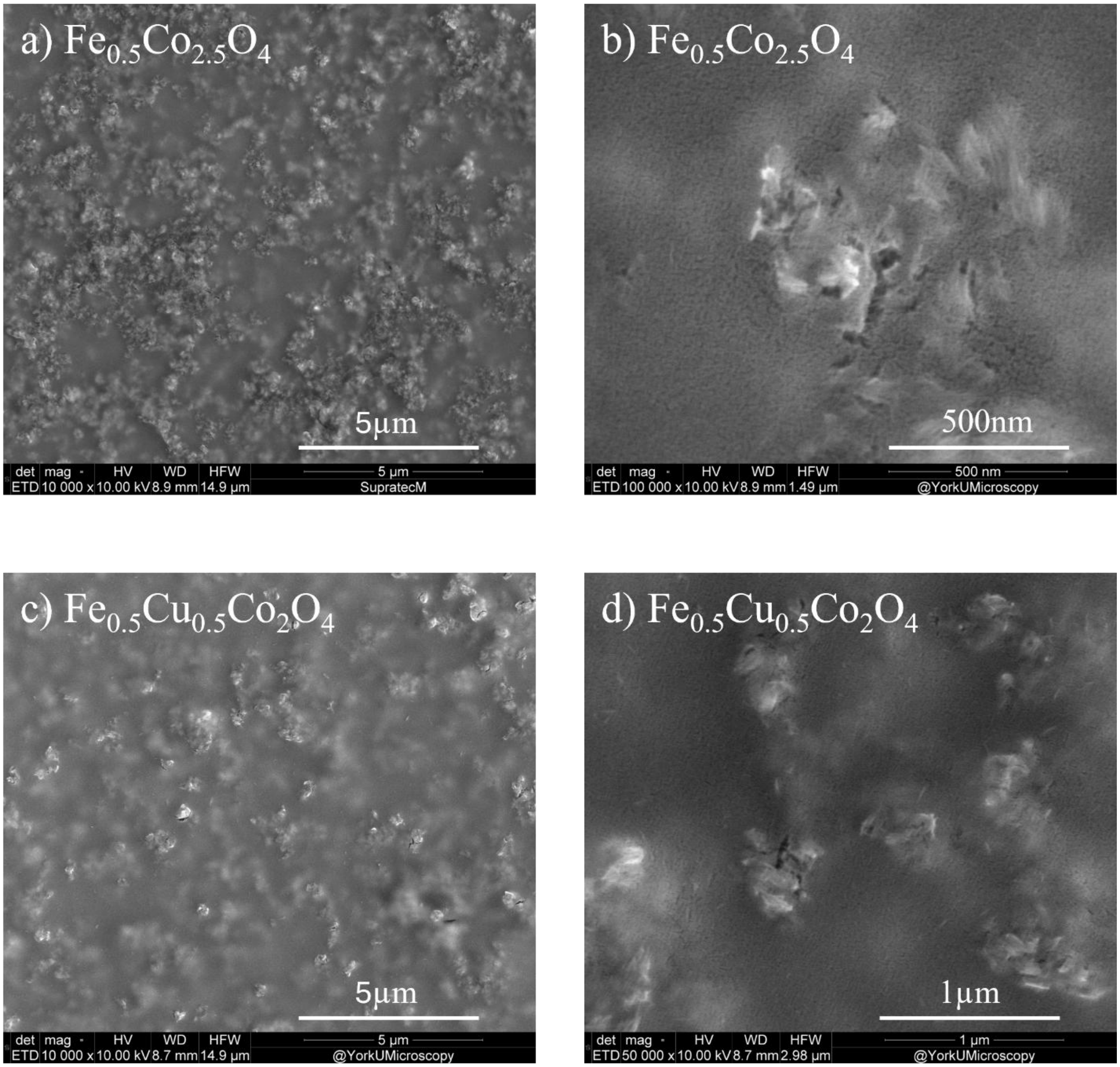

Figure 6. Scanning electron microscopy images of spinel a) and b) $Fe_{0.5}Co_{2.5}O_4$, c) and d) $Fe_{0.5}Cu_{0.5}Co_2O_4$. Samples deposited on FTO glass. Their magnifications are 10000, 50000, and 100000X.

.

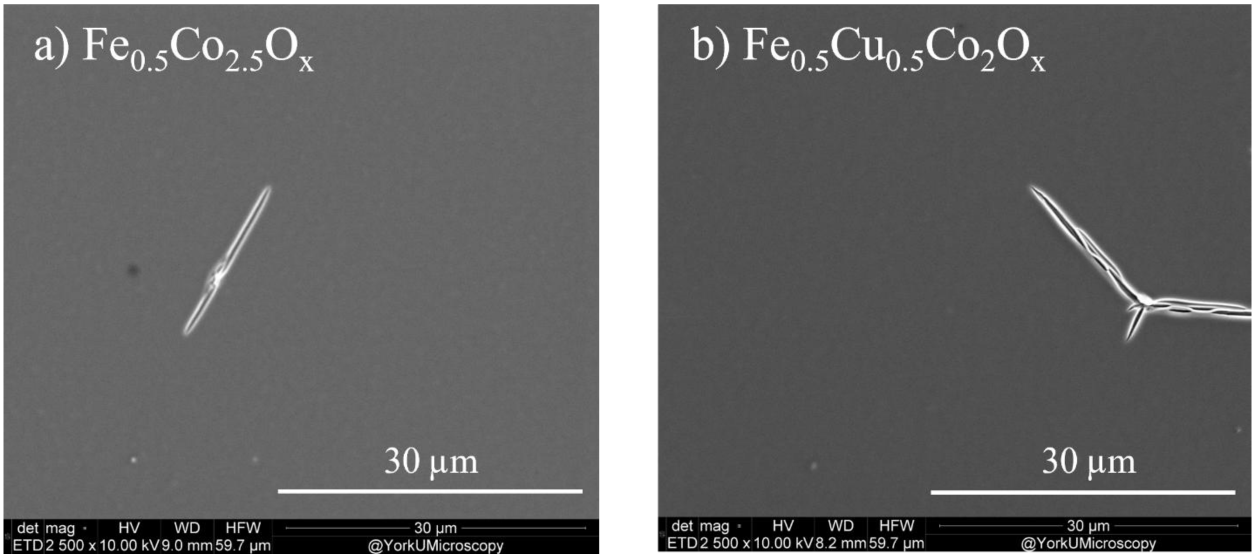

Figure 7. Scanning electron microscopy images of amorphous a) $Fe_{0.5}Co_{2.5}O_X$, and b) $Fe_{0.5}Cu_{0.5}Co_2O_X$. Samples deposited on FTO glass. Their magnifications is 2500X.

4.1.2 EDX results: film composition

Energy dispersive X-ray spectroscopy (EDX) is an analytical technique that can determine the elemental composition of the materials. EDX spectra were obtained for these metal oxides to determine their chemical composition near the surface. An example of EDX spectrum is shown in figure 8 for an amorphous $Fe_{0.5}Cu_{0.5}Co_2O_x$ thin film. The graph displays characteristic peaks associated with the presence of Co, Cu, Fe and O in the material. Also, visible are peaks corresponding to Sn and Si from the FTO glass substrate. Table 2 lists the stochiometric composition and their corresponding EDX compositions for all the samples prepared in this work. There is a good agreement between the EDX and stochiometric compositions. EDX spectra for other samples are placed in Appendix section.

Table 2. Stoichiometric compositions and their corresponding compositions obtained from EDX measurements

Stochiometric Composition	EDX Composition
$Fe_{0.5}Co_{2.5}O_x$	$Fe_{0.62}Co_{2.38}O_x$
$Fe_{0.5}Cu_{0.5}Co_2O_x$	$Fe_{0.65}Cu_{0.57}Co_{1.78}O_x$
$Fe_{0.5}Co_{2.5}O_4$	$Fe_{0.47}Co_{2.53}O_4$
$Fe_{0.5}Cu_{0.5}Co_2O_4$	$Fe_{0.53}Cu_{0.40}Co_{2.07}O_4$
$Fe_{0.5}Ni_{0.5}Co_2O_4$	$Fe_{0.5}Ni_{0.47}Co_{2.03}O_4$

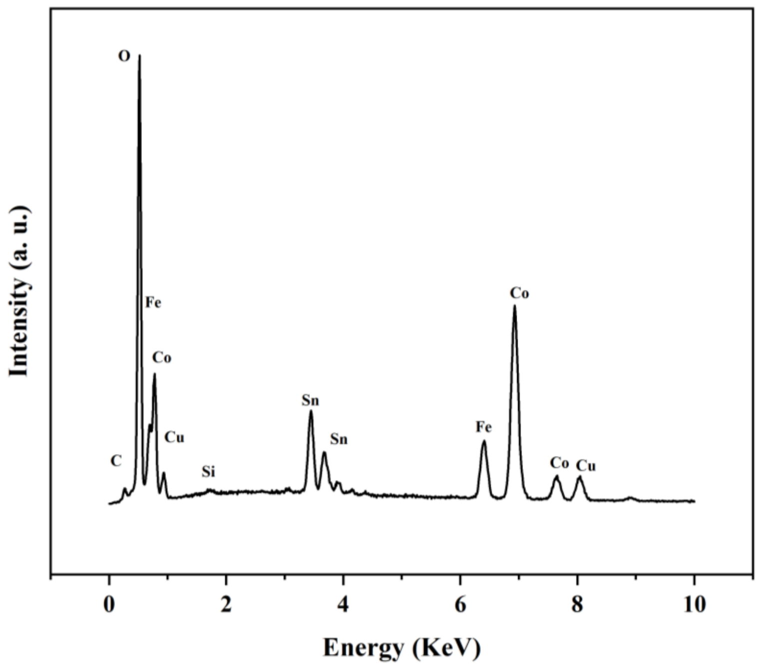

Figure 8. Energy dispersive X-ray spectra of amorphous $Fe_{0.5}Cu_{0.5}Co_2O_x$

Error analysis in EDX is important to confirm the accuracy of the spectra and the elemental composition of the sample. Many factors lead to rise of errors in EDX including but not limited to instrumental errors, contaminations, and errors in sample preparations. One known approach to account for the errors in EDX is correcting through ZAF. This approach which accounts for matrix effects such as atomic number, absorption, and fluorescence uses a mathematical formulation for quantitative error analysis in samples with an internal standard[2]. However, in this work for EDX analysis no standard was measured and due the porous nature of the films, an error as high as 15% is expected[3,4]. The EDX error analysis is described in appendix.

4.1.3 XRD results: film structure

X-ray diffraction is a widely used technique to characterize and identify the bulk composition of the crystalline material. The popularity of this technique comes from its ability to measure the size, shape, and distance between internal crystalline regions[5].

X-ray diffraction patterns were obtained to determine the spinel and the amorphous phase of these cobalt oxides. The amorphous compounds are expected to have very weak pattern or none at all. As seen in figure 9 a (top graph) the amorphous oxides all display the XRD pattern corresponding to the FTO coated glass. The patterns shown in Fig. 9b (bottom graph) are for spinel oxides and they exhibit the characteristics peaks of the cubic spinel structure. The diffraction peaks corresponding to the (111), (220), (311), (222), (400), (422), (511), and (440) planes are shown in figure 9 b. The broad diffraction peak at 20-30 degree is from the glass substrate.

X-ray diffraction data can also be used to investigate the average crystallite sizes of the grain in the sample. For this purpose, the famous Debye-Scherrer's equation[6] was used:

$$D = \frac{0.9\lambda}{\beta Cos\theta} \qquad (4.1)$$

Where D represents the average crystallite size. The wavelength of the radiation X-rays is represented by λ and the full width at half maximum of the diffraction peak (the most intense one) in radians is represented by β. Finally, θ is the Bragg angle which represents half of the diffraction angle[6].

The average crystallite size of the spinel binary and ternary samples in this project are listed in table 3 below. They do not change significantly with composition. The smallest grain size was obtained for $Fe_{0.5}Cu_{0.5}Co_2O_4$ with an average size of 5.24 nm, while the largest grain size was obtained for $Fe_{0.5}Co_{2.5}O_4$ with an average size of 8.53 nm.

Table 3. Lattice parameters and the grain size obtained from XRD measurements for spinel oxides

Sample	Lattice (Å)	Crystallite size (nm)
$Fe_{0.5}Co_{2.5}O_4$	8.1267 ± 0.0006	8.53 ± 0.2
$Fe_{0.5}Cu_{0.5}Co_2O_4$	8.1446 ± 0.0009	5.24 ± 0.3
$Fe_{0.5}Ni_{0.5}Co_2O_4$	8.1427 ± 0.0005	7.18 ± 0.2

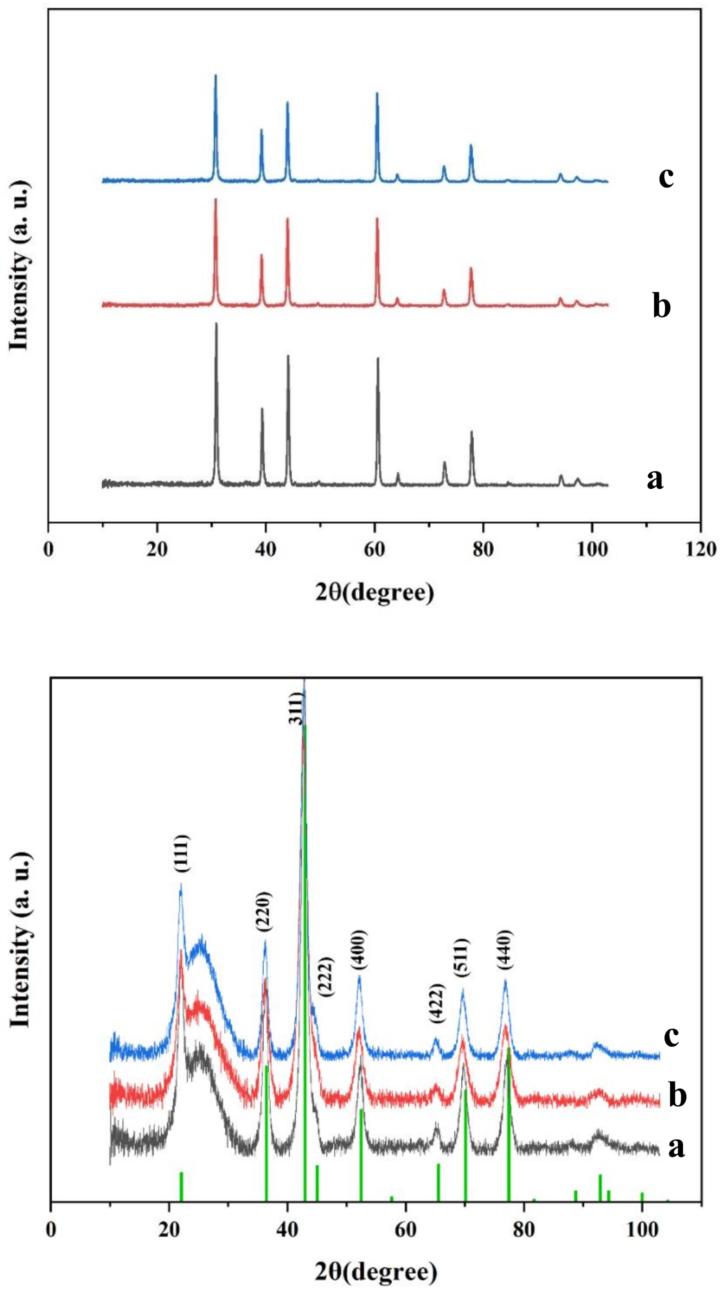

Figure 9. X-ray diffraction images of (top) amorphous oxides: a)FTO glass, b) $Fe_{0.5}Co_{2.5}O_X$, c) $Fe_{0.5}Cu_{0.5}Co_2O_X$; and (bottom) spinel oxides: a) $Fe_{0.5}Co_{2.5}O_4$, b) $Fe_{0.5}Cu_{0.5}Co_2O_4$, c) $Fe_{0.5}Ni_{0.5}Co_2O_4$. The peak assignment (green lines) is from the standard sheet JCPDS-ICDD42-1467.

4.1.4 XPS results: surface composition

XPS is a technique that investigates the surface of the samples. It's a widely used technique in materials and surface science to analyze thin film, catalysts and coatings. XPS is mainly valuable in determining different phases of each metal present at the surface of the sample and providing insights into the oxidation states[7].

Both survey spectra and high-resolution spectra were recorded for each sample in this work. The survey spectra show all the elements that are present in the sample, and according to figure 10 we can see that there is no contamination in the sample. The high-resolution spectra show different species of the metals present at the surface. For example, in this spectrum of O 1s, we see peaks for lattice oxygen, hydroxide, and surface water. In Co 2p spectrum we see different species of CoOOH, spinel and $Co(OH)_2$. Cu also is mainly incorporated in the spinel and hydroxide and for the Fe the major species is the hydroxide in the sample $Fe_{0.5}Co_{2.5}O_4$ and hematite in the sample $Fe_{0.5}Cu_{0.5}Co_{2.5}O_4$.

To analyze the XPS data in this project standard values in literature were employed in assigning peaks to different species. Moreover, these standard values were also used to constrain values such as FWHM and the peak positions. Background correction was performed using Shirley Background. Peak fitting was performed using a Gaussian/Lorentzian (70:30) ratio. Moreover, the area under the peak for each element was normalized by their special atomic sensitivity factor (RSF). To obtain an accuracy of ± 0.1 eV, measurements were taken at different spots on the sample[8].

Both spinel and amorphous oxides have comparable surface functionalities, however XRD does not confirm formation of these phases, therefore the bulk structure differs from the surface for both amorphous and spinel.

Table 4. various species of each element with their corresponding percentages present in $Fe_{0.5}Co_{2.5}O_4$

Peak	Species	Percentage[(a)]	Peak	Species	Percentage[(a)]	Peak	Species	Percentage[(a)]
Co 2p	Spinel	23.75	Fe 2p	Spinel	20.35	O 1s	Lattice	67.37
	$Co(OH)_2$	36.08		Fe_2O_3	29.73		Hydroxide	26.79
	CoO	8.18		FeOOH	49.49		Water	5.84
	CoOOH	31.98						

a: The experimental error is ±0.2

Table 5. various species of each element with their corresponding percentages present in $Fe_{0.5}Cu_{0.5}Co_{2.5}O_4$

Peak	Species	Percentage[(a)]	Peak	Species	Percentage[(a)]
Co 2p	Spinel	30.25	Fe 2p	Spinel	26.44
	$Co(OH)_2$	42.2		Fe_2O_3	52.95
	CoOOH	27.56		FeOOH	20.61
Cu 2p	Spinel	53.53	O 1s	Lattice	67.02
	$Cu(OH)_2$	35.61		Hydroxide	29.91
	CuO	4.5		Water	3.07
	Cu_2O	6.37			

(a): The experimental error is ±0.2

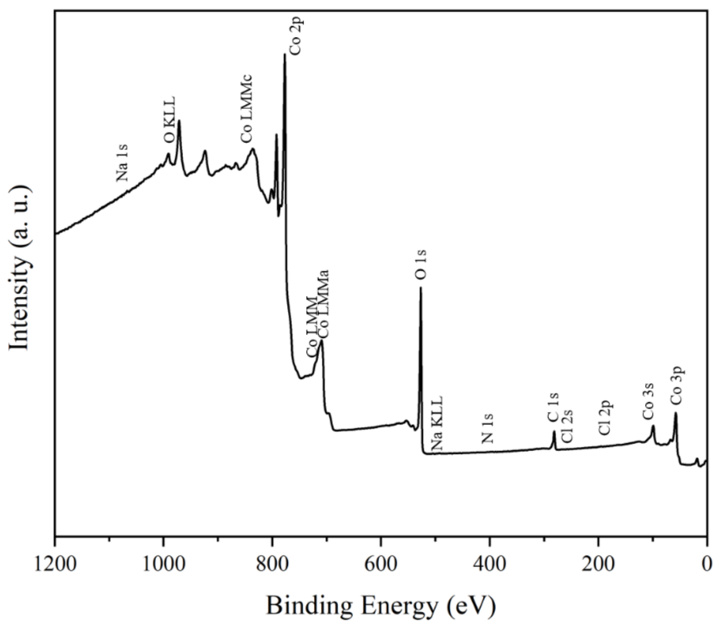

Figure 10. Survey spectrum of $Fe_{0.5}Co_{2.5}O_4$.

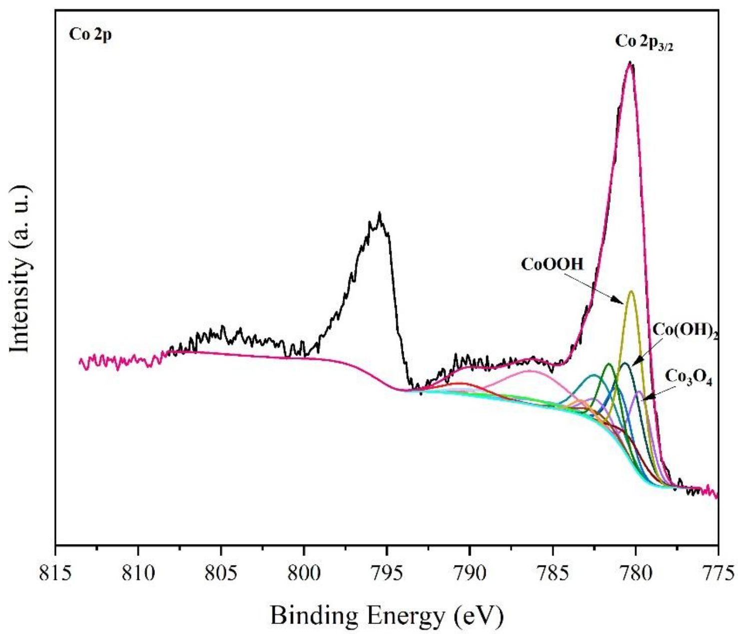
Co 2p
Co 2p$_{3/2}$
CoOOH
Co(OH)$_2$
Co$_3$O$_4$
Intensity (a. u.)
815
810
805
800
795
790
785
780
775
Binding Energy (eV)

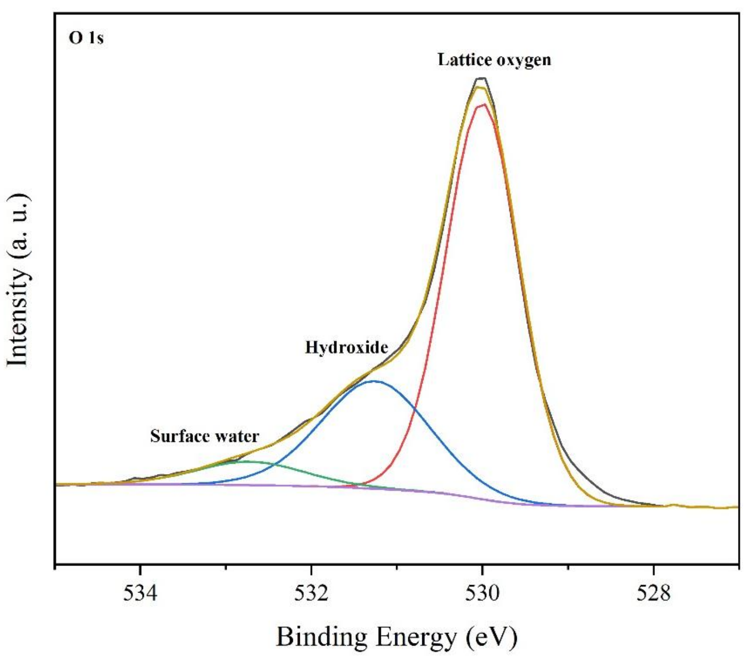
O 1s
Lattice oxygen
Hydroxide
Surface water
Intensity (a. u.)
534
532
530
528
Binding Energy (eV)

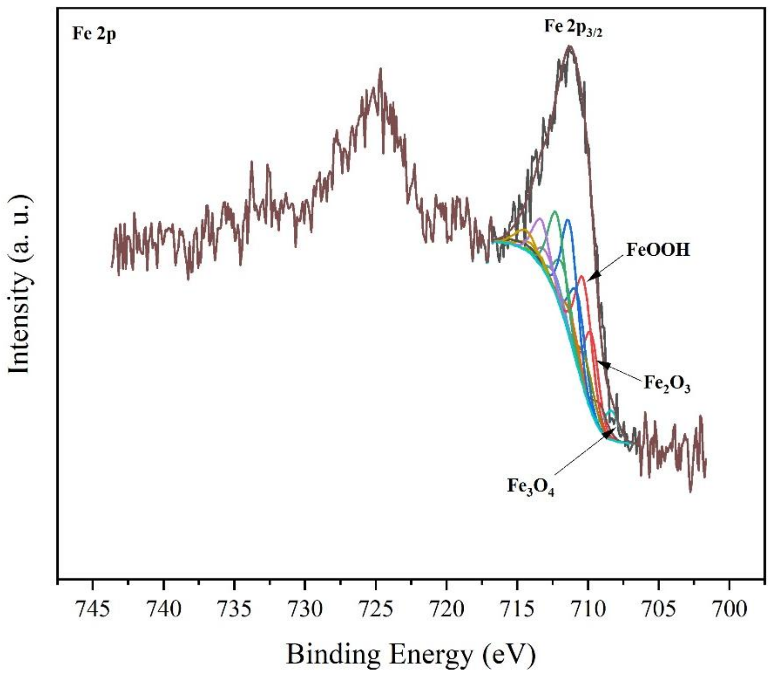

Figure 11. High resolution spectra of Co 2p, O 1s, and Fe 2p.

The shapes of the lines in high resolution spectra of Co 2p, Fe 2p, and O 1s is very similar to the reported XPS for these elements in the literature[9]. According to the spectrum for Co 2p, we see that cobalt is present in the form of Co^{2+} and Co^{3+} ions. In spinel structure, there are two photoelectron peaks and three satellite peaks. In addition, the $Co(OH)_2$, CoOOH, and CoO each possess two photoelectron peaks and two satellite peaks.

Analyzing the high-resolution spectrum of O 1s indicates that the photoelectron peak is comprised of three peaks corresponding to the oxygen in the lattice structure, oxygen in metal hydroxide (a significant amount of oxide was found in the spectra of other metals), and oxygen in the surface water.

Analysis of the high-resolution spectrum of Fe 2p shows that iron is present in different species in the sample. In the spinel structure Fe is present in the form of Fe^{2+} and Fe^{3+} ions and 5 satellite peaks. Magnetite with the chemical formula of Fe_3O_4 is present in our samples 20-27%. In a pure crystal structure of magnetite Fe^{2+} is placed in a tetrahedral hole and Fe^{3+} is placed in an octahedral hole to create a pure spinel structure[10]. Another species that was present in our samples according to the XPS of Fe 2p, is Fe_2O_3 known as hematite with a content of 30-50%. In its pure crystal structure, Fe^{3+} occupies two third of the octahedral holes and creates a rhombohedral corundum structure[10].

Looking at literature for analysis of Fe XPS data, it has been reported that the specific positions of peaks of Fe $2p_{1/2}$ and $2p_{3/2}$ vary based on the charge and oxidation state of iron in the sample[11]. Moreover, Fe 3p XPS spectrum has been analyzed by Mekki et al[12] to find information about different ionic states of iron in silicate glass. Since the peak for the two ionic states of Fe were considered overlapping, they have deconvoluted the peak into two for Fe^{2+} and Fe^{3+}, however, the validity of this method is in question[11].

Another paper by Graat et al[13] investigated the quantitative analysis of XPS spectra for thin iron oxide films. They have employed Tougaard's theory for inelastic scattering of electrons within the sample. This theory basically describes the loss of energy by electrons as they interact with other atoms when travelling through the sample. This causes a broad background signal on the high binding energy side of the spectrum[14]. This paper obtained the XPS spectra of some pure standard powders for Fe^0, Fe^{2+}, and Fe^{3+} and used Tougaard's formula when fitting the peaks for these samples. This formula describes the energy loss function of electron during inelastic scattering after hitting the sample. Its particularly helpful in interpreting the XPS spectra for bulk and surface contributions to the inelastic scattering[14].

As mentioned previously in chapter 3.5 a Shirley background was subtracted from 2p region. The assumption in this background is that the intensity is related to the numbers of electrons emitted at higher binding energies[15]. Its best to be used for core level spectra where inelastic scattering happens mainly because of valence electrons. Moreover, it has lower computational complexity[16]. Comparing with Tougaard's, it assumes that the background stems from the loss of energy that occurs in electron inelastic scattering. It works well with cases that energy losses that occur have a great effect on the shape of the spectra. The downside is that it requires material specific parameters and more complex to implement[16,17].

4.1.5 TEM results: internal structure

Transmission electron microscopy is a widely used technique to obtain information about the internal structure of the materials at high resolution. This technique is mainly popular in materials science and nanotechnology to study the morphology and crystallography of the sample[18].

Both TEM and HR-TEM (high resolution transmission electron microscopy) analysis were performed for $Fe_{0.5}Co_{2.5}O_4$ (both in crystalline and amorphous phase). In order to study the effect of polarization, analysis was performed on post-polarized and pre-polarized samples. Polarization of the samples was obtained by performing a broader range and longer time (than our normal CV) CV scan. The non-polarized samples were analyzed for TEM as they were prepared.

Figure 12 d) and e) display HRTEM images of spinel $Fe_{0.5}Co_{2.5}O_4$ and we see spherical shaped grains, which confirms a higher degree of crystallization compared to a) and b) that are HRTEM images of its amorphous analog. Moreover, we see well-resolved lattice fringes in parts d) and e) that are not present in the amorphous sample. The observed lattice fringe spacing of 0.24 nm corresponds to the plane of 311 and 0.46 nm corresponds to the (111) plane. Both are characteristic patterns of a cubic spinel structure. In addition, selected area diffraction (SAED) patterns were obtained for these samples that show sharp and well-defined rings for the spinel sample in part e) of this figure while, looking at the amorphous sample in part c) these rings are absent. Therefore, the amorphous nature of the sample is further confirmed.

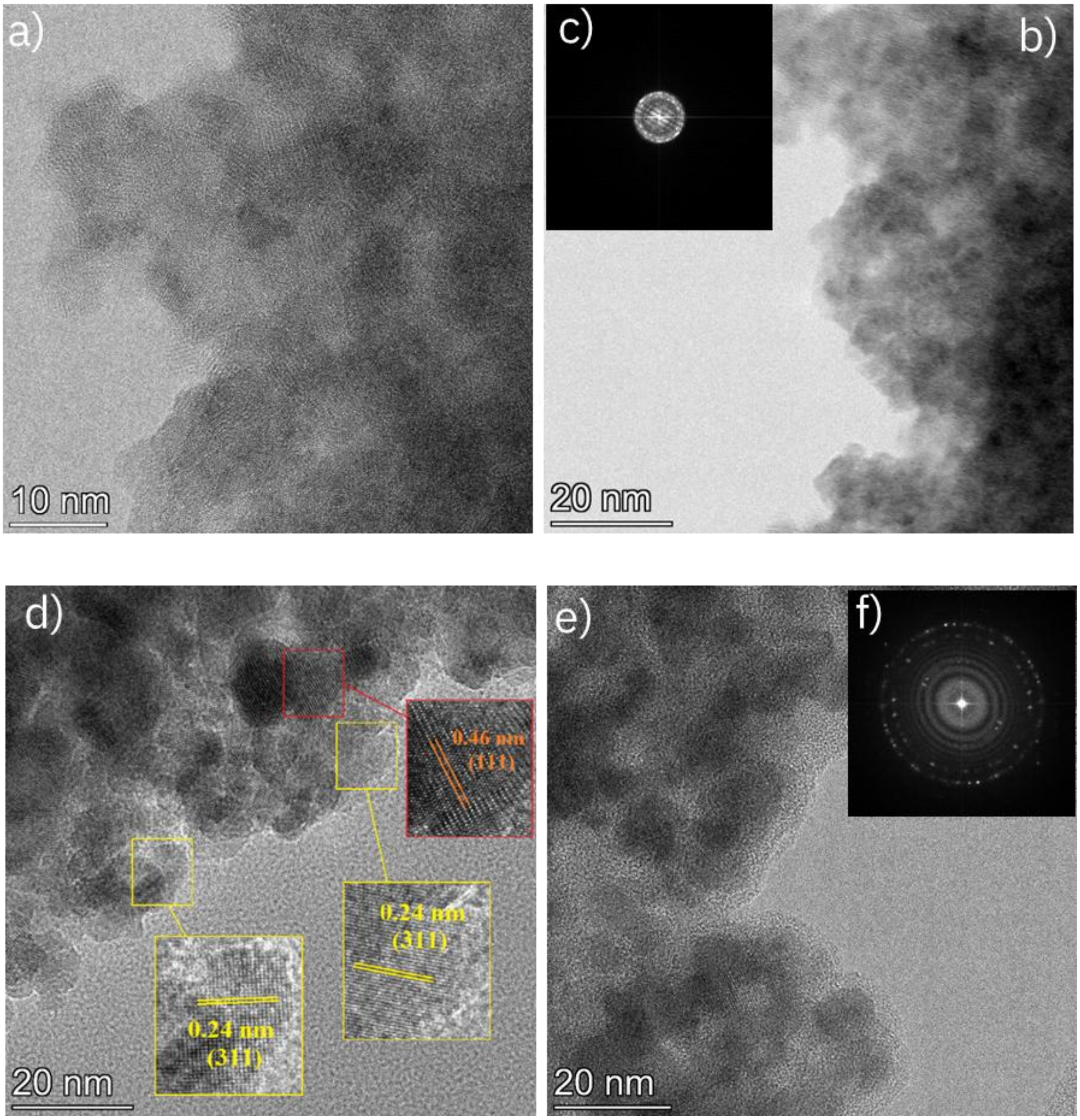

Figure 12. HRTEM images of (a) and (b) $Fe_{0.5}Co_{2.5}O_x$ amorphous samples at different magnifications (c) SAED pattern of $Fe_{0.5}Co_{2.5}O_x$, (d) and (e) $Fe_{0.5}Co_{2.5}O_4$ crystalline sample (f) SAED pattern of $Fe_{0.5}Co_{2.5}O_4$.

4.2 Electrochemical characterization of the Materials

To evaluate the electrocatalytic performance of these materials, electrochemical characterization is performed using CV, EIS, and differential capacitance methods. These methods will provide information regarding the electrochemical behavior and charge storage abilities of the materials.

Cyclic voltammetry was applied to determine the double layer capacitance by cycling at various scan rate and obtaining the current versus potential graph, allowing for the evaluation of the material's ability to store and release charge. These double layer capacitance values also provide a relative measurement of the materials' roughness. Electrochemical impedance spectroscopy was also employed to analyze the frequency-dependent behavior of the catalysts, therefore providing information regarding charge transfer and solution resistances, ion diffusion, and capacitive behavior across a wide range of frequency and applied potential values. Moreover, measuring the differential capacitance will further enlighten our knowledge of the material's surface reactivity and its ability to adsorb and desorb ions during cycling. Finally, a comparison of these techniques provides a comprehensive understanding of the catalyst's electrochemical properties, displaying its potential for applications such as energy storage and catalysis.

4.2.1 CV (capacitance)

In order to investigate the electrocatalytic performance of binary and ternary cobalt oxides prepared in this work, cyclic voltammetry was performed. Cyclic voltammograms (CVs) were used to determine the roughness factor associated with the electrochemically active surface area for each sample. Since each composition has different surface texture and structure, a calculation of the roughness factor allows the comparison of these oxides' electrocatalytic activities from one composition to another and from amorphous to their spinel counterparts. For this purpose, CVs were measured in 1.0 M KOH solution for the potential range of -50 to 50 mV (SCE). In figure 13, a plot of the current density as a function of scan rates (10, 20, 40, 60, 80, and 100 mV/s) will help to determine the anodic/cathodic currents. The positive current of each graph is recorded as the anodic current and the negative as the cathodic current. Plotting these points as a function of scan rates results in straight lines (figure 14). The slopes of these graphs are averaged to determine the double layer capacitance. Using the double layer capacitance and the capacitance of a smooth surface (60 $\mu F\ cm^{-2}$) the roughness factor can be determined[19]. The calculated roughness factors for each sample are summarized for crystalline and amorphous samples in table 6. Pure Co_3O_4 has a roughness of 112 ± 22. While this value increases significantly by introducing Cu and Ni (181 and 353, respectively)[20], adding small amount of iron decreases this value to around 80[20]. Increasing the amount of iron further decreases the roughness factor to approximately 40. The smallest roughness factor (i.e. 32) was obtained for $Fe_{0.5}Co_{2.5}O_4$ which does not include any Cu or Ni. This is in agreement with our previous observations. The highest roughness factors are calculated for the amorphous oxides. This could be due to the broad capacitance region of amorphous oxides.

The error in the roughness factor was estimated by propagating the uncertainties associated with the double-layer capacitance and the capacitance of a smooth surface, in combination with the error in the measured current. The current error was determined as the standard deviation of three data points: the current at 0 mV, along with the values at the immediately adjacent potentials (one above and one below 0 mV).

Table 6. Calculated roughness factor for binary and ternary cobalt oxides

Composition	Roughness factor (R_f)
*Co_3O_4-240°C	211±17
Co_3O_4-300°C	147±15
Co_3O_4-400°C	102±10
Co_3O_x	133±11
$Fe_{0.5}Co_{2.5}O_x$	198±46
$Fe_{0.5}Cu_{0.5}Co_2O_x$	133±33
$Fe_{0.5}Ni_{0.5}Co_2O_x$	300±32
$Fe_{0.5}Co_{2.5}O_4$	32±4
$Fe_{0.5}Cu_{0.5}Co_2O_4$	40±5
$Fe_{0.5}Ni_{0.5}Co_2O_4$	103±12

*This data is taken from my BSc. Honors Thesis.

Another trend that was observed in the table 6, is with regards to the effect of the annealing temperature and the film morphology on the roughness factor of cobalt oxide electrodes. According to this table, as the annealing temperature increases the roughness of the surface decreases. This has been reported in literature for example in a study of CoFeSm thin films on Si substrates. This work demonstrated that by increasing the annealing temperature, the surface became smoother[21].

Moreover, in this thesis, a difference in the roughness factor for amorphous and spinel cobalt oxides were also observed. Typically, amorphous oxides show higher surface roughness than their crystalline counterparts, since the crystalline oxides have a more ordered structure resulting in smoother surface[22].

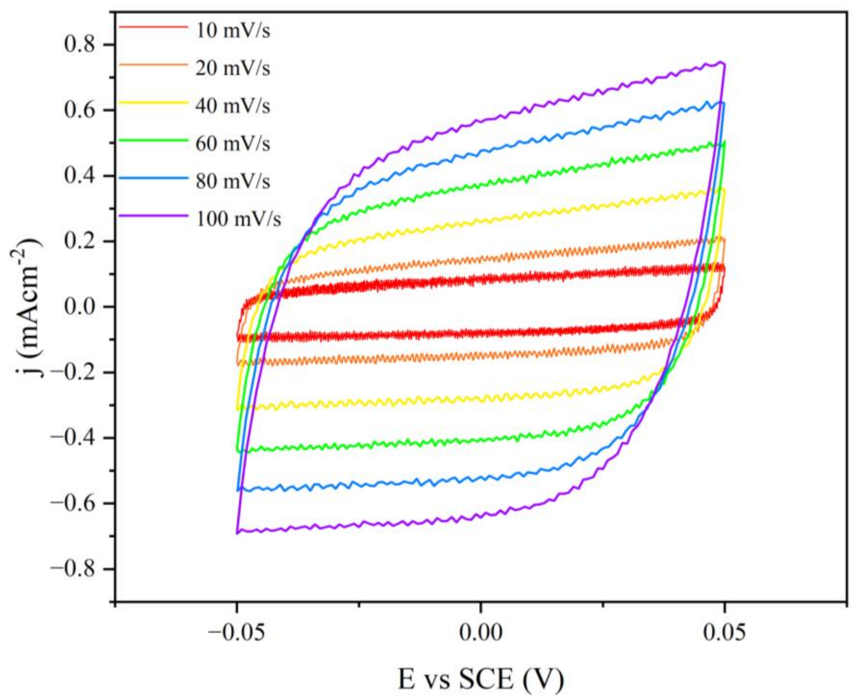

Figure 13. Plots of current as a function of potential difference (-0.5 to 0.5 V) at different scan rates for $Fe_{0.5}Ni_{0.5}Co_2O_4$

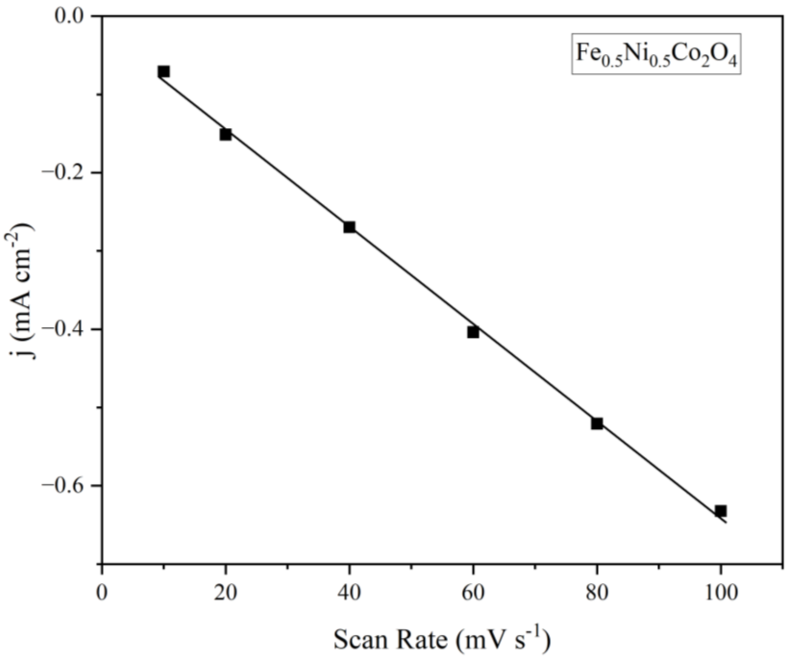

Figure 14. Plot of cathodic current Vs. scan rates for $Fe_{0.5}Ni_{0.5}Co_2O_4$.

4.2.2 Impedance results: total capacitance

Electrochemical impedance spectroscopy is widely known for its ability to simulate and separate the electrochemical current in its real and imaginary components. Fitting of these impedance spectra to an electrical circuit yields numerical values for its elements such as resistances (R) and capacitances (C) using dedicated software. It should be noted that in trying to fit the circuit model to the impedance data, one should ensure that the fit represents a realistic and physically intuitive system accounting for features such as pores and insulating capacitive layers.

Randles circuit is a well-known and widely employed electrical circuit to fit the EIS spectrum. Elements of this circuit include solution resistance (R_s), double layer capacitance (C_{dl}) and the resistance due to charge transfer (R_{ct}). Research into electro and photocatalytic properties of metal oxides has emphasized the significance of morphology, surface defect states, and deliberate surface layer additions to enhance the reactivity. Morphological variations have often been analyzed using basic Randle circuits, where reduced charge transfer resistance correlates with improved catalytic activity. Notably, R_{ct} demonstrates an inverse relationship with the exchange current at each applied potential[23].

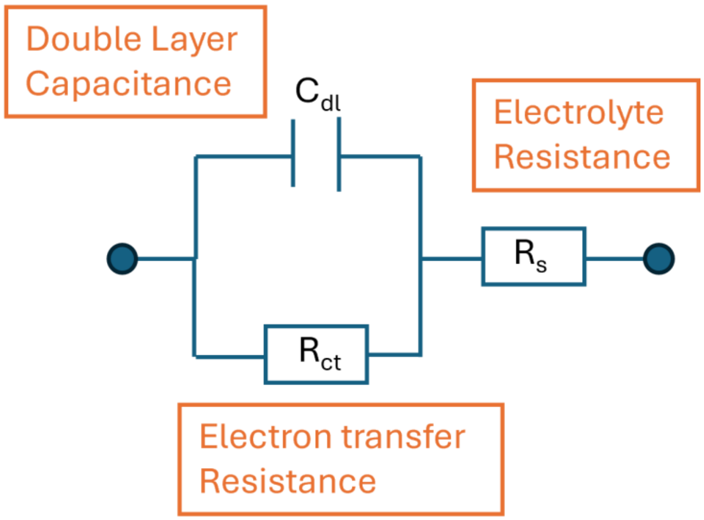

Figure 15. Schematic representation of Randles circuit

This circuit has been used by J. Hu[24] et al. to investigate their NiFeO electrode materials. They have obtained the Nyquist plots at potential of 1580 mV Vs. RHE (1821 mV Vs. SCE) in 1M KOH solution and compared the semicircles with that of NiO and Fe_3O_4. The charge transfer resistance is the smallest for NiFeO which corresponds to the mesoporous structure. This, in turn, offers abundant active edges and vacancy sites which further facilitates electron transfer and reduces mass transport pathways, therefore resulting in enhanced OER activity[24].

Moreover, to study defect sites and surface layers various derivatives of Randles circuit have been explored. In these circuits surface related characteristics are represented by another RC component placed alongside the primary circuit or integrated within, aimed at capturing the bulk properties of these electrodes[23]. Efforts were made to understand the capacitance of defects and surface layers to elucidate their distribution of energy levels. However, this will not account for all the reactions that occur in the electrolyte solution, such as diffusional resistance caused by the electroactive species. This is mainly due to the inherently intricate, multielectron reactions involved during charge transfer with the metal oxide electrode[23].

In this research the electrochemical impedance spectroscopy for $Fe_{0.5}Co_{2.5}O_4$ were carried out in 1 M KOH solution at potentials of -0.1, 0, 0.1, 0.2, 0.3, 0.4, 0.5, and 0.6 V versus SCE. EIS measurements for the rest of the samples were carried at 0 V and at a potential near the onset of the OER. EIS data are shown in the form of Nyquist plots for representative potentials -0.1 and 0.5 V. In this work, initial attention was directed towards the findings acquired at potentials below OER (< 0.4 V) to explore the capacitive behavior of the electrode. Subsequently, the focus was shifted to the potential range involving OER potential (> 0.4 V) to derive kinetic information for the OER.

In figure 18, for potentials smaller than 0.4 V, a sloping line is observed on the Nyquist plot at low frequencies. This is an indication of the capacitive behaviour of the electrode at the electrode/electrolyte interface. The diffusion of charged species into the electrode through pores, could be the reason. Such capacitive behavior at low frequencies is typical when ions intercalate into an inorganic or polymer matrix. On the other hand, in the OER, for potentials 0.5 and 0.6 V a semicircle appears at the low frequency end of the Nyquist plot and its diameter decreases as E (or overpotential, η) increases. In the literature a similar pattern has been reported for cobalt oxide electrodes in 1M KOH solution that are under investigation for OER[25].

After analyzing the experimental findings, the procedure is to use a standard electrical equivalent circuit consisting of two resistive (R and RC), one capacitive (CDC) and one Warburg elements (W) in series and parallel, respectively (figure 16), to analyze the experimental data for potentials -0.1, 0.3 and 0.4 V. For other potentials (0.1 and 0.2 V) the fitting process indicated that the closest match between the experimental and simulated data was achieved when a constant phase element (CPE) replaced the pure capacitance in this circuit model. In the case of CPE two parameters have an influence on determination of impedance: Q that is independent of frequency, and a parameter "a" that shows the deviation from ideal performance with a = 1 for pure capacitive behavior of the element.

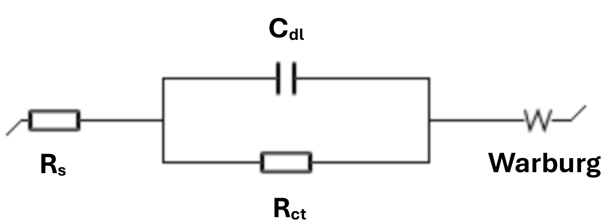

Figure 16. Equivalent circuit employed to fit the Nyquist plots for $Fe_{0.5}Co_{2.5}O_4$ electrode in this work

Nyquist plots corresponding to potentials -0.1 and 0.5V (figure 17), display the best circuit model that was proposed. While other potentials with their closest fit are displayed in the Appendix section, it should be noted that these circuits require further optimization to find the perfect match.

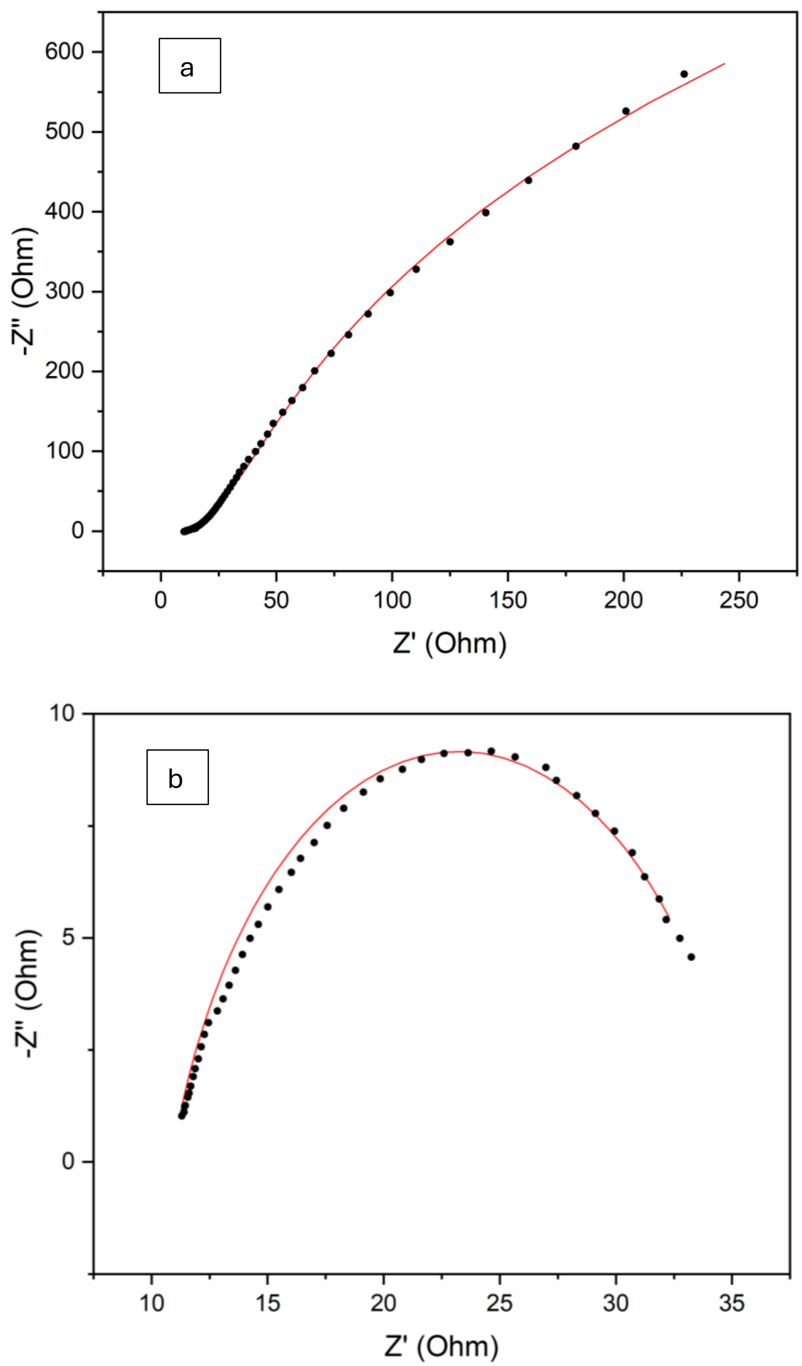

Figure 17. Nyquist plots for a) V=-0.1 V and b) V=0.5 V. The measured data are shown with black dots while the simulated fit is shown with red line.

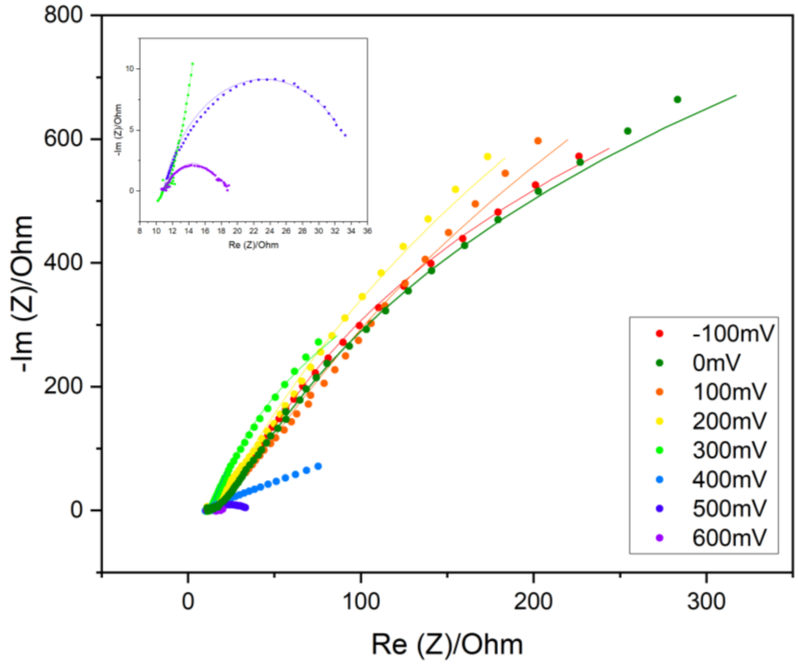

Figure 18. Experimental and simulated Nyquist plots for $Fe_{0.5}Co_{2.5}O_4$ electrode in 1 M KOH at different potentials. The measured data are shown in the form of colored dots and the simulated fit are shown in the form of solid line with corresponding color for each.

Based on the data obtained from fitting the EIS, a graph of capacitance vs. potential was created, as illustrated in figure 19. This curve exhibits a trend similar to the cyclic voltammogram of this electrode (section 4.3.1 figure 20). The peak capacitance occurs around 0.4 V, aligning with the voltametric peak potential. Similar relationships for double layer capacitance and potential have been reported for other crystalline structures of cobalt oxides in alkaline medium[26]. The ascending part of the curve may be due to changes in the double layer caused by the oxidation of Co^{3+} to Co^{4+}. Additionally, the formation of this redox couple is known to be a quasi-reversible process. The slow diffusion of OH^- within the pores contributes to the slow transition rate. Consequently, capacitance values increase exponentially with increasing potential[25].

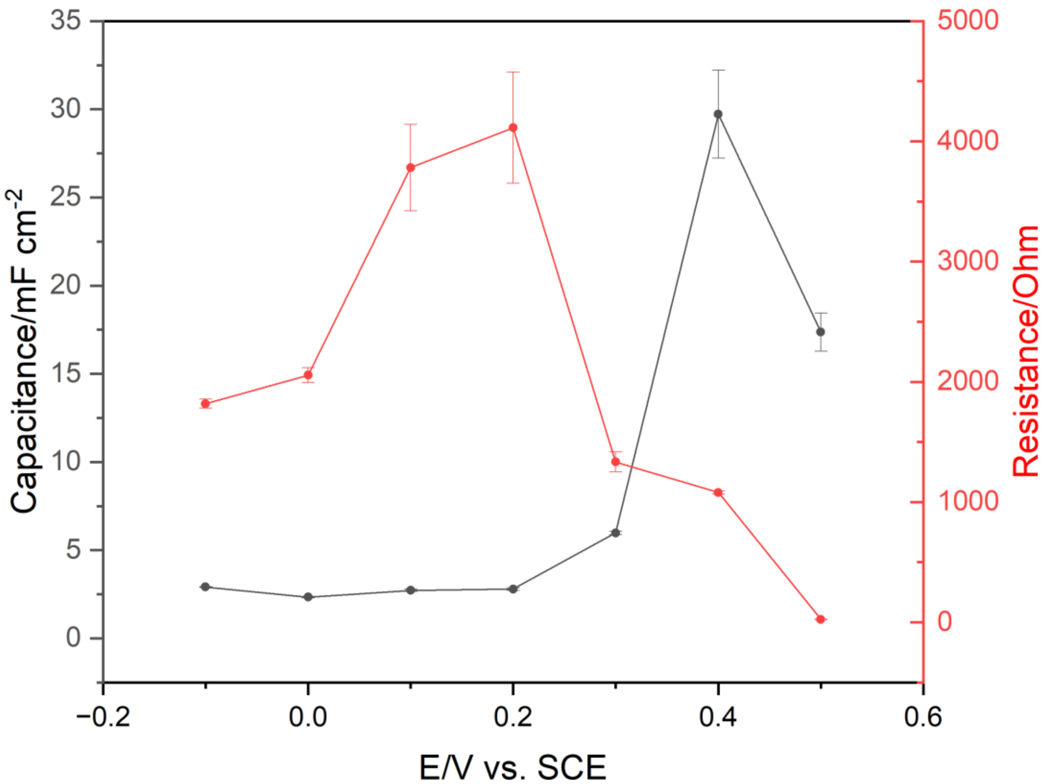

Figure 19. Plot of capacitance (in black) and resistance, R_{ct} (in red) of $Fe_{0.5}Co_{2.5}O_4$ electrode as a function of potential.

.

4.2.3 Differential capacitance

The differential capacitance measurements were conducted for the electrodes at a potential interval of 100 mV and the values are reported in table 7 The capacitance values obtained were normalized for the real surface area (0.983 cm^2) to allow for comparison between different electrodes. No significant trend is observed for different materials. However amorphous oxide materials tend to show higher capacitance values compared to their crystalline counterparts. This indicates that amorphous oxides might be better in providing charge storage ability due to their lack of long-range atomic structure that leads to higher ion diffusion and more active sites[27]. On the other hand, spinel oxides have a more rigid atomic structures which limits the ion diffusion pathways and there are less chances for surface defects and active sites to provide charge storage[28].

Table 7. Obtained values of differential capacitance for different electrodes at every 100 mV interval

Electrodes	-100 mV	0 mV	100 mV	200 mV	300 mV	400 mV
Co_3O_4-300	2.08±0.87 $\mu F.cm^{-2}$	2.75±0.34 $\mu F.cm^{-2}$	4.25±0.69 $\mu F.cm^{-2}$	5.27±1.2 $\mu F.cm^{-2}$	7.07±1.56 $\mu F.cm^{-2}$	18.17±3.45 $\mu F.cm^{-2}$
Co_3O_4-400	1.33±0.7 $\mu F.cm^{-2}$	2.11±0.56 $\mu F.cm^{-2}$	2.98±0.87$\mu F.cm^{-2}$	2.99±0.5 $\mu F.cm^{-2}$	3.31±0.9 $\mu F.cm^{-2}$	8.89±1.3 $\mu F.cm^{-2}$
Co_3O_x	-	0.9±0.1 $\mu F.cm^{-2}$	3.16±0.23 $\mu F.cm^{-2}$	4.13±1.1 $\mu F.cm^{-2}$	7.65±1.3 $\mu F.cm^{-2}$	-
$Fe_{0.5}Co_{2.5}O_x$	0.50±0.1 $\mu F.cm^{-2}$	0.89±0.1 $\mu F.cm^{-2}$	1.91±0.32 $\mu F.cm^{-2}$	4.24±0.95 $\mu F.cm^{-2}$	8.63±1.2 $\mu F.cm^{-2}$	33.70±3.9 $\mu F.cm^{-2}$
$Fe_{0.5}Cu_{0.5}Co_2O_x$	9.08±1.23 $\mu F.cm^{-2}$	7.22±1.1 $\mu F.cm^{-2}$	9.51±1.3 $\mu F.cm^{-2}$	21.55±3.2 $\mu F.cm^{-2}$	108.02±15.9 $\mu F.cm^{-2}$	-
$Fe_{0.5}Ni_{0.5}Co_2O_x$	6.10±0.98 $\mu F.cm^{-2}$	7.11±0.77 $\mu F.cm^{-2}$	9.24±1.23 $\mu F.cm^{-2}$	8.86±0.88 $\mu F.cm^{-2}$	12.86±2.1 $\mu F.cm^{-2}$	14.25±2.3 $\mu F.cm^{-2}$
$Fe_{0.5}Co_{2.5}O_4$	0.37±0.1 $\mu F.cm^{-2}$	0.38±0.08 $\mu F.cm^{-2}$	0.51±0.1 $\mu F.cm^{-2}$	0.80±0.1 $\mu F.cm^{-2}$	2.17±0.45 $\mu F.cm^{-2}$	8.17±0.95 $\mu F.cm^{-2}$
$Fe_{0.5}Cu_{0.5}Co_2O_4$	0.74±0.1 $\mu F.cm^{-2}$	0.74±0.1 $\mu F.cm^{-2}$	0.83±0.1 $\mu F.cm^{-2}$	0.90±0.21 $\mu F.cm^{-2}$	1.31±0.32 $\mu F.cm^{-2}$	3.59±0.76 $\mu F.cm^{-2}$
$Fe_{0.5}Ni_{0.5}Co_2O_4$	-	3.06±0.78 $\mu F.cm^{-2}$	-6.04±1.37 $\mu F.cm^{-2}$	-6.19±1.68 $\mu F.cm^{-2}$	16.61±3.2 $\mu F.cm^{-2}$	24.93±4.1 $\mu F.cm^{-2}$

In almost all cases, an increase in the capacitance value is observed with the rise in potential. This can be attributed to the expansion of the electrochemical double layer at the electrode-electrolyte interface which causes an increase in charge separation and leads to increase in capacitance[29]. Moreover, at higher potential the induced charge at the surface of the electrode increases, therefore the materials ability to store the charge increases[30]. In addition, transition metal oxides are known for their pseudocapacitive behaviors where reversible redox reactions take place at the surface of these electrodes and can contribute to the total capacitance[31].

4.2.4 Comparison between three approaches to determine electrode capacitance

In order to compare three different approaches to determine electrode capacitance, table 8 is constructed. This table lists nine different compositions along with their corresponding capacitance values obtained from EIS (shown as C1, C2, and C total), differential capacitance, and cyclic voltammetry (shown as C_{dl}) at potential 0 V. The values in the table are normalized for real surface area to allow for comparison. Looking at the capacitance values from EIS, C1 and C2 represent circuit elements with C total being their combined value. Almost in all cases, C total is the highest capacitance value. This can indicate that the impedance spectroscopy is picking up contributions from bulk and interfacial effects. A similar trend as stated earlier is observed for amorphous oxides that possess higher capacitance values than their crystalline counter parts in all three methods. Although one thing that should be mentioned for crystalline oxide is that the capacitance value from EIS (C total) is very close to the value obtained from CV as we can see in the last column of the table. As explained earlier, EIS takes into account the charge storage contributions from both the double layer and faradaic reactions, while the capacitance measurements from CV measures only the double layer capacitance so this similarity between the two values indicate that the faradaic contributions are very low at this specific potential (0 V)[32].

Table 8. Capacitance values obtained from EIS, differential capacitance, and CV at 0 V potential for various electrodes

electrode	C_1 (EIS) µF cm^{-2}	C_2 (EIS) µF cm^{-2}	C_{total} (EIS) µF cm^{-2}	C diff.capa. µF cm^{-2}	C_{dl} (CV) µF cm^{-2}	Difference C_{total} and C_{dl}
Co_3O_4-300	24.42	16.28	9.77	2.75	8.8	0.97
Co_3O_4-400	27.47	14.24	9.38	2.12	6.1	3.28
Co_3O_x	9.37	1.06	0.95	0.90	7.9	-6.95
$Fe_{0.5}Co_{2.5}O_x$	51.18	27.62	17.94	0.89	12.5	5.44
$Fe_{0.5}Cu_{0.5}Co_2O_x$	101.00	24.51	19.72	1.93	5.0	14.72
$Fe_{0.5}Ni_{0.5}Co_2O_x$	38.11	-	38.11	7.11	18.0	20.11
$Fe_{0.5}Co_{2.5}O_4$	3.19	-	3.19	0.39	2.0	1.19
$Fe_{0.5}Cu_{0.5}Co_2O_4$	13.22	8.60	5.21	0.74	3.7	1.51
$Fe_{0.5}Ni_{0.5}Co_2O_4$	17.63	9.67	6.25	3.06	6.7	-0.45

4.3 Electrocatalytic properties

One essential approach in evaluating the ability of materials in energy storage and conversion, is to understand their electrocatalytic performance. This chapter section presents these results and provides an understanding of these behaviours for various electrodes materials (binary and ternary spinel oxides) with the aid of techniques such as cyclic voltammetry, linear sweep voltammetry and Tafel measurements. Cyclic voltammetry gives information about the redox characteristics and the stability of the electrode. Linear sweep and Tafel measurements will provide information regarding the OER mechanism and charge transfer efficiency.

4.3.1 CV results

The electrocatalytic performances of these catalysts were evaluated by cyclic voltammetry. Cyclic voltammograms were recorded in 1M KOH from -100 to 1000 mV (SCE) at scan rate of 50 mV/s. Using the roughness factor the current density was corrected in order to compare electrocatalytic activity of different compositions. According to figure 20, $Fe_{0.5}Cu_{0.5}Co_2O_4$ spinel oxide possesses the highest current density of about 0.9 $mAcm^{-2}$ at a potential of 1V (SCE) indicating higher redox activity and charge transfer ability. This is followed very closely by $Fe_{0.5}Co_{2.5}O_4$ while the second place is owned by $Fe_{0.5}Ni_{0.5}Co_2O_4$ with ~0.4 $mAcm^{-2}$ current density. These iron incorporated spinel oxides have far greater current densities than pure cobalt oxides with a current density of less than 0.2 $mAcm^{-2}$. It suggests a role of iron incorporation in improving catalytic activity[33]. However, it should be noted that these values are reported without iR drop correction and the assumption here is that the resistances of the electrolyte solution and the catalyst thin film are similar across the sample. The results were expected as in a previous study, Morin's group showed that addition of Fe to cobalt spinel oxides have improved catalytic activity and replacing Cu with Ni in $Cu_xCo_{3-x}O_4$ has a detrimental effect[20].

Moreover, the paper by Yang *et al*[34], also discusses the role of iron in the binary of $FeCo_2O_4$ spinel oxides. This paper indicates that Co^{3+} ions are favorable for OER since they can preferably absorb OH^-. They also state that when ferric ions substitute cobalt cations in the spinel lattice, it alters the Co 3d electron delocalization and spin state transformation. Due to a combination of charge and spin effects, the Fe^{3+} ions can activate their neighbouring cobalt cations and improve the intrinsic catalytic activity of $FeCo_2O_4$ spinel oxides[34].

Interestingly, Wang *et al*[35] presented the idea of interface engineering in their recent paper for a $NiCo_2O_4$ catalyst. This catalyst was tailored to posses both amorphous and spinel heterogenous interfaces, so their catalyst benefited from the advantages of both phases. The main positive point for an amorphous structure is having a high number of oxygen vacancies and surface defect sites which can act as active sites. Therefore, increasing the adsorption of water molecules and enhancing catalytic efficiency. On the other hand, crystalline phase increases the electrical conductivity and promotes the speed of electron transfer during the two half reactions of water splitting, OER and HER. In addition, they have also performed DFT calculations which suggests that the presence of oxygen vacancies changes the coordination of the catalytic center thereby decreasing the Gibbs free energy of the potential-determining steps in OER and HER[35].

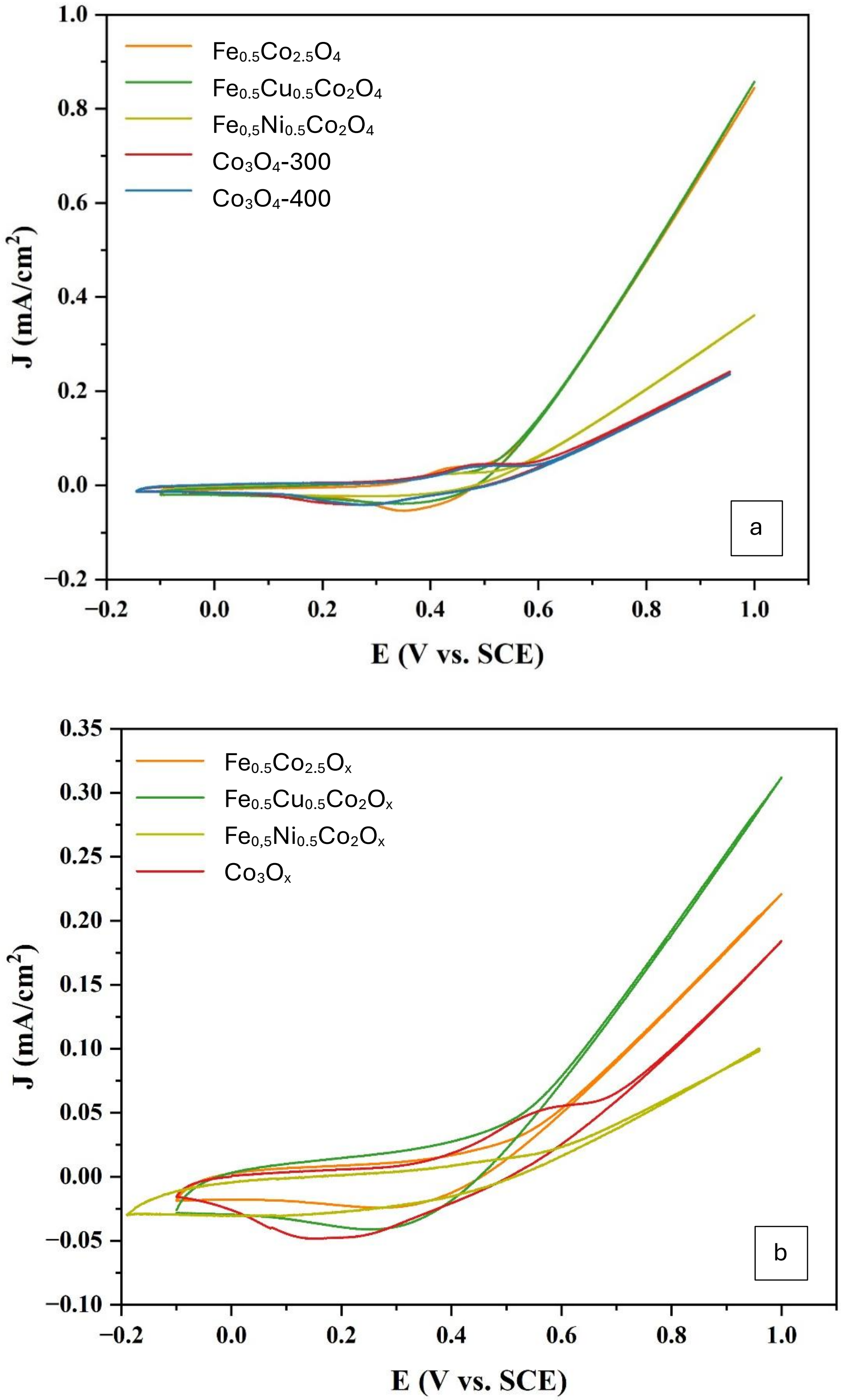

Figure 20. Cyclic voltammograms of a) spinel oxides and b) amorphous oxides prepared in this work, measured at 1M KOH at scan rate of 50 mVs^{-1}.

A comparative analysis on these oxides shows that the amorphous oxides have lower electrocatalytic performance than their crystalline analogous in terms of their current density. These finding states that even though amorphous oxides have higher surface area, they probably have lower electronic conductivity.

When the CV data were corrected for iR drop to account for the potential drop originated from the internal resistance of the system, a potential of 700mV versus SCE was chosen to compare the OER current density of the various samples. At this potential the current density for $Fe_{0.5}Cu_{0.5}Co_2O_4$ is the highest and is closely followed by $Fe_{0.5}Co_{2.5}O_4$ while $Fe_{0.5}Ni_{0.5}Co_2O_4$ has the lowest current density among these iron containing spinel oxides indicating that Ni has a detrimental effect on catalytic activity in cobaltite spinel oxides. Overall, amorphous oxides have lower catalytic activity than their crystalline counterparts, as was observed in earlier graphs. Figure 21 shows the cyclic voltammograms of $Fe_{0.5}Co_{2.5}O_4$ electrode corrected for iR drop while the current is a) as obtained from the experiment and b) corrected for the real surface area to be able to compare with different compositions. The graphs of other compositions are shown in the appendix. In order to compare the catalytic activity of metal oxides we should consider two components, extrinsic and intrinsic activity. Each is divided into few sub-components. For example, for extrinsic activity we should consider loading of the sample, surface area of the film and the matrix. For intrinsic activity components such as nature of the active sites, number of the active sites and mechanism should be considered. When we correct for the iR drop, it in fact is a correction within the intrinsic activity while the surface area correction (using Rf) is a correction in extrinsic activity components.

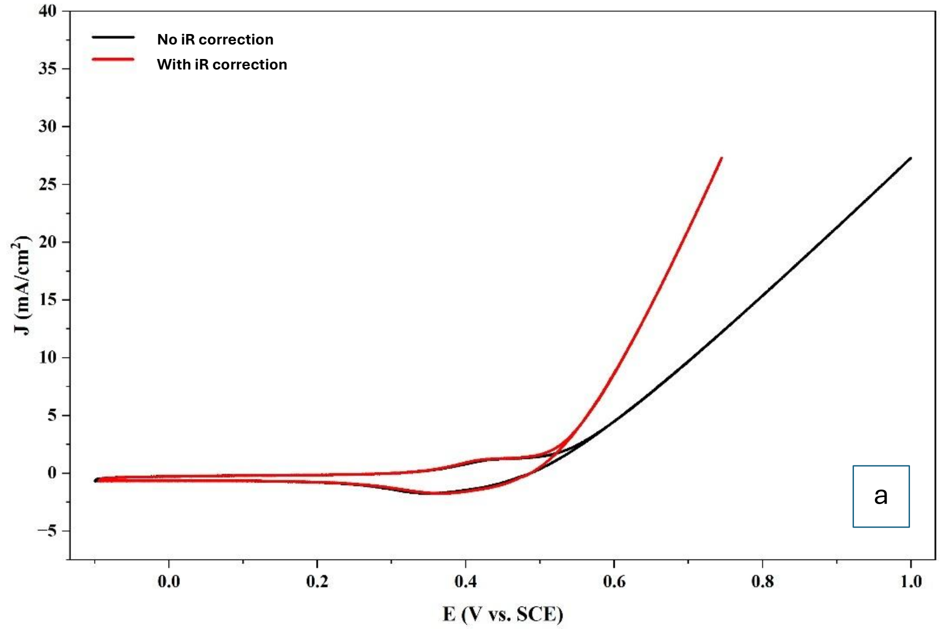

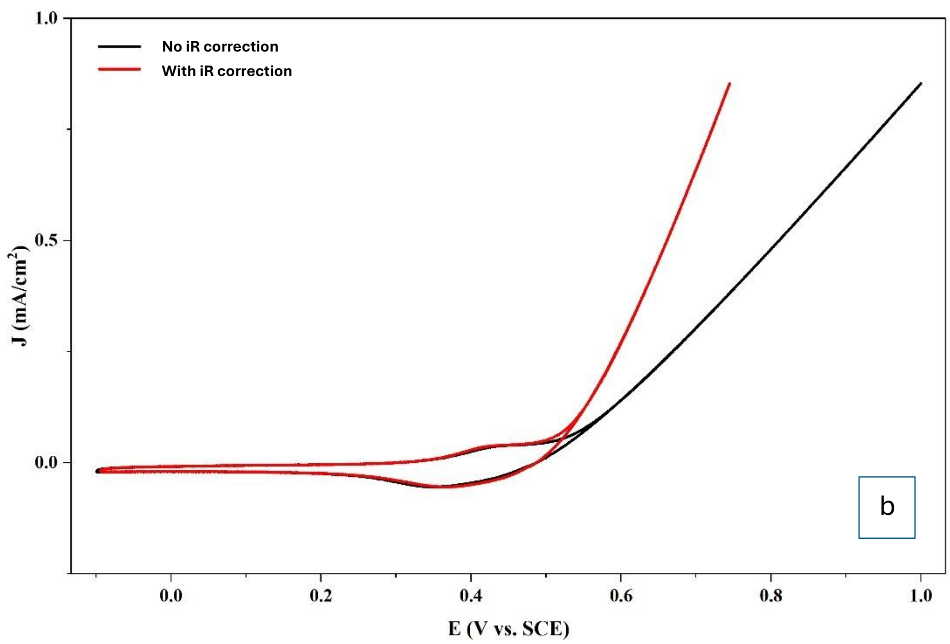

Figure 21. Cyclic voltammograms of $Fe_{0.5}Co_{2.5}O_4$ electrode corrected for iR drop measured at 1M KOH at scan rate of 50 mVs^{-1} and a) geometric area b) real surface area (roughness factor).

Several reports in literature have also applied iR drop correction to CV data to account for the voltage losses that can negatively affect the electrocatalytic performance of metal oxides. For example, the paper by Zhang *et al*[36] which investigated the OER activity of Co_2FeO_4 and $CoFe_2O_4$ nanoparticles mentions using the ohmic correction for CV curves. However, this important tool for accurate determination of catalytic activity parameters (overpotentials, Tafel slope, etc.) has its own challenges. One of the challenges is to accurately calculate the solution resistance through impedance which depends on many factors such as the morphology of the electrode, concentration and composition of the solution, and the heterogenous nature of the electrode. An incorrect R value can lead to miscalculation for ohmic drop and create misshaped curves and Tafel slopes[37]. Moreover, when gas evolution or rapid potential sweep is happening, the resistance of the interface changes quickly and this further complicates applying the static ohmic drop correction[38]. Furthermore, use of the on-the-fly modes such as positive feedback and current interrupt can add to the noise and stability issues and lead to preventing a true catalytic response. It has been suggested to apply only 80% of the resistance value to account for some of the errors associated with the overcorrection of the ohmic drop[39].

4.3.2 Kinetic studies an Tafel measurements

In this section, the electrocatalytic performance of these electrode materials that were investigated through linear sweep voltammetry and Tafel studies, are presented. The LSV curves were recorded for all spinel oxide electrodes at rotation speeds of 500 rpm, 1000 rpm, 1500 rpm, 2000 rpm, 2500 rpm, and 3000 rpm. The electrolyte solution was 0.1 M KOH, and the scan rate was 2 mV/s. More details are available in Chapter 3, section 3.8. Figure 22 shows the LSV curves at various rpm for $Fe_{0.5}Co_{2.5}O_4$. A trend that is followed in these figures for all of the electrodes, is that by increasing the electrode rotation speed, the current density increases. This can be explained by an enhanced transport of oxygen containing species flux to the surface as the electrode rotates faster. In other words, when the disk electrode rotates at higher speeds, mass transport is improved because of a decreased thickness in the diffusion layer. This results in more oxygen containing species flowing towards the surface. Moreover, since there is no significant divergence from the expected trend for rotation speeds above 500 rpm (see Figure 22), this could indicate that the electrode has a stable catalytic performance through various speeds[40]. Increase rotation speed can also help dislodge oxygen gas bubbles from the surface maintaining the active surface area free from gas bubbles.

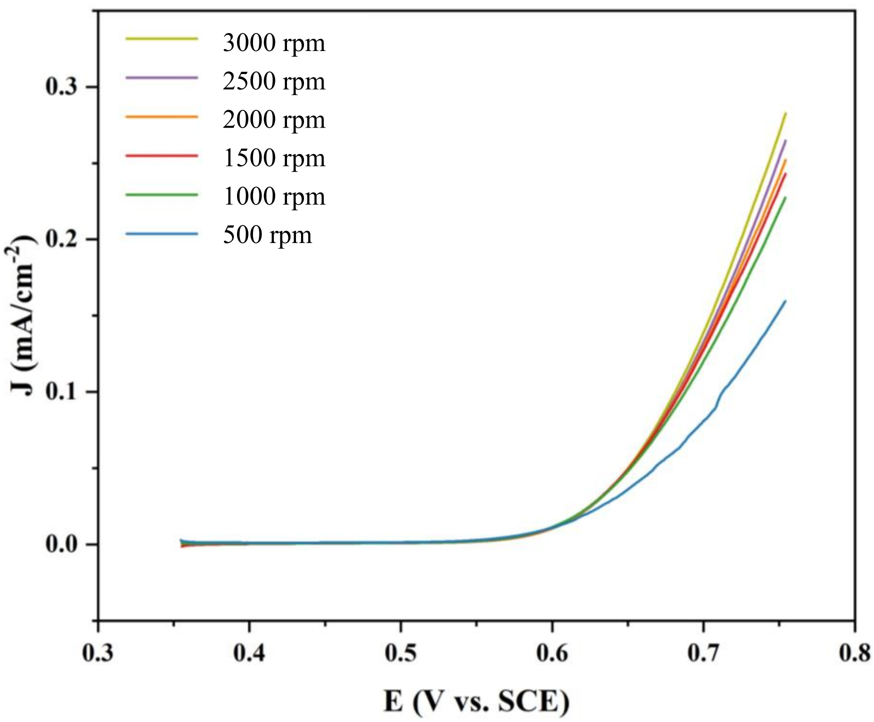

Figure 22. LSV curves of $Fe_{0.5}Co_{2.5}O_4$ at different rotation rates in 0.1 M KOH electrolyte solution.

Tafel slopes were calculated using the LSV curve at 3000 rpm. Figure 23 shows the graphs of overpotential versus log of current density for $Fe_{0.5}Co_{2.5}O_4$ at 0.1 M KOH solution. The slope of the most linear part of this graph is the Tafel slope. The current density has been corrected for the real surface area and the potential has been corrected for the iR drop. All the other Tafel slope graphs are presented in Appendix section 3 and their values are listed in table 9. Tafel values range from 64.4 $mV.dec^{-1}$ to 96.5 $mV.dec^{-1}$, indicating that there is not a significant change in the mechanism of OER with change in composition. The lower the value of the Tafel slope, the faster is electron transfer kinetic and improved catalytic activity. Among the electrodes listed in the table, $Fe_{0.5}Co_{2.5}O_4$ has the lowest slope with 64.4 $mV.dec^{-1}$ suggesting that it has the most favorable charge transfer characteristics. $Fe_{0.5}Cu_{0.5}Co_2O_4$ follows closely (69.8 $mV.dec^{-1}$) indicating the role of copper in enhancing the catalytic activity[41]. On the other hand, $Fe_{0.5}Ni_{0.5}Co_2O_4$ has the highest value (96.5 $mV.dec^{-1}$) indicating the detrimental effect of nickel incorporation on charge transfer activity. This observation is similar to literature reports. For example, this study on nano spinel $Ni_{0.8}Co_{0.2}Fe_2O_4$ has reported a Tafel value of 79 $mV.dec^{-1}$ in 1 M KOH solution which is higher than its non-nickel doped counterparts[42], indicating this negative effect of Ni doping on Tafel slope and charge transfer efficiency[43]. Pure Co_3O_4 has shown a moderate Tafel of 84.5 $mV.dec^{-1}$ confirming that with adding iron and copper, electrocatalytic activity will enhance and with incorporating nickel it will be slowed down. Numerous studies have reported the Tafel values for cobalt iron spinel oxides ranging from 40 to 60 mV.dec^{-1} suggests that Fe doping is favorable for OER kinetics[44]. For example, a study on iron doped cobalt oxide nanoparticles reported a Tafel slope of 70 mV.dec^{-1} in 1 M KOH solution, which is much lower than the value reported for pure Co_3O_4 (124 mV.dec^{-1})[45].

Moreover, Tafel slope values close to 60 mV.dec^{-1} suggest that in the mechanism that is at play, the rate determining step (RDS) is a chemical reaction with the first electron transfer. According to the table below, this could be the mechanism for $Fe_{0.5}Co_{2.5}O_4$ and $Fe_{0.5}Cu_{0.5}Co_2O_4$ with 64.4 and 69.8 mV.dec^{-1} respectively. A Tafel slope value of 120 mV.dec^{-1} suggests that RDS is not chemical but an electrochemical reaction occurring with the first electron transfer step. For the other Tafel values in the table that are close to 90 mV.dec^{-1}, it is not easy to determine their mechanisms as there could be more than one mechanism at play and what we measure may in fact be an average of more than one slope values. There are many reasons that could come up here for this, such as alteration in film resistance with a change in potential. As we oxidize the nanoparticle material its property changes. Moreover, the surface is not in a continuous phase everywhere. Iron rich or cobalt rich particles might follow different mechanism and therefore different Tafel slopes. This analysis is in line with our previous work in Dr. Morin's group[46].

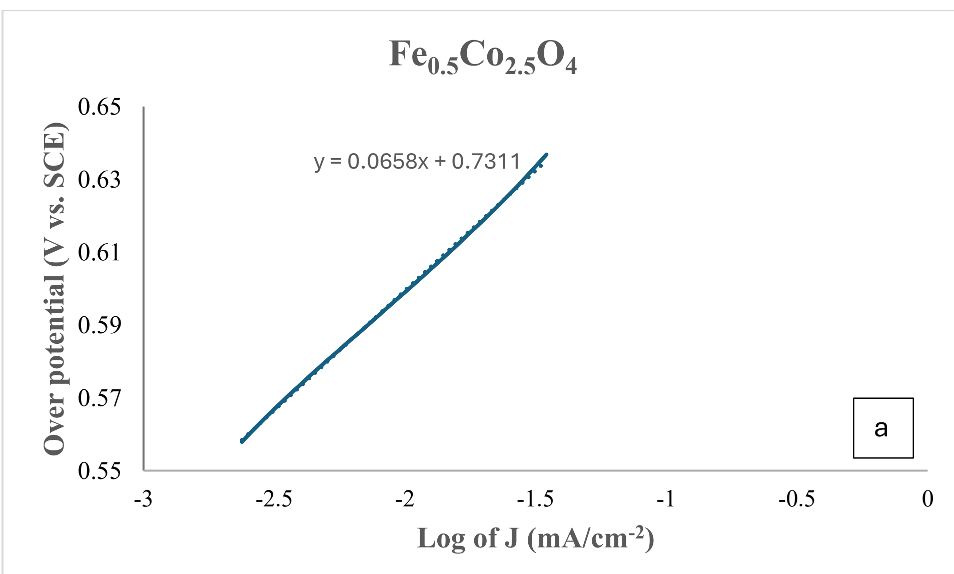

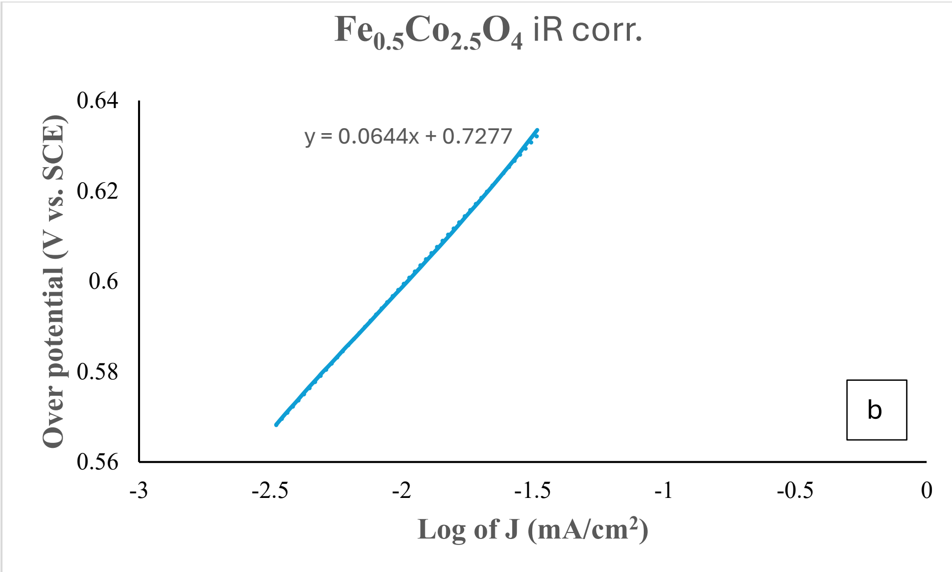

Figure 23. Tafel slopes of $Fe_{0.5}Co_{2.5}O_4$ in 0.1 M KOH solution at 3000 rpm where the potential is a) as recorded and b) corrected for iR drop.

Table 9. Tafel slopes of electrodes

Sample	Tafel slope ± 10 mV/dec
Co_3O_4	84.5
$Fe_{0.5}Co_{2.5}O_4$	64.4
$Fe_{0.5}Cu_{0.5}Co_2O_4$	69.8
$Fe_{0.5}Ni_{0.5}Co_2O_4$	96.5

4.3.3 Correlations between structural, electrochemical, and catalytic properties

One of the main reasons behind this study is to design a good electrocatalyst to overcome the barriers in water electrolysis reaction. This requires a deeper understanding of the electrocatalytic performance of the synthesized electrodes. Therefore, a comparative analysis of capacitance, current density, roughness factor, lattice and crystallite size was conducted. The relationship observed between these parameters can provide insight into the effect of surface structure and composition on the catalytic performance and activity. This section includes correlations between these parameters and discusses further effect of adding iron and difference in performance activity of crystalline versus amorphous oxide electrodes.

In figure 24 the graph of lattice parameters versus crystallite size is plotted for spinel oxide sample prepared in this work ($Fe_{0.5}Co_{2.5}O_4$, $Fe_{0.5}Cu_{0.5}Co_2O_4$, and $Fe_{0.5}Ni_{0.5}Co_2O_4$) and other samples prepared in the Morin's group. This graph shows an inverse relationship between lattice parameters and crystallite size for these electrodes with an adjusted coefficient of determination (r^2_{adj}) of 0.72. One reason for this could be the influence of lattice strain. Crystallites with smaller sizes tend to face larger strain because of defects and grain boundaries. The experienced strain can deform the lattice and various lattice parameters can be generated[47]. This has been reported in a study on $Ba_{1/4}Sr_{3/4}MnO_3$ layered perovskites magnetite. According to this study, a decrease in the crystallite size can result in an increase in the lattice strain and altered parameters[47].

Another finding based on this graph is that by increasing the iron content, lattice parameter increases and the crystallite size decreases. The lattice parameter changes linearly with the ionic radii of the cations involved. Substituting Co^{3+} with Fe^{3+} will lead to an increase in the lattice parameter[48]. Furthermore, increasing the iron content increases strain and defects leading to a disruption of crystal growth[49]. Increasing the annealing temperature might reduce this effect, however iron rich spinels show smaller crystallites compared to their non-iron counterparts[48].

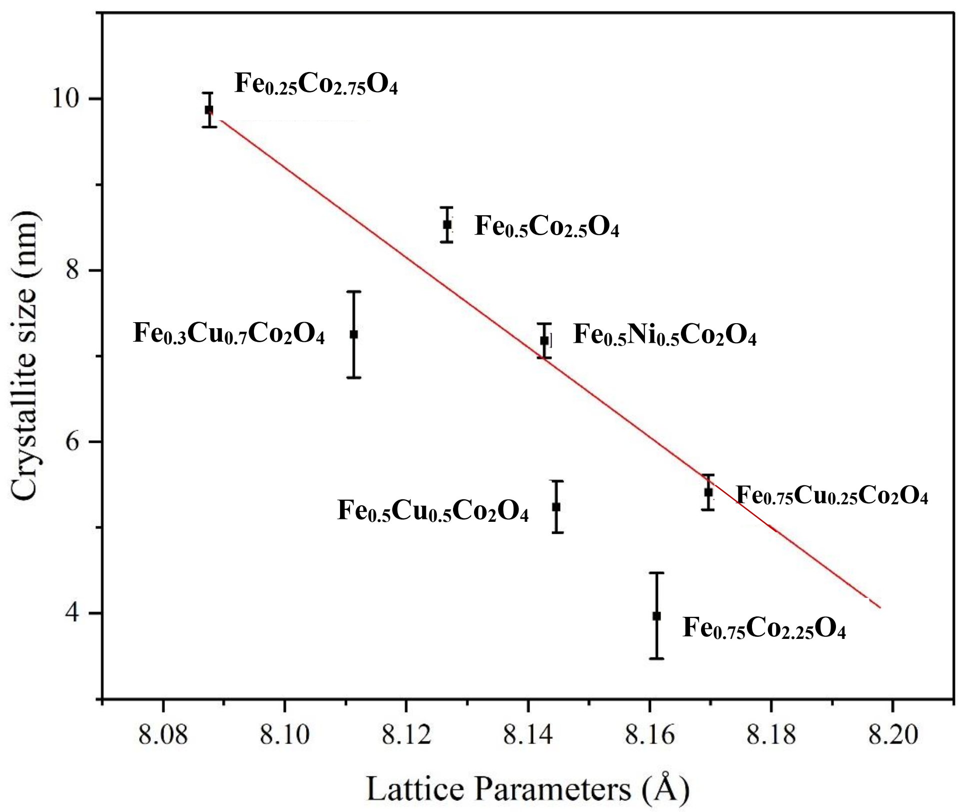

Figure 24. Graph of crystallite size plotted as a function of lattice parameters for spinel oxide electrodes

In figure 25 the graph of current density versus lattice parameters is plotted for the same spinel oxides as above. The current is reported at 1V Vs. SCE and it was measured in 1 M KOH electrolyte. It is then corrected for the geometric area and roughness factor. While there is no significant correlation, the current density tends to decrease with an increase in the lattice parameter. The alteration in lattice parameters can influence the electronic properties of the material and therefore can lead to changes in the adsorption and desorption of the oxygen containing intermediates during the OER, and give rise to modifications in the catalytic properties[50].

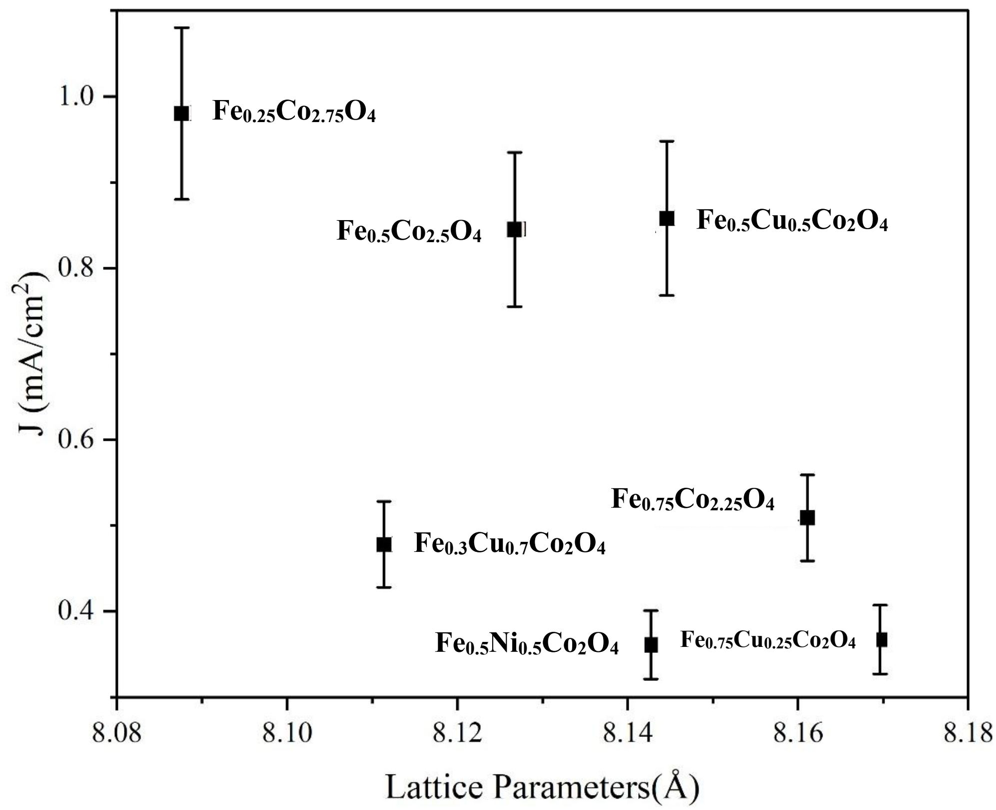

Figure 25. Graph of current density is plotted as a function of lattice parameters for spinel oxides

Figure 26 shows plots of current density and the double layer capacitance for amorphous oxide electrodes. The current is reported at 1V Vs. SCE and it was measured in 1 M KOH electrolyte. This current density is corrected for the geometric area but not the roughness factor (figure 26 a). While this limited data does not display a correlation between catalytic current and capacitance. Increasing the number of data points (which is achieve by increasing the number of spinel composition) does lead to a correlation as seen in Ref. 52. Amorphous oxide electrodes show an increase in current density as the capacitance increases, which demonstrates that the surface area is the main contributing parameter for increasing the current density in amorphous oxides[51]. However, if we take the surface roughness factor into account and correct the J values for the roughness of the electrodes surface by dividing the current by Rf values (figure 26 b), the graph changes drastically. It shows an inverse relationship between capacitance and the current density[52]. This could be due to limitations in diffusion at higher current densities which can limits the transport of the electrolyte ions into the bulk of the active materials. This leads to inaccessibility of the surface-active sites for charge storage and reducing the capacitance[51].

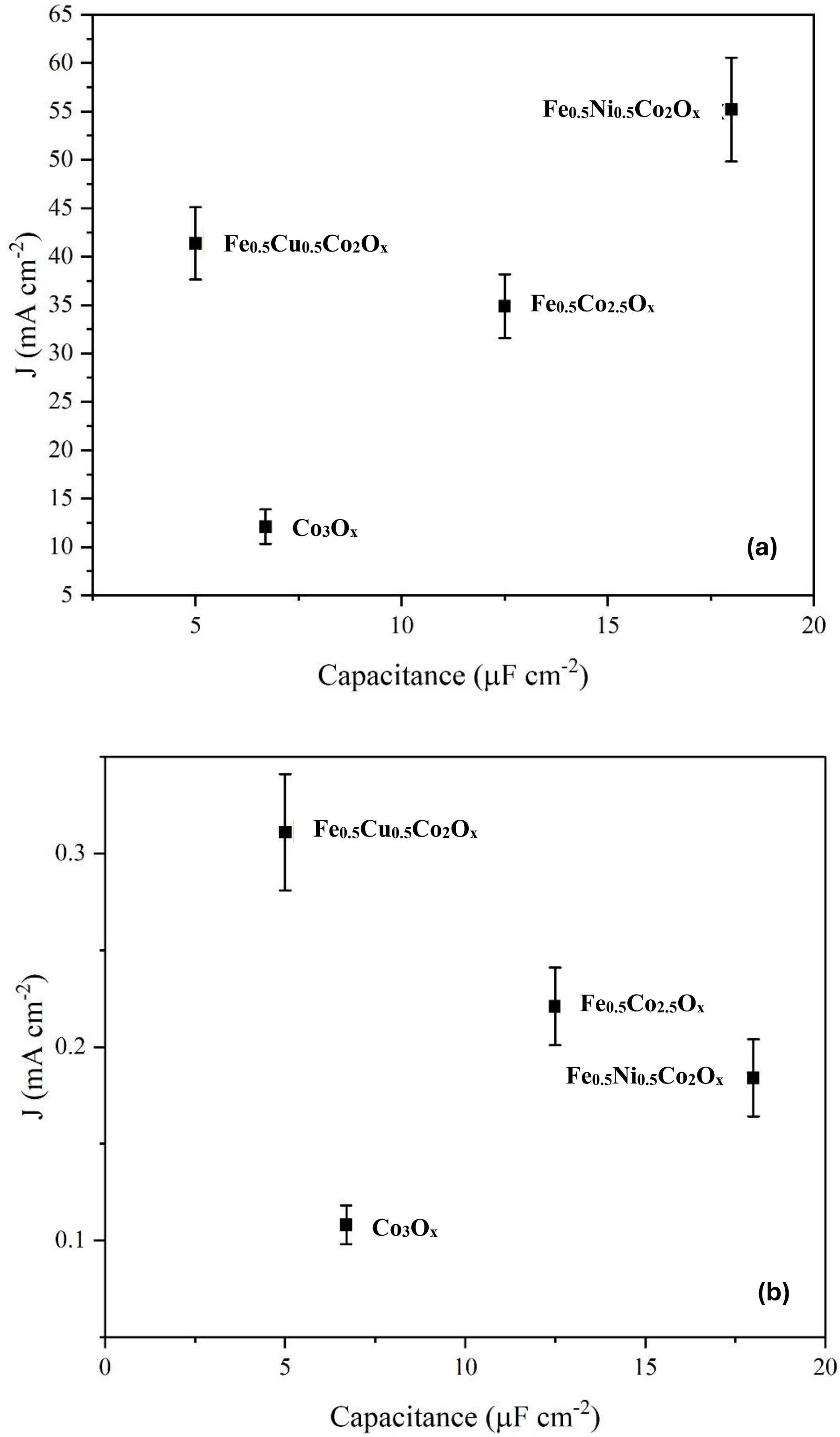

Figure 26. Graph of current density is plotted as a function of capacitance for amorphous oxides where the current density is a) corrected for only the geometric area and b) corrected for geometric area and roughness factor.

Figure 27 demonstrates a different correlations (r^2_{adj} of 0.35) between capacitance of the double layer and current density for spinel oxides electrodes. In this figure, the current is reported for 1V vs. SCE and CVs were measured in 1 M KOH electrolyte. The current is then corrected for the geometric area and roughness factor. Before correcting for surface area differences between the sample, there was no correlation between capacitance and current density. This points to amorphous oxides activity being related mainly to their surface area (extrinsic catalytic activity), while the catalytic activity depends on the intrinsic properties of the samples in the case of the spinel oxides, such as elemental composition. In accordance with the literature adding and increasing the amount of iron enhances the catalytic activity of cobalt-based spinel oxides. More on the effect of iron has been discussed in CH. 2 of this thesis. Substituting nickel also has a significant effect on the catalytic activity. For electrodes prepared in this work, when copper is added to the binary of Fe and Co ($Fe_{0.5}Cu_{0.5}Co_2O_4$), the current density almost stays the same and the capacitance dose not change significantly. However, if Ni substitutes Cu in this ternary, the current density decreases drastically, while an increase in capacitance is observed. In literature, Ni has been reported as to have a mixed effect on catalytic activity of spinel oxides. It can improve the conductivity but reduce the catalytic activity because of a decrease in electron transport. This has been reported in a study that demonstrated nickel substitution in cobalt-based spinel oxides improves a spin state transition in Co ions[53]. On the contrary, a study on cobalt nickel mixed oxide catalysts for methane combustion has reported that with an increasing Ni content, a decrease in activity was observed and they suggest an optimal Co/Ni ration can lead to maximum performance[54].

Similarly, no significant correlation has been observed in the plot of Tafel slope versus current density where the current has been corrected for the real surface area. According to the graph in figure 28, the binary of $Fe_{0.5}Co_{2.5}O_4$ and the ternary of $Fe_{0.5}Cu_{0.5}Co_2O_4$ posses the highest current density and lowest Tafel slope. A high current density means that the catalyst is able to facilitate a greater rate of the OER and a low Tafel slope can indicate that the catalyst has favorable reaction kinetics[55].

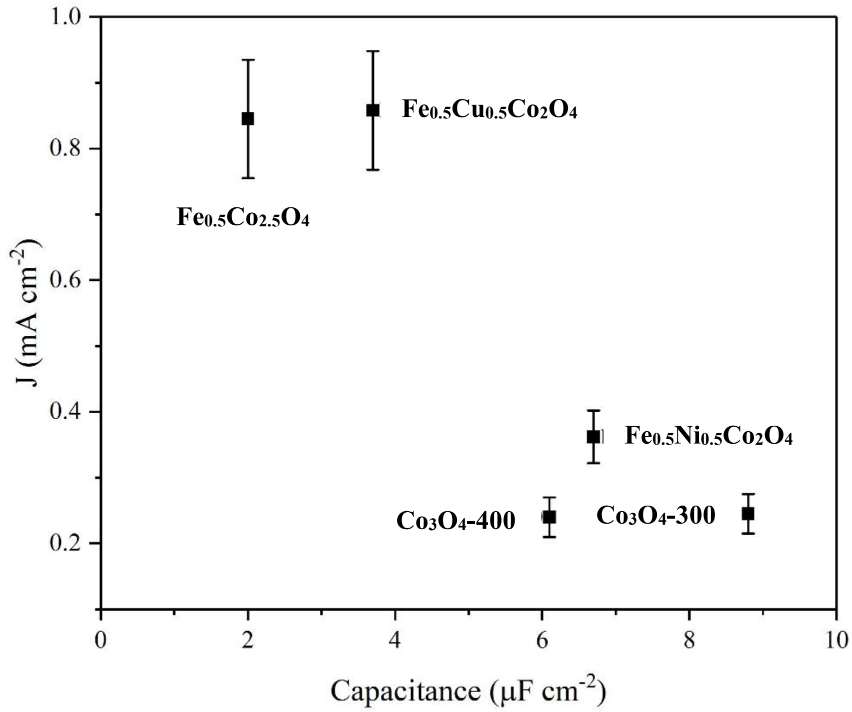

Figure 27. Graph of current density is plotted as a function of capacitance for spinel oxides where the current density is corrected for the real surface area.

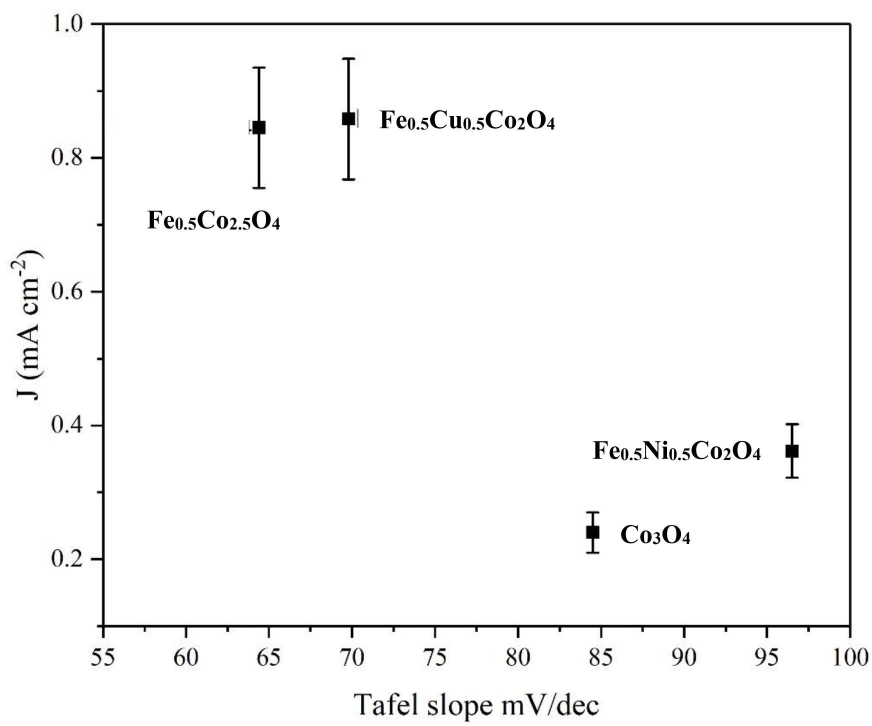

Figure 28. Graph of current density is plotted as a function of Tafel slope for spinel oxides where the current density is corrected for the real surface area.

In this chapter we linked the chemical properties and structural parameters to electrochemical properties with respect to the OER. It contains results and discussion of materials physical and chemical characterization in the first part of this chapter which includes SEM, EDX, XRD, XPS, and TEM. The second part of this chapter, materials electrochemical characterization which includes results and discussion on the capacitance obtained from CV, EIS, and differential capacitance measurements. The last part of chapter 4, electrocatalytic properties include results and discussion on CV, LSV, and Tafel slope measurements. This section also talks about various correlation between structural, electrochemical, and catalytic properties found for our electrodes. In the following chapter, we will draw conclusion and comparison with the previous works done in Dr. Morin's group. A future path for these electrodes is also drawn to take advantage of the work done here and follow along to get closer to the ultimate goal of designing an efficient electrocatalyst for OER.

4.4 References

(1) Singh, C.; Mukhopadhyay, S.; Hod, I. Metal–Organic Framework Derived Nanomaterials for Electrocatalysis: Recent Developments for CO2 and N2 Reduction. *Nano Converg* **2021**, *8* (1), 1–10. https://doi.org/10.1186/s40580-020-00251-6.

(2) Vajda, E. G.; Skedros, J. G.; Bloebaum, R. D. Errors in Quantitative Backscattered Electron Analysis of Bone Standardized by Energy-Dispersive X-Ray Spectrometry. *Scanning* **1998**, *20*, 527–535.

(3) Leng, Y. *Materials Characterization: Introduction to Microscopic and Spectroscopic Methods: 2nd Ed*; Wiley, 2013. https://doi.org/10.1002/9783527670772.

(4) Goldstein, J. I.; Newbury, D. E.; Michael, J. R.; Ritchie, N. W. M.; Scott, J. H. J.; Joy, D. C. *Scanning Electron Microscopy and X-Ray Microanalysis*, Latest edition.; Springer New York, 2018. https://doi.org/10.1007/978-1-4939-6676-9/COVER.

(5) Bunaciu, A. A.; Udriştioiu, E. gabriela; Aboul-Enein, H. Y. X-Ray Diffraction: Instrumentation and Applications. *Crit Rev Anal Chem* **2015**, *45* (4), 289–299. https://doi.org/10.1080/10408347.2014.949616.

(6) Mustapha, S.; Ndamitso, M. M.; Abdulkareem, A. S.; Tijani, J. O.; Shuaib, D. T.; Mohammed, A. K.; Sumaila, A. Comparative Study of Crystallite Size Using Williamson-Hall and Debye-Scherrer Plots for ZnO Nanoparticles. *Advances in Natural Sciences: Nanoscience and Nanotechnology* **2019**, *10*, 045013. https://doi.org/10.1088/2043-6254/ab52f7.

(7) Siegbahn, K. Electron Spectroscopy for Atoms, Molecules and Condensed Matter - an Overview. *Rev Mod Phys* **1982**, *54* (3), 709–727. https://doi.org/10.1016/0368-2048(85)80013-X.

(8) Biesinger, M. C.; Payne, B. P.; Grosvenor, A. P.; Lau, L. W.; Gerson, A. R.; StC Smart, R. Resolving Surface Chemical States in XPS Analysis of First Row Transition Metals, Oxides and Hydroxides: Cr, Mn, Fe, Co and Ni. *Appl Surf Sci* **2010**, *257*, 2717–2730. https://doi.org/10.1016/j.apsusc.2010.10.051.

(9) Mountapmbeme Kouotou, P.; Vieker, H.; Tian, Z. Y.; Tchoua Ngamou, P. H.; El Kasmi, A.; Beyer, A.; Gölzhäuser, A.; Kohse-Höinghaus, K. Structure–Activity Relation of Spinel-Type Co–Fe Oxides for Low-Temperature CO Oxidation. *Catal Sci Technol* **2014**, *4* (9), 3359–3367. https://doi.org/10.1039/C4CY00463A.

(10) Bogdandy, L. von; Engell, H. J. *The Reduction of Iron Ores*; Wiley, 1971. https://doi.org/10.1002/BBPC.19720761219.

(11) Yamashita, T.; Hayes, P. Analysis of XPS Spectra of Fe 2+ and Fe 3+ Ions in Oxide Materials. *Appl Surf Sci* **2008**, *254* (8), 2441–2449. https://doi.org/10.1016/j.apsusc.2007.09.063.

(12) Mekki, A.; Holland, D.; McConville, C. F.; Salim, M. An XPS Study of Iron Sodium Silicate Glass Surface. *J Non Cryst Solids* **1996**, *208*, 267–276.

(13) Graat, P.; Somers¤, M. A. J. Quantitative Analysis of Overlapping XPS Peaks by Spectrum Reconstruction: Determination of the Thickness and Composition of Thin Iron Oxide Films. *Surf. Interface Anal* **1998**, *26*, 773–782.

(14) Tougaard, S. Universality Classes of Inelastic Electron Scattering Cross-Sections. *Surface and Interface Analysis* **1997**, *25* (3), 137–154. https://doi.org/10.1002/(SICI)1096-9918(199703)25:3<137::AID-SIA230>3.0.CO;2-L.

(15) Castle, J. E.; Salvi, A. M. Interpretation of the Shirley Background in X-Ray Photoelectron Spectroscopy Analysis. *Journal of Vacuum Science & Technology A: Vacuum, Surfaces, and Films* **2001**, *19* (4), 1170–1175. https://doi.org/10.1116/1.1378074.

(16) Engelhard, M. H.; Baer, D. R.; Herrera-Gomez, A.; Sherwood, P. M. A. Introductory Guide to Backgrounds in XPS Spectra and Their Impact on Determining Peak Intensities. *Journal of Vacuum Science & Technology A: Vacuum, Surfaces, and Films* **2020**, *38* (6), 63203. https://doi.org/10.1116/6.0000359.

(17) Tougaard, S. Practical Guide to the Use of Backgrounds in Quantitative XPS. *Journal of Vacuum Science & Technology A* **2021**, *39* (1), 11201. https://doi.org/10.1116/6.0000661.

(18) Nixon, W. C. The General Principles of Scanning Electron Microscopy. *Philosophical Transactions of the Royal Society of London. B, Biological Sciences* **1971**, *261* (837), 45–50. https://doi.org/10.1098/rstb.1971.0035.

(19) Marsan, B.; Fradette, N.; Beaudoin, G. Physicochemical and Electrochemical Properties of CuCo2 O 4 Electrodes Prepared by Thermal Decomposition for Oxygen Evolution. *J Electrochem Soc* **1992**, *139* (7), 1889–1896. https://doi.org/10.1149/1.2069516/XML.

(20) Thekkoot, S.; Islam, R.; Morin, S. Improved Oxygen Evolution Reaction Performance with Addition of Fe to Form FeyCux-YCo3-XO4 and FeyNix-YCo3-XO4 (x = 0.5, 1 and y = 0.1, 0.15) Spinel Oxides. *Electrochim Acta* **2021**, *378*, 14–16. https://doi.org/10.1016/j.electacta.2021.138116.

(21) Liu, W. J.; Chang, Y. H.; Chiang, C. C.; Chen, Y. T.; Lu, P. X.; He, Y. J.; Lin, S. H. Studying the Effects of Annealing and Surface Roughness on Both the Magnetic Property and Surface Energy of Co60Fe20Sm20 Thin Films on Si(100) Substrate. *Coatings* **2023**, *13* (10). https://doi.org/10.3390/coatings13101783.

(22) Pan, L.; Wang, Q.; Li, Y.; Zhang, C. Amorphous Cobalt-Cerium Binary Metal Oxides as High Performance Electrocatalyst for Oxygen Evolution Reaction. *J Catal* **2020**, *384*, 14–21. https://doi.org/10.1016/j.jcat.2020.02.005.

(23) Bredar, A. R. C.; Chown, A. L.; Burton, A. R.; Farnum, B. H. Electrochemical Impedance Spectroscopy of Metal Oxide Electrodes for Energy Applications. *ACS Appl Energy Mater* **2020**, *3*, 66–98. https://doi.org/10.1021/acsaem.9b01965.

(24) Qiao, J.; Song, F.; Hu, J.; Huo, D.; Yuan, J. Mesoporous Spinel NiFe Oxide Cubes as Advanced Electrocatalysts for Oxygen Evolution. *Int J Hydrogen Energy* **2019**, *44* (31), 16368–16377. https://doi.org/10.1016/j.ijhydene.2019.04.259.

(25) Laouini, E.; Hamdani, M.; Pereira, M. I. S.; Douch, J.; Mendonc, M. H.; Berghoute, Y.; Singh, R. N. Electrochemical Impedance Spectroscopy Investigation of Spinel Type Cobalt Oxide Thin Film Electrodes in Alkaline Medium. *J Appl Electrochem* **2008**, *38*, 1485–1494. https://doi.org/10.1007/s10800-008-9593-4.

(26) Bockris, J. O.; Otagawa, T. The Electrocatalysis of Oxygen Evolution on Perovskites. *J Electrochem Soc* **1984**, *131* (2), 290–302. https://doi.org/10.1149/1.2115565.

(27) Li, H. B.; Yu, M. H.; Wang, F. X.; Liu, P.; Liang, Y.; Xiao, J.; Wang, C. X.; Tong, Y. X.; Yang, G. W. Amorphous Nickel Hydroxide Nanospheres with Ultrahigh Capacitance and Energy Density as Electrochemical Pseudocapacitor Materials. *Nature Communications 2013 4:1* **2013**, *4* (1), 1–7. https://doi.org/10.1038/ncomms2932.

(28) Cai, W.; Chen, R.; Yang, H.; Tao, H. B.; Wang, H. Y.; Gao, J.; Liu, W.; Liu, S.; Hung, S. F.; Liu, B. Amorphous versus Crystalline in Water Oxidation Catalysis: A Case Study of NiFe Alloy. *Nano Lett* **2020**, *20* (6), 4278–4285. https://doi.org/10.1021/ACS.NANOLETT.0C00840/ASSET/IMAGES/MEDIUM/NL0C00840_M003.GIF.

(29) Jeanmairet, G.; Rotenberg, B.; Salanne, M. Microscopic Simulations of Electrochemical Double-Layer Capacitors. *Chem Rev* **2022**, *122* (12), 10860–10898. https://doi.org/10.1021/ACS.CHEMREV.1C00925.

(30) Ji, H.; Zhao, X.; Qiao, Z.; Jung, J.; Zhu, Y.; Lu, Y.; Zhang, L. L.; MacDonald, A. H.; Ruoff, R. S. Capacitance of Carbon-Based Electrical Double-Layer Capacitors. *Nature Communications 2014 5:1* **2014**, *5* (1), 1–7. https://doi.org/10.1038/ncomms4317.

(31) Panchu, S. J.; Raju, K.; Swart, H. C. Emerging Two–Dimensional Intercalation Pseudocapacitive Electrodes for Supercapacitors. *ChemElectroChem* **2024**, *11* (15), e202300810. https://doi.org/10.1002/celc.202300810.

(32) Gharbi, O.; Tran, M. T. T.; Tribollet, B.; Turmine, M.; Vivier, V.; Revisiting, V. V. Revisiting Cyclic Voltammetry and Electrochemical Impedance Spectroscopy Analysis for Capacitance Measurements. *Electrochim Acta* **2020**, *343*. https://doi.org/10.1016/j.electacta.2020.136109ï.

(33) Zhu, S.; Wang, X.; Le, J.; An, N.; Li, J.; Liu, D.; Kuang, Y. Striking Stabilization Effect of Spinel Cobalt Oxide Oxygen Evolution Electrocatalysts in Neutral PH by Dual-Sites Iron Incorporation. *Energy and Environmental Materials* **2024**, *7* (2), 1–9. https://doi.org/10.1002/eem2.12594.

(34) Du, Y.; Yang, F.; Jiang, M.; Li, J.; Zhang, J. Preparation and Electrocatalytic Properties of Spinel Oxide FeCo2O4. *Proceedings of SPIE* **2022**, *12164*, 71. https://doi.org/10.1117/12.2628639.

(35) Wang, M.; Feng, X.; Li, S.; Ma, Y.; Peng, Y.; Yang, S.; Liu, Y. Spinel-Type Metal Oxides with Tailored Amorphous / Crystalline Heterointerfaces for Enhanced Electrocatalytic Water Splitting. *Adv Func Mater* **2024**, *34*, 2410439. https://doi.org/10.1002/adfm.202410439.

(36) Xiang, W.; Yang, N.; Li, X.; Linnemann, J.; Hagemann, U.; Ruediger, O.; Heidelmann, M.; Falk, T.; Aramini, M.; DeBeer, S.; Muhler, M.; Tschulik, K.; Li, T. 3D Atomic-Scale Imaging of Mixed Co-Fe Spinel Oxide Nanoparticles during Oxygen Evolution Reaction. *Nat Commun* **2022**, *13* (1), 1–14. https://doi.org/10.1038/s41467-021-27788-2.

(37) Anantharaj, S.; Noda, S. IR Drop Correction in Electrocatalysis: Everything One Needs to Know! *J Mater Chem A Mater* **2022**, *10* (17), 9348–9354. https://doi.org/10.1039/D2TA01393B.

(38) Markoví, N. M.; Ross, P. N. Surface Science Studies of Model Fuel Cell Electrocatalysts. *Surf Sci Rep* **2002**, *45* (4–6), 117–229. https://doi.org/10.1016/s0167-5729(01)00022-x.

(39) Zheng, W. IR Compensation for Electrocatalysis Studies : Considerations and Recommendations. *ACS Energy Lett* **2023**, *8*, 1952–1958. https://doi.org/10.1021/acsenergylett.3c00366.

(40) Li, H.; Kang, W.; Wang, L.; Yue, Q.; Xu, S.; Wang, H.; Liu, J. Synthesis of Three-Dimensional Flowerlike Nitrogen-Doped Carbons by a Copyrolysis Route and the Effect of Nitrogen Species on the Electrocatalytic Activity in Oxygen Reduction Reaction. *Carbon N Y* **2013**, *54*, 249–257. https://doi.org/10.1016/j.carbon.2012.11.036.

(41) Thekkoot, S.; Islam, R.; Gray, O.; Morin, S. Efficiency of Nanostructured CuxCo3-XO4 and NixCu1 – XCo2O4 Electrodes as Electrocatalysts for the Oxygen Evolution Reaction-Revisited. *Electrochim Acta* **2023**, *471*, 143339. https://doi.org/10.7868/s0002337x15010042.

(42) Malima, N. M.; Khan, M. D.; Choi, J.; Gupta, R. K.; Mashazi, P.; Nyokong, T.; Revaprasadu, N. Solventless Synthesis of Nanospinel Ni1−xCoxFe2O4(0 ≤x≤ 1) Solid Solutions for Efficient Electrochemical Water Splitting and Supercapacitance. *RSC Adv* **2021**, *11* (49), 31002–31014. https://doi.org/10.1039/d1ra04833c.

(43) Yousaf, S.; Zulfiqar, S.; Khalid, M. U.; Warsi, M. F.; Shakir, I.; Shahid, M.; Ahmad, I.; Cochran, E. W. Beyond the Ordinary: Exploring the Synergistic Effect of Iodine and Nickel Doping in Cobalt Hydroxide for Superior Energy Storage Applications. *RSC Adv* **2024**, *14* (24), 16661. https://doi.org/10.1039/D4RA01907E.

(44) Saddeler, S.; Bendt, G.; Salamon, S.; Haase, F. T.; Landers, J.; Timoshenko, J.; Rettenmaier, C.; Jeon, H. S.; Bergmann, A.; Wende, H.; Roldan Cuenya, B.; Schulz, S. Influence of the Cobalt Content in Cobalt Iron Oxides on the Electrocatalytic OER Activity. *J Mater Chem A Mater* **2021**, *9* (45), 25381–25390. https://doi.org/10.1039/d1ta06568h.

(45) He, C.; Han, X.; Kong, X.; Jiang, M.; Lei, D.; Lei, X. Fe-Doped Co 3 O 4 @C Nanoparticles Derived from Layered Double Hydroxide Used as Efficient Electrocatalyst for Oxygen Evolution Reaction. *Journal of Energy Chemistry* **2019**, *32*, 63–70. https://doi.org/10.1016/j.jechem.2018.06.014.

(46) Thekkoot, S. *Crystalline and Amorphous Cobalt-Based Metal Oxides for Water Oxidation Reaction – Structure, Composition, Morphology and Electrochemical Performance*; Ph.D. Thesis, York University, Toronto, 2024.

(47) Kumar, D.; Singh, M.; Singh, A. K. Crystallite Size Effect on Lattice Strain and Crystal Structure of Ba1/4Sr3/4MnO3 Layered Perovskite Manganite. *AIP Conf Proc* **2018**, *1953*, 10–13. https://doi.org/10.1063/1.5032520.

(48) Hossain, S.; Dev, G.; Aktar, Mst. S.; Kamrul Hassan, M.; Zakaria, A. K. M.; Kumar Datta, T.; Kamal, I.; Yunus, Sk. M.; Habibul Ahsan, M.; Azad, A. K. Preparation and Structural Properties of ZnAlxFe2−xO4 Spinel Oxide. *Am J Analyt Chem* **2016**, *7*, 203–209. https://doi.org/10.1016/j.physb.2010.08.050.

(49) Jian, W.; Jia, R.; Wang, J.; Zhang, H. X.; Bai, F. Q. Iron Oxides with a Reverse Spinel Structure: Impact of Active Sites on Molecule Adsorption. *Inorg Chem Front* **2019**, *6* (10), 2810–2816. https://doi.org/10.1039/c9qi00790c.

(50) Tok, A. I. Y.; Du, S. W.; Boey, F. Y. C.; Chong, W. K. Hydrothermal Synthesis and Characterization of Rare Earth Doped Ceria Nanoparticles. *Materials Science and Engineering A* **2007**, *466*, 223–229. https://doi.org/10.1016/j.msea.2007.02.083.

(51) Li, H. B.; Yu, M. H.; Wang, F. X.; Liu, P.; Liang, Y.; Xiao, J.; Wang, C. X.; Tong, Y. X.; Yang, G. W. Amorphous Nickel Hydroxide Nanospheres with Ultrahigh Capacitance and Energy Density as Electrochemical Pseudocapacitor Materials. *Nat Commun* **2013**, *4*. https://doi.org/10.1038/ncomms2932.

(52) Rezaee, B.; Thekkoot, S. R.; Gray, O.; Rajaguru, D.; Tian, J.; Morin, S. Systematic Study of the Effect of Iron in Mixed Transition Metal Spinel Oxides as Oxygen Evolution Electrocatalysts – Electrochemistry and Materials Properties. *In Preparation*.

(53) Liu, S.; Zhang, B.; Cao, Y.; Wang, H.; Zhang, Y.; Zhang, S.; Li, Y.; Gong, H.; Liu, S.; Yang, Z.; Sun, J. Understanding the Effect of Nickel Doping in Cobalt Spinel Oxides on Regulating Spin State to Promote the Performance of the Oxygen Reduction Reaction and Zinc-Air Batteries. *ACS Energy Lett* **2023**, *8* (1), 159–168. https://doi.org/10.1021/acsenergylett.2c02457.

(54) Lim, T. H.; Cho, S. J.; Yang, H. S.; Engelhard, M. H.; Kim, D. H. Effect of Co/Ni Ratios in Cobalt Nickel Mixed Oxide Catalysts on Methane Combustion. *Appl Catal A Gen* **2015**, *505*, 62–69. https://doi.org/10.1016/j.apcata.2015.07.040.

(55) Raveendran, A.; Chandran, M.; Dhanusuraman, R. A Comprehensive Review on the Electrochemical Parameters and Recent Material Development of Electrochemical Water Splitting Electrocatalysts. *RSC Adv* **2023**, *13* (6), 3843–3876. https://doi.org/10.1039/d2ra07642j.

Chapter 5: Conclusions and future directions

5.1 Conclusion

The over usage of fossil fuels has made a significant contribution to global warming and air pollution, giving rise to profound environmental and health consequences. Hydrogen gas is considered as a renewable energy carrier and clean fuel since its main byproduct is water when oxidized in fuel cells. However, a notable challenge in this process lies in bypassing the significant overpotential associated with the OER. Therefore, developing a better catalyst for OER is of high importance to be able to activate the rate limiting step and to reduce the overpotential. Our main goal was to investigate the relationship between the structure and composition of the transition metal oxide materials (iron rich cobalt spinel oxides in the crystalline and amorphous forms) to their electrocatalytic performance for OER.

To accomplish this goal, various novel binary and ternary compositions of amorphous and spinel cobalt-rich oxides were prepared ($Cu_{0.5}Fe_{0.5}Co_2O_4$, $Ni_{0.5}Fe_{0.5}Co_2O_4$, $Fe_{0.5}Co_{2.5}O_4$, $Cu_{0.5}Fe_{0.5}Co_2O_x$, $Fe_{0.5}Co_{2.5}O_x$, $Cu_{0.5}Fe_{0.5}Co_2O_x$) and characterized by XRD, EDXS, TEM, XPS, and SEM to confirm their amorphous/crystalline nature, their stochiometric compositions and to determine the surface morphology for these metal oxides. Moreover, to investigate their catalytic properties cyclic voltammetry, EIS, Tafel slope analysis, and differential capacitance measurements were conducted. The results of surface characterization and electrochemical performances of the amorphous cobalt oxides were compared to the results obtained for spinel materials of the same composition.

Most of the binary and ternary cobalt oxides that were synthesized and characterized through this work, have not/or rarely been studied and reported in literature. This work contains the successful synthesis procedure for both amorphous and crystalline (spinel) transition metal oxides. Their morphology has been successfully confirmed by SEM and TEM. Moreover, the elemental composition obtained from EDX show that their stoichiometric compositions are in good agreement with their bulk compositions. XRD results revealed information regarding crystallite size, lattice parameters, and the main structure of the materials. Two spinel compositions have been placed under detailed surface analysis using XPS and the results revealed that there are more structures present at the surface (such as hydroxides, oxides, and hydroxy oxides) even though XRD only confirmed one spinel structure.

In order to study different composition and compare their electrocatalytic performance, the current density has to be normalized for the real surface area of the sample. This will enable us to make comparisons and determine the superior composition as electrocatalyst for OER. In this work we performed the normalization by measuring the surface area through CV and determining the roughness factor.

Looking at roughness factor data obtained from capacitance measurements and the SEM images for amorphous oxides; an apparent discrepancy is observed. This could be explained by the difference in the scale at which each method works. Capacitance measurements are sensitive to very small features, just a few angstroms across. While SEM images capture features that are thousands of times larger, on the micrometer scale. This means that a surface can appear rough when measured at the atomic level but still look smooth when viewed at a much larger scale. So, the two results are not actually in conflict. They are just showing different details of the same surface.

The electrocatalytic performances of these catalysts were evaluated by cyclic voltammetry. Iron rich cobalt oxides showed high current density in compared to pure cobalt oxides. This reveals the role of iron in improving the catalytic activity. Another important information obtained from CVs, is that among the iron rich samples substituting Cu with Ni has a detrimental effect on the catalytic activity. These results are in line with our previous study in Morin's group[1,2].

To obtain information regarding the double layer capacitance and the total capacitance of the electrode, EIS and differential capacitance measurements were also conducted. One key observation from these results was that the capacitance obtained from EIS (for spinel oxides) is very close to the one calculated using CV, which further implies the validity of our method in surface area measurements and current density normalization.

Another key finding of this study includes some correlations between different structural, chemicals, and electrochemical parameters of our sample. These relationships can help in evaluating and mapping materials properties according to their structure and chemical composition. Data obtained from XRD revealed that there is an inverse relationship between the crystallite size and the lattice parameter for spinel oxides. The substitution of Co with Fe had led to an increase in the lattice parameter due to the larger ionic radii of the cations. Moreover, an increased iron content has led to a disruption in crystal growth and therefore formation of finer crystallites in spinel oxides. An inverse relationship was also observed for the current density and lattice parameters.

The correlation between the current density and the double layer capacitance of the amorphous oxide has also led to an important finding. The obtained results suggest that the current density and in turn the catalytic performance of the amorphous oxides is merely due to the surface area of the sample instead of its intrinsic activity. Furthermore, the obtained results from spinel oxides do not show this relationship which indicates the catalytic performance of the spinels are more complex and depend on various factors such as structure and composition of the sample. This correlation has been reported in literature[3], and it is in line with previous works in Prof. Morin's group where a series of various amorphous and spinel oxides were compared for their electrocatalytic properties[2].

As part of the studies for electrocatalytic properties, Tafel slope measurements where also conducted using rotating disc electrode. Tafel slopes of iron rich cobalt oxide was the lowest and closely followed by the copper incorporated iron cobalt oxide. However, Ni has a deteriorating effect on the catalytic activity since by incorporating Ni, the Tafel slope increased. This trend is also supported by CV data where iron rich cobalt oxide and copper incorporated iron cobalt oxide posses the highest current density and the Ni incorporated oxide sit way below on the graph.

The goal of this work was to study the effect of adding and increasing the amount of iron incorporation into pure cobalt oxides electrodes and through synthesizing novel amorphous and crystalline (spinel) compositions and investigate their properties using various structural, chemical, and electrochemical techniques. The results will provide great data and in conjugation with our previous work in Morin's group, can be highly beneficial towards building a set of guidelines for designing an efficient electrocatalyst from transition metal oxides for OER. Enhancing OER catalysts can help to increase hydrogen production which is crucial for clean energy applications and removing the dependency to fossil fuels.

5.2 Future work

Future works for this research could include more advanced characterization techniques such as in-situ XPS, XRD and Raman spectroscopy to monitor real time changes at the surface and in bulk of the electrode during OER and to obtain insights into the active species formation. XAS also can be useful as it can probe the oxidation state and identify the local coordination environments around the atoms in various structures[4]. Moreover, computational and theoretical studies such as density functional theory (DFT) calculation can provide information regarding the reaction pathway and binding energies of the intermediate species[5].

Another future path for this work can be studying a series of electrode containing both amorphous and spinel at the surface. As it has been reported in many literatures that a combination of amorphous and spinel phases at the surface of the electrode can posses high electrocatalytic properties. DFT calculations can help to understand the electronic structure in mixed-phase catalysts and can guide in phase engineering strategies[5].

Furthermore, as it was shown in this work and in our previous works in Morin's group that adding and increasing the amount of iron has an enhancing effect on the electrocatalytic activity of the cobalt oxides, more characterization techniques that help in unravelling the role of iron should be employed. Mossbauer spectroscopy can help in probing the magnetic properties of iron and its electronic contribution towards OER through determining the ratio of F^{2+}/Fe^{3+} cations, their coordination geometry of octahedral vs. tetrahedral, and its interaction with the surrounding atoms[6]. Electron paramagnetic resonance spectroscopy (EPR) also can be used to obtain information regarding unpaired electrons and defect site. These techniques will help in determining if the lattice iron improves the catalytic activity via electronic effects or through forming defects on the lattice structure[7].

5.3 References

(1) Thekkoot, S.; Islam, R.; Morin, S. Improved Oxygen Evolution Reaction Performance with Addition of Fe to Form FeyCux-YCo3-XO4 and FeyNix-YCo3-XO4 (x = 0.5, 1 and y = 0.1, 0.15) Spinel Oxides. *Electrochim Acta* **2021**, *378*, 14–16. https://doi.org/10.1016/j.electacta.2021.138116.

(2) Thekkoot, S. *Crystalline and Amorphous Cobalt-Based Metal Oxides for Water Oxidation Reaction – Structure, Composition, Morphology and Electrochemical Performance*; Ph.D. Thesis, York University, Toronto, **2024**.

(3) Li, H. B.; Yu, M. H.; Wang, F. X.; Liu, P.; Liang, Y.; Xiao, J.; Wang, C. X.; Tong, Y. X.; Yang, G. W. Amorphous Nickel Hydroxide Nanospheres with Ultrahigh Capacitance and Energy Density as Electrochemical Pseudocapacitor Materials. *Nat Commun* **2013**, *4*. https://doi.org/10.1038/ncomms2932.

(4) Yano, J.; Yachandra, V. K. X-Ray Absorption Spectroscopy. *Photosynthesis Research* **2009**, *102*, 241–254. https://doi.org/10.1007/s11120-009-9473-8.

(5) Pantazis, D. A.; Orio, M.; Neese, F. Density Functional Theory. *Photosynthesis Research* **2009**, *102*, 443–453. https://doi.org/10.1007/s11120-009-9404-8.

(6) Yoshida, Y.; Langouche, G. *Mössbauer Spectroscopy*; Springer-Verlag Berlin Heidelberg, **2013**.

(7) Bonke, S. A.; Risse, T.; Schnegg, A.; Bruckner, A. In Situ Electron Paramagnetic Resonance Spectroscopy for Catalysis. *Nature reviews: methods and primers* **2021**, *1* (1).

List of References Cited in Thesis

1. aoki, K.; Tokuda, K.; Matsuda, H. Linear Sweep and Cyclic Voltammetry for Electrocatalysis at Modified Electrodes with Very Thin Films. *J Electroanal Chem Interfacial Electrochem* **1986**, *199* (1), 69–79. https://doi.org/10.1016/0022-0728(86)87042-5.

2. A. Mohammed; A. Abdullah. Scanning Electron Microscopy (SEM): A Review. *Proceedings of 2018 International Conference on Hydraulics and Pneumatics - HERVEX* **2018**, 77–85.

3. Allen, L. J.; D'Alfonso, A. J.; Freitag, B.; Klenov, D. O. Chemical Mapping at Atomic Resolution Using Energy-Dispersive X-Ray Spectroscopy. *MRS Bull* **2012**, *37* (1), 47–52. https://doi.org/10.1557/mrs.2011.331.

4. Anantharaj, S.; Noda, S. How Properly Are We Interpreting the Tafel Lines in Energy Conversion Electrocatalysis? *Mater Today Energy* **2022**, *29*, 101123. https://doi.org/10.1016/j.mtener.2022.101123.

5. Anantharaj, S.; Noda, S. IR Drop Correction in Electrocatalysis: Everything One Needs to Know! *J Mater Chem A Mater* **2022**, *10* (17), 9348–9354. https://doi.org/10.1039/D2TA01393B.

6. Bai, L.; Wen, X.; Guan, J. Amorphous Fe[Sbnd]Co[Sbnd]Ni Oxide for Oxygen Evolution Reaction. *Mater Today Energy* **2019**, *12*, 311–317. https://doi.org/10.1016/j.mtener.2019.02.004.

7. Bard, A. J.; Faulkner, L. R. *Electrochemical Methods: Fundamentals and Applications*, 2nd ed.; Wiley: New York, 2001.

8. Bergmann, A.; Martinez-Moreno, E.; Teschner, D.; Chernev, P.; Gliech, M.; De Araújo, J. F.; Reier, T.; Dau, H.; Strasser, P. Reversible Amorphization and the Catalytically Active State of Crystalline Co3O4 during Oxygen Evolution. *Nat Commun* **2015**, *6*, 8625. https://doi.org/10.1038/ncomms9625.

9. Biesinger, M. C.; Payne, B. P.; Grosvenor, A. P.; Lau, L. W.; Gerson, A. R.; StC Smart, R. Resolving Surface Chemical States in XPS Analysis of First Row Transition Metals, Oxides and Hydroxides: Cr, Mn, Fe, Co and Ni. *Appl Surf Sci* **2010**, *257*, 2717–2730. https://doi.org/10.1016/j.apsusc.2010.10.051.

10. Binnig, G.; Quate' ', C. F.; Gi, E. L.; Gerber, C. Atomic Force Microscope. *Phys Rev Lett* **1986**, *56* (9), 930–933.

11. Bockris, J. O.; Otagawa, T. The Electrocatalysis of Oxygen Evolution on Perovskites. *J Electrochem Soc* **1984**, *131* (2), 290–302. https://doi.org/10.1149/1.2115565.

12. Bogdandy, L. von; Engell, H. J. *The Reduction of Iron Ores*; Wiley, 1971. https://doi.org/10.1002/BBPC.19720761219.

13. Bonke, S. A.; Risse, T.; Schnegg, A.; Bruckner, A. In Situ Electron Paramagnetic Resonance Spectroscopy for Catalysis. *Nature reviews: methods and primers* **2021**, *1* (1).

14. Bredar, A. R. C.; Chown, A. L.; Burton, A. R.; Farnum, B. H. Electrochemical Impedance Spectroscopy of Metal Oxide Electrodes for Energy Applications. *ACS Appl Energy Mater* **2020**, *3*, 66–98. https://doi.org/10.1021/acsaem.9b01965.

15. Brunauer, S.; Emmett, P. H.; Teller, E. Adsorption of Gases in Multimolecular Layers. *J Am Chem Soc* **1938**, *60* (2), 309–319. https://doi.org/10.1021/JA01269A023.

16. Bunaciu, A. A.; Udriştioiu, E. gabriela; Aboul-Enein, H. Y. X-Ray Diffraction: Instrumentation and Applications. *Crit Rev Anal Chem* **2015**, *45* (4), 289–299. https://doi.org/10.1080/10408347.2014.949616.

17. Cai, W.; Chen, R.; Yang, H.; Tao, H. B.; Wang, H. Y.; Gao, J.; Liu, W.; Liu, S.; Hung, S. F.; Liu, B. Amorphous versus Crystalline in Water Oxidation Catalysis: A Case Study of NiFe Alloy. *Nano Lett* **2020**, *20* (6), 4278–4285.

18. Castle, J. E.; Salvi, A. M. Interpretation of the Shirley Background in X-Ray Photoelectron Spectroscopy Analysis. *Journal of Vacuum Science & Technology A: Vacuum, Surfaces, and Films* **2001**, *19* (4), 1170–1175. https://doi.org/10.1116/1.1378074.

19. Corrigan, D. A. Catalysis of the Oxygen Evolution Reaction by Trace Iron Impurities in Thin Film Nickel Oxide Electrodes. *J Electrochem Soc* **1987**, *134*, 377.

20. Cushman, C. V.; Chatterjee, S.; Major, G. H.; Smith, N. J.; Roberts, A.; Linford, M. R. Trends in Advanced XPS Instrumentation. I. Overview of the Technique, Automation, High Sensitivity, Imaging, Snapshot Spectroscopy, Gas Cluster Ion Beams, and Multiple Analytical Techniques on the Instrument. *Vacuum Technology & Coating* **2016**, No. 11, 2–9.

21. Du, Y.; Yang, F.; Jiang, M.; Li, J.; Zhang, J. Preparation and Electrocatalytic Properties of Spinel Oxide FeCo2O4. *Proceedings of SPIE* **2022**, *12164*, 71. https://doi.org/10.1117/12.2628639.

22. Elgrishi, N. N.; Rountree, K. J.; Mccarthy, B. D.; Rountree, E. S.; Eisenhart, T. T.; Dempsey, J. L. A Practical Beginner's Guide to Cyclic Voltammetry. **2017**. https://doi.org/10.1021/acs.jchemed.7b00361.

23. Engelhard, M. H.; Baer, D. R.; Herrera-Gomez, A.; Sherwood, P. M. A. Introductory Guide to Backgrounds in XPS Spectra and Their Impact on Determining Peak Intensities. *Journal of Vacuum Science & Technology A: Vacuum, Surfaces, and Films* **2020**, *38* (6), 63203. https://doi.org/10.1116/6.0000359.

24. Gharbi, O.; Tran, M. T. T.; Tribollet, B.; Turmine, M.; Vivier, V.; Revisiting, V. V. Revisiting Cyclic Voltammetry and Electrochemical Impedance Spectroscopy Analysis for Capacitance Measurements. *Electrochim Acta* **2020**, *343*. https://doi.org/10.1016/j.electacta.2020.136109ï.

25. Glenk, G.; Reichelstein, S. Economics of Converting Renewable Power to Hydrogen. *Nat Energy* **2019**, *4* (3), 216–222.

26. Goldstein, J. I.; Newbury, D. E.; Michael, J. R.; Ritchie, N. W. M.; Scott, J. H. J.; Joy, D. C. *Scanning Electron Microscopy and X-Ray Microanalysis*, Latest edition.; Springer New York, 2018. https://doi.org/10.1007/978-1-4939-6676-9/COVER.

27. Graat, P.; Somers¤, M. A. J. Quantitative Analysis of Overlapping XPS Peaks by Spectrum Reconstruction: Determination of the Thickness and Composition of Thin Iron Oxide Films. *Surf. Interface Anal* **1998**, *26*, 773–782.

28. He, C.; Han, X.; Kong, X.; Jiang, M.; Lei, D.; Lei, X. Fe-Doped Co 3 O 4 @C Nanoparticles Derived from Layered Double Hydroxide Used as Efficient Electrocatalyst for Oxygen Evolution Reaction. *Journal of Energy Chemistry* **2019**, *32*, 63–70. https://doi.org/10.1016/j.jechem.2018.06.014.

29. Hodoroaba, V. D.; Procop, M. A Method to Test the Performance of an Energy-Dispersive X-Ray Spectrometer (EDS). *Microscopy and Microanalysis* **2014**, *20* (5), 1556–1564. https://doi.org/10.1017/S1431927614001652.

30. Hossain, S.; Dev, G.; Aktar, Mst. S.; Kamrul Hassan, M.; Zakaria, A. K. M.; Kumar Datta, T.; Kamal, I.; Yunus, Sk. M.; Habibul Ahsan, M.; Azad, A. K. Preparation and Structural Properties of ZnAlxFe2−xO4 Spinel Oxide. *Am J Analyt Chem* **2016**, *7*, 203–209. https://doi.org/10.1016/j.physb.2010.08.050.

31. Hung, S. F.; Hsu, Y. Y.; Chang, C. J.; Hsu, C. S.; Suen, N. T.; Chan, T. S.; Chen, H. M. Unraveling Geometrical Site Confinement in Highly Efficient Iron-Doped Electrocatalysts toward Oxygen Evolution Reaction. *Adv Energy Mater* **2018**, *8* (7), 1701686. https://doi.org/10.1002/aenm.201701686.

32. Indra, A.; Menezes, P. W.; Sahraie, N. R.; Bergmann, A.; Das, C.; Tallarida, M.; Schmeißer, D.; Strasser, P.; Driess, M. Unification of Catalytic Water Oxidation and Oxygen Reduction Reactions: Amorphous Beat Crystalline Cobalt Iron Oxides. *J Am Chem Soc* **2014**, *136* (50), 17530–17536. https://doi.org/10.1021/ja509348t.

33. Intergovernmental Panel on Climate Change. *Climate Change 2021: The Physical Science Basis*. Intergovernmental Panel on Climate Change. https://doi.org/10.4324/9781315071961-11.

34. Jeanmairet, G.; Rotenberg, B.; Salanne, M. Microscopic Simulations of Electrochemical Double-Layer Capacitors. *Chem Rev* **2022**, *122* (12), 10860–10898. https://doi.org/10.1021/ACS.CHEMREV.1C00925.

35. Jerkiewicz, G. Standard and Reversible Hydrogen Electrodes: Theory, Design, Operation, and Applications. *ACS Catal* **2020**, *10* (15), 8409–8417. https://doi.org/10.1021/acscatal.0c02046.

36. Ji, H.; Zhao, X.; Qiao, Z.; Jung, J.; Zhu, Y.; Lu, Y.; Zhang, L. L.; MacDonald, A. H.; Ruoff, R. S. Capacitance of Carbon-Based Electrical Double-Layer Capacitors. *Nature Communications 2014 5:1* **2014**, *5* (1), 1–7. https://doi.org/10.1038/ncomms4317.

37. Jian, W.; Jia, R.; Wang, J.; Zhang, H. X.; Bai, F. Q. Iron Oxides with a Reverse Spinel Structure: Impact of Active Sites on Molecule Adsorption. *Inorg Chem Front* **2019**, *6* (10), 2810–2816. https://doi.org/10.1039/c9qi00790c.

38. Kapałka, A.; Fóti, G.; Comninellis, C. Determination of the Tafel Slope for Oxygen Evolution on Boron-Doped Diamond Electrodes. *Electrochem commun* **2008**, *10* (4), 607–610. https://doi.org/10.1016/j.elecom.2008.02.003.

39. Kim, J. S.; Kim, B.; Kim, H.; Kang, K. Recent Progress on Multimetal Oxide Catalysts for the Oxygen Evolution Reaction. *Advanced Energy Materials*. **2018**, *8*, 1702774. https://doi.org/10.1002/aenm.201702774.

40. Krishna, D. N. G.; Philip, J. Review on Surface-Characterization Applications of X-Ray Photoelectron Spectroscopy (XPS): Recent Developments and Challenges. *Applied Surface Science Advances* **2022**, *12* (November), 100332. https://doi.org/10.1016/j.apsadv.2022.100332.

41. Kumar, D.; Singh, M.; Singh, A. K. Crystallite Size Effect on Lattice Strain and Crystal Structure of Ba1/4Sr3/4MnO3 Layered Perovskite Manganite. *AIP Conf Proc* **2018**, *1953*, 10–13. https://doi.org/10.1063/1.5032520.

42. Lan, S.; Zhu, L.; Wu, Z.; Gu, L.; Zhang, Q.; Kong, H.; Liu, J.; Song, R.; Liu, S.; Sha, G.; Wang, Y.; Liu, Q.; Liu, W.; Wang, P.; Liu, C. T.; Ren, Y.; Wang, X. L. A Medium-Range Structure Motif Linking Amorphous and Crystalline States. *Nat Mater* **2021**, *20* (10), 1347–1352. https://doi.org/10.1038/s41563-021-01011-5.

43. Laouini, E.; Hamdani, M.; Pereira, M. I. S.; Douch, J.; Mendonc, M. H.; Berghoute, Y.; Singh, R. N. Electrochemical Impedance Spectroscopy Investigation of Spinel Type Cobalt Oxide Thin Film Electrodes in Alkaline Medium. *J Appl Electrochem* **2008**, *38*, 1485–1494. https://doi.org/10.1007/s10800-008-9593-4.

44. Lazanas, A. C.; Prodromidis, M. I. Electrochemical Impedance Spectroscopy - A Tutorial. *ACS Measurement Science Au* **2023**, *3*, 162–193. https://doi.org/10.1021/acsmeasuresciau.2c00070.

45. Leng, Y. *Materials Characterization: Introduction to Microscopic and Spectroscopic Methods: 2nd Ed*; Wiley, 2013. https://doi.org/10.1002/9783527670772.

46. Li, H. B.; Yu, M. H.; Wang, F. X.; Liu, P.; Liang, Y.; Xiao, J.; Wang, C. X.; Tong, Y. X.; Yang, G. W. Amorphous Nickel Hydroxide Nanospheres with Ultrahigh Capacitance and Energy Density as Electrochemical Pseudocapacitor Materials. *Nature Communications 2013 4:1* **2013**, *4* (1), 1–7. https://doi.org/10.1038/ncomms2932.

47. Li, H.; Kang, W.; Wang, L.; Yue, Q.; Xu, S.; Wang, H.; Liu, J. Synthesis of Three-Dimensional Flowerlike Nitrogen-Doped Carbons by a Copyrolysis Route and the Effect of Nitrogen Species on the Electrocatalytic Activity in Oxygen Reduction Reaction. *Carbon N Y* **2013**, *54*, 249–257. https://doi.org/10.1016/j.carbon.2012.11.036.

48. Lim, T. H.; Cho, S. J.; Yang, H. S.; Engelhard, M. H.; Kim, D. H. Effect of Co/Ni Ratios in Cobalt Nickel Mixed Oxide Catalysts on Methane Combustion. *Appl Catal A Gen* **2015**, *505*, 62–69. https://doi.org/10.1016/j.apcata.2015.07.040.

49. Liu, S.; Zhang, B.; Cao, Y.; Wang, H.; Zhang, Y.; Zhang, S.; Li, Y.; Gong, H.; Liu, S.; Yang, Z.; Sun, J. Understanding the Effect of Nickel Doping in Cobalt Spinel Oxides on Regulating Spin State to Promote the Performance of the Oxygen Reduction Reaction and Zinc-Air Batteries. *ACS Energy Lett* **2023**, *8* (1), 159–168. https://doi.org/10.1021/acsenergylett.2c02457.

50. Liu, W. J.; Chang, Y. H.; Chiang, C. C.; Chen, Y. T.; Lu, P. X.; He, Y. J.; Lin, S. H. Studying the Effects of Annealing and Surface Roughness on Both the Magnetic Property and Surface Energy of

Co60Fe20Sm20 Thin Films on Si(100) Substrate. *Coatings* **2023**, *13* (10). https://doi.org/10.3390/coatings13101783.

51. Lu, Y. T.; Chien, Y. J.; Liu, C. F.; You, T. H.; Hu, C. C. Active Site-Engineered Bifunctional Electrocatalysts of Ternary Spinel Oxides, M0.1Ni0.9Co2O4 (M: Mn, Fe, Cu, Zn) for the Air Electrode of Rechargeable Zinc–Air Batteries. *J Mater Chem A Mater* **2017**, *5* (39), 21016–21026. https://doi.org/10.1039/C7TA06302D.

52. Malima, N. M.; Khan, M. D.; Choi, J.; Gupta, R. K.; Mashazi, P.; Nyokong, T.; Revaprasadu, N. Solventless Synthesis of Nanospinel Ni1−xCoxFe2O4(0 ≤x≤ 1) Solid Solutions for Efficient Electrochemical Water Splitting and Supercapacitance. *RSC Adv* **2021**, *11* (49), 31002–31014. https://doi.org/10.1039/d1ra04833c.

53. Markoví, N. M.; Ross, P. N. Surface Science Studies of Model Fuel Cell Electrocatalysts. *Surf Sci Rep* **2002**, *45* (4–6), 117–229. https://doi.org/10.1016/s0167-5729(01)00022-x.

54. Marsan, B.; Fradette, N.; Beaudoin, G. Physicochemical and Electrochemical Properties of CuCo2 O 4 Electrodes Prepared by Thermal Decomposition for Oxygen Evolution. *J Electrochem Soc* **1992**, *139* (7), 1889–1896. https://doi.org/10.1149/1.2069516/XML.

55. McCrory, C. C. L.; Jung, S.; Ferrer, I. M.; Chatman, S. M.; Peters, J. C.; Jaramillo, T. F. Benchmarking Hydrogen Evolving Reaction and Oxygen Evolving Reaction Electrocatalysts for Solar Water Splitting Devices. *J Am Chem Soc* **2015**, *137* (13), 4347–4357. https://doi.org/10.1021/ja510442p.

56. McCrory, C. C. L.; Jung, S.; Peters, J. C.; Jaramillo, T. F. Benchmarking Heterogeneous Electrocatalysts for the Oxygen Evolution Reaction. *J Am Chem Soc* **2013**, *135* (45), 16977–16987. https://doi.org/10.1021/ja407115p.

57. Mekki, A.; Holland, D.; McConville, C. F.; Salim, M. An XPS Study of Iron Sodium Silicate Glass Surface. *J Non Cryst Solids* **1996**, *208*, 267–276.

58. Miti, Ž.; Stoli, A.; Stojanovi, S.; Najman, S.; Ignjatovi, N.; Nikoli, G.; Trajanovi, M. Instrumental Methods and Techniques for Structural and Physicochemical Characterization of Biomaterials and Bone Tissue : A Review. *Materials Science and Engineering C* **2017**, *79*, 930–949. https://doi.org/10.1016/j.msec.2017.05.127.

59. Mountapmbeme Kouotou, P.; Vieker, H.; Tian, Z. Y.; Tchoua Ngamou, P. H.; El Kasmi, A.; Beyer, A.; Gölzhäuser, A.; Kohse-Höinghaus, K. Structure–Activity Relation of Spinel-Type Co–Fe Oxides for Low-Temperature CO Oxidation. *Catal Sci Technol* **2014**, *4* (9), 3359–3367. https://doi.org/10.1039/C4CY00463A.

60. Mustapha, S.; Ndamitso, M. M.; Abdulkareem, A. S.; Tijani, J. O.; Shuaib, D. T.; Mohammed, A. K.; Sumaila, A. Comparative Study of Crystallite Size Using Williamson-Hall and Debye-Scherrer Plots for ZnO Nanoparticles. *Advances in Natural Sciences: Nanoscience and Nanotechnology* **2019**, *10*, 045013. https://doi.org/10.1088/2043-6254/ab52f7.

61. Nasir, S.; Hussein, M. Z.; Zainal, Z.; Yusof, N. A.; Mohd Zobir, S. A.; Alibe, I. M. Potential Valorization of By-Product Materials from Oil Palm: A Review of Alternative and Sustainable Carbon Sources for Carbon-Based Nanomaterials Synthesispotential Valorization of by-Product Materials from Oil

Palm: A Review of Alternative and Sustaina. *Bioresources* **2019**, *14* (1), 2352–2388. https://doi.org/10.15376/biores.14.1.Nasir.

62. Nixon, W. C. The General Principles of Scanning Electron Microscopy. *Philosophical Transactions of the Royal Society of London. B, Biological Sciences* **1971**, *261* (837), 45–50. https://doi.org/10.1098/rstb.1971.0035.

63. Nørskov, J. K.; Bligaard, T.; Logadottir, A.; Kitchin, J. R.; Chen, J. G.; Pandelov, S.; Stimming, U. Trends in the Exchange Current for Hydrogen Evolution. *J Electrochem Soc* **2005**, *152* (3), J23. https://doi.org/10.1149/1.1856988.

64. Orazem, M.E.; Tribollet, B. *Electrochemical Impedance Spectroscopy*.; John Wiley and Sons: 2008.

65. Palmas, S.; Ferrara, F.; Vacca, A.; Mascia, M.; Polcaro, A. M. Behavior of Cobalt Oxide Electrodes during Oxidative Processes in Alkaline Medium. *Electrochim Acta* **2007**, *53*, 400–406. https://doi.org/10.1016/j.electacta.2007.01.085.

66. Pan, L.; Wang, Q.; Li, Y.; Zhang, C. Amorphous Cobalt-Cerium Binary Metal Oxides as High Performance Electrocatalyst for Oxygen Evolution Reaction. *J Catal* **2020**, *384*, 14–21. https://doi.org/10.1016/j.jcat.2020.02.005.

67. Panchu, S. J.; Raju, K.; Swart, H. C. Emerging Two–Dimensional Intercalation Pseudocapacitive Electrodes for Supercapacitors. *ChemElectroChem* **2024**, *11* (15), e202300810. https://doi.org/10.1002/celc.202300810.

68. Pantazis, D. A.; Orio, M.; Neese, F. Density Functional Theory. *Photosynthesis Research* **2009**, *102*, 443–453. https://doi.org/10.1007/s11120-009-9404-8.

69. Pauric, A. D.; Easton, E. B.; MacLean, B. J. Fe-N/C Oxygen Reduction Catalysts Prepared by Surface Functionalization of Carbon Black with 5,6-Diamino,1-10-Phenanthroline. *ECS Trans* **2010**, *28* (23), 55–62. https://doi.org/10.1149/1.3502337.

70. Plevová, M.; Hnát, J.; Bouzek, K. Electrocatalysts for the Oxygen Evolution Reaction in Alkaline and Neutral Media. A Comparative Review. *J Power Sources* **2021**, *507* (March). https://doi.org/10.1016/j.jpowsour.2021.230072.

71. Pope, C. A.; Dockery, D. W. Health Effects of Fine Particulate Air Pollution: Lines That Connect. *J Air Waste Manage Assoc* **2006**, *56* (6), 709–742. https://doi.org/10.1080/10473289.2006.10464485.

72. Prencipe, I.; Dellasega, D.; Zani, A.; Rizzo, D.; Passoni, M. Energy Dispersive X-Ray Spectroscopy for Nanostructured Thin Film Density Evaluation. *Sci Technol Adv Mater* **2015**, *16* (2), 25007. https://doi.org/10.1088/1468-6996/16/2/025007.

73. Qiao, J.; Song, F.; Hu, J.; Huo, D.; Yuan, J. Mesoporous Spinel NiFe Oxide Cubes as Advanced Electrocatalysts for Oxygen Evolution. *Int J Hydrogen Energy* **2019**, *44* (31), 16368–16377. https://doi.org/10.1016/j.ijhydene.2019.04.259.

74. Raveendran, A.; Chandran, M.; Dhanusuraman, R. A Comprehensive Review on the Electrochemical Parameters and Recent Material Development of Electrochemical Water Splitting Electrocatalysts. *RSC Adv* **2023**, *13* (6), 3843–3876. https://doi.org/10.1039/d2ra07642j.

75. Rezaee, B.; Thekkoot, S. R.; Gray, O.; Rajaguru, D.; Tian, J.; Morin, S. Systematic Study of the Effect of Iron in Mixed Transition Metal Spinel Oxides as Oxygen Evolution Electrocatalysts – Electrochemistry and Materials Properties. *In Preparation*.

76. Saddeler, S.; Bendt, G.; Salamon, S.; Haase, F. T.; Landers, J.; Timoshenko, J.; Rettenmaier, C.; Jeon, H. S.; Bergmann, A.; Wende, H.; Roldan Cuenya, B.; Schulz, S. Influence of the Cobalt Content in Cobalt Iron Oxides on the Electrocatalytic OER Activity. *J Mater Chem A Mater* **2021**, *9* (45), 25381–25390. https://doi.org/10.1039/d1ta06568h.

77. Salvatore, D. A.; Dettelbach, K. E.; Hudkins, J. R.; Berlinguette, C. P. Near-Infrared-Driven Decomposition of Metal Precursors Yields Amorphous Electrocatalytic Films. *Sci Adv* **2015**, *1* (2), 2–23. https://doi.org/10.1126/sciadv.1400215.

78. Siegbahn, K. Electron Spectroscopy for Atoms, Molecules and Condensed Matter - an Overview. *Rev Mod Phys* **1982**, *54* (3), 709–727. https://doi.org/10.1016/0368-2048(85)80013-X.

79. Sigle, W. Analytical Transmission Electron Microscopy. *Annu Rev Mater Res* **2005**, *35*, 239–314. https://doi.org/10.1146/annurev.matsci.35.102303.091623.

80. Singh, C.; Mukhopadhyay, S.; Hod, I. Metal–Organic Framework Derived Nanomaterials for Electrocatalysis: Recent Developments for CO2 and N2 Reduction. *Nano Converg* **2021**, *8* (1), 1–10. https://doi.org/10.1186/s40580-020-00251-6.

81. Smith, R. D. L.; Prévot, M. S.; Fagan, R. D.; Trudel, S.; Berlinguette, C. P. Water Oxidation Catalysis: Electrocatalytic Response to Metal Stoichiometry in Amorphous Metal Oxide Films Containing Iron, Cobalt, and Nickel. *J Am Chem Soc* **2013**, *135* (31), 11580–11586. https://doi.org/10.1021/ja403102j.

82. Son, Y. J.; Marquez, R. A.; Kawashima, K.; Smith, L. A.; Chukwuneke, C. E.; Babauta, J.; Mullins, C. B. Navigating IR Compensation: Practical Considerations for Accurate Study of Oxygen Evolution Catalytic Electrodes. *ACS Energy Lett* **2023**, *8* (10), 4323–4329. https://doi.org/10.1021/acsenergylett.3c01658.

83. Staffell, I.; Scamman, D.; Velazquez Abad, A.; Balcombe, P.; Dodds, P. E.; Ekins, P.; Shah, N.; Ward, K. R. The Role of Hydrogen and Fuel Cells in the Global Energy System. *Energy and Environmental Science*. 2019, pp 463–491. https://doi.org/10.1039/c8ee01157e.

84. Stokes, L. C. The Politics of Renewable Energy Policies: The Case of Feed-in Tariffs in Ontario, Canada. *Energy Policy* **2013**, *56*, 490–500. https://doi.org/10.1016/j.enpol.2013.01.009.

85. Thekkoot, S. *Crystalline and Amorphous Cobalt-Based Metal Oxides for Water Oxidation Reaction – Structure, Composition, Morphology and Electrochemical Performance*; Ph.D. Thesis, York University, Toronto, 2024.

86. Thekkoot, S. R. Nanostructured Mixed Transition Metal Spinel Oxide as Efficient Electrocatalysts, Master's Thesis, York University, Toronto, Canada, 2015.

87. Thekkoot, S.; Islam, R.; Gray, O.; Morin, S. Efficiency of Nanostructured CuxCo3-XO4 and NixCu1 –XCo2O4 Electrodes as Electrocatalysts for the Oxygen Evolution Reaction-Revisited. *Electrochim Acta* **2023**, *471*, 143339. https://doi.org/10.7868/s0002337x15010042.

88. Thekkoot, S.; Islam, R.; Morin, S. Improved Oxygen Evolution Reaction Performance with Addition of Fe to Form FeyCux-YCo3-XO4 and FeyNix-YCo3-XO4 (x = 0.5, 1 and y = 0.1, 0.15) Spinel Oxides. *Electrochim Acta* **2021**, *378*, 14–16. https://doi.org/10.1016/j.electacta.2021.138116.

89. Tok, A. I. Y.; Du, S. W.; Boey, F. Y. C.; Chong, W. K. Hydrothermal Synthesis and Characterization of Rare Earth Doped Ceria Nanoparticles. *Materials Science and Engineering A* **2007**, *466*, 223–229. https://doi.org/10.1016/j.msea.2007.02.083.

90. Tougaard, S. Practical Guide to the Use of Backgrounds in Quantitative XPS. *Journal of Vacuum Science & Technology A* **2021**, *39* (1), 11201. https://doi.org/10.1116/6.0000661.

91. Tougaard, S. Universality Classes of Inelastic Electron Scattering Cross-Sections. *Surface and Interface Analysis* **1997**, *25* (3), 137–154. https://doi.org/10.1002/(SICI)1096-9918(199703)25:3<137::AID-SIA230>3.0.CO;2-L.

92. Vajda, E. G.; Skedros, J. G.; Bloebaum, R. D. Errors in Quantitative Backscattered Electron Analysis of Bone Standardized by Energy-Dispersive X-Ray Spectrometry. *Scanning* **1998**, *20*, 527–535.

93. van der Heijden, O.; Park, S.; Vos, R. E.; Eggebeen, J. J. J.; Koper, M. T. M. Tafel Slope Plot as a Tool to Analyze Electrocatalytic Reactions. *ACS Energy Lett* **2024**, *9* (4), 1871–1879. https://doi.org/10.1021/acsenergylett.4c00266.

94. Wang, J.; Cui, W.; Liu, Q.; Xing, Z.; Asiri, A. M.; Sun, X. Recent Progress in Cobalt-Based Heterogeneous Catalysts for Electrochemical Water Splitting. *Advanced Materials* **2016**, *28* (2), 215–230. https://doi.org/10.1002/adma.201502696.

95. Wang, M.; Feng, X.; Li, S.; Ma, Y.; Peng, Y.; Yang, S.; Liu, Y. Spinel-Type Metal Oxides with Tailored Amorphous / Crystalline Heterointerfaces for Enhanced Electrocatalytic Water Splitting. *Adv Func Mater* **2024**, *34*, 2410439. https://doi.org/10.1002/adfm.202410439.

96. World Health Organization. *Ambient (outdoor) air pollution*. World Health Organisation Geneva. https://www.who.int/news-room/fact-sheets/detail/ambient-(outdoor)-air-quality-and-health (accessed 2024-08-23).

97. Xiang, W.; Yang, N.; Li, X.; Linnemann, J.; Hagemann, U.; Ruediger, O.; Heidelmann, M.; Falk, T.; Aramini, M.; DeBeer, S.; Muhler, M.; Tschulik, K.; Li, T. 3D Atomic-Scale Imaging of Mixed Co-Fe Spinel Oxide Nanoparticles during Oxygen Evolution Reaction. *Nat Commun* **2022**, *13* (1), 1–14. https://doi.org/10.1038/s41467-021-27788-2.

98. Xu, D.; Stevens, M. B.; Rui, Y.; DeLuca, G.; Boettcher, S. W.; Reichmanis, E.; Li, Y.; Zhang, Q.; Wang, H. The Role of Cr Doping in Ni–Fe Oxide/(Oxy)Hydroxide Electrocatalysts for Oxygen Evolution. *Electrochim Acta* **2018**, *265*, 10–18. https://doi.org/10.1016/j.electacta.2018.01.143.

99. Yamashita, T.; Hayes, P. Analysis of XPS Spectra of Fe 2+ and Fe 3+ Ions in Oxide Materials. *Appl Surf Sci* **2008**, *254* (8), 2441–2449. https://doi.org/10.1016/j.apsusc.2007.09.063.

100. Yan, S.; Abhilash, K. P.; Tang, L.; Yang, M.; Ma, Y.; Xia, Q.; Guo, Q.; Xia, H. Research Advances of Amorphous Metal Oxides in Electrochemical Energy Storage and Conversion. *Small* **2019**, *15* (4), 1–30. https://doi.org/10.1002/smll.201804371.

101. Yang, Q.; Li, X.; Zhao, L.; Wang, G.; Guo, Z.; Niu, K.; Jiang, S.; Hou, F.; Lin, J.; Yang, Q.; Li, X.; Zhao, L.; Wang, G.; Guo, Z.; Niu, K.; Jiang, S.; Hou, F.; Lin, J. Unified Transmission Electron Microscopy with the Glovebox Integrated System for Investigating Air-Sensitive Two-Dimensional Quantum Materials. *The Innovation* **2025**, *6* (1), 100751. https://doi.org/10.1016/j.xinn.2024.100751.

102. Yano, J.; Yachandra, V. K. X-Ray Absorption Spectroscopy. *Photosynthesis Research* **2009**, *102*, 241–254. https://doi.org/10.1007/s11120-009-9473-8.

103. Yoshida, Y.; Langouche, G. *Mössbauer Spectroscopy*; Springer-Verlag Berlin Heidelberg, **2013**.

104. Yousaf, S.; Zulfiqar, S.; Khalid, M. U.; Warsi, M. F.; Shakir, I.; Shahid, M.; Ahmad, I.; Cochran, E. W. Beyond the Ordinary: Exploring the Synergistic Effect of Iodine and Nickel Doping in Cobalt Hydroxide for Superior Energy Storage Applications. *RSC Adv* **2024**, *14* (24), 16661. https://doi.org/10.1039/D4RA01907E.

105. Zhao, Q.; Yan, Z.; Chen, C.; Chen, J. Spinels : Controlled Preparation , Oxygen Reduction / Evolution Reaction Application, and Beyond. *Chem Rev* **2017**, *117* (15), 10121–10211. https://doi.org/10.1021/acs.chemrev.7b00051.

106. Zheng, W. IR Compensation for Electrocatalysis Studies: Considerations and Recommendations. *ACS Energy Lett* **2023**, *8*, 1952–1958. https://doi.org/10.1021/acsenergylett.3c00366.

107. Zhu, S.; Wang, X.; Le, J.; An, N.; Li, J.; Liu, D.; Kuang, Y. Striking Stabilization Effect of Spinel Cobalt Oxide Oxygen Evolution Electrocatalysts in Neutral PH by Dual-Sites Iron Incorporation. *Energy and Environmental Materials* **2024**, *7* (2), 1–9. https://doi.org/10.1002/eem2.12594.

Appendix 1. Supporting documents for Chapter 4.1 Structural Characterization

In this section more figures and graphs are shown such as SEM images, EDX graphs and XPS spectra that couldn't fit into the main text of Chapter 4.1 to make the length manageable.

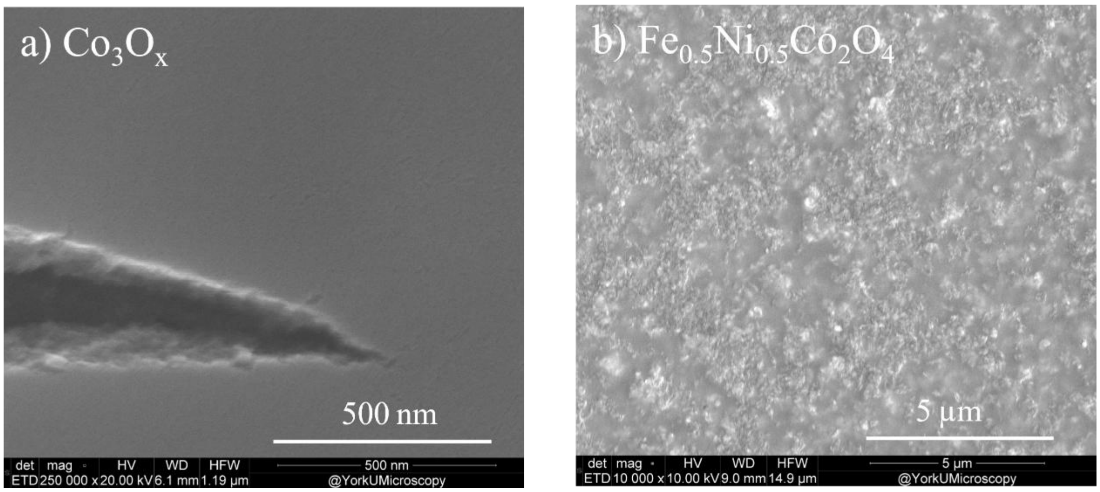

Figure A1.1. Scanning electron microscopy images a) amorphous Co_3O_x with a magnification of 250000X and b) spinel $Fe_{0.5}Ni_{0.5}Co_2O_4$ with a magnification of 10000X.

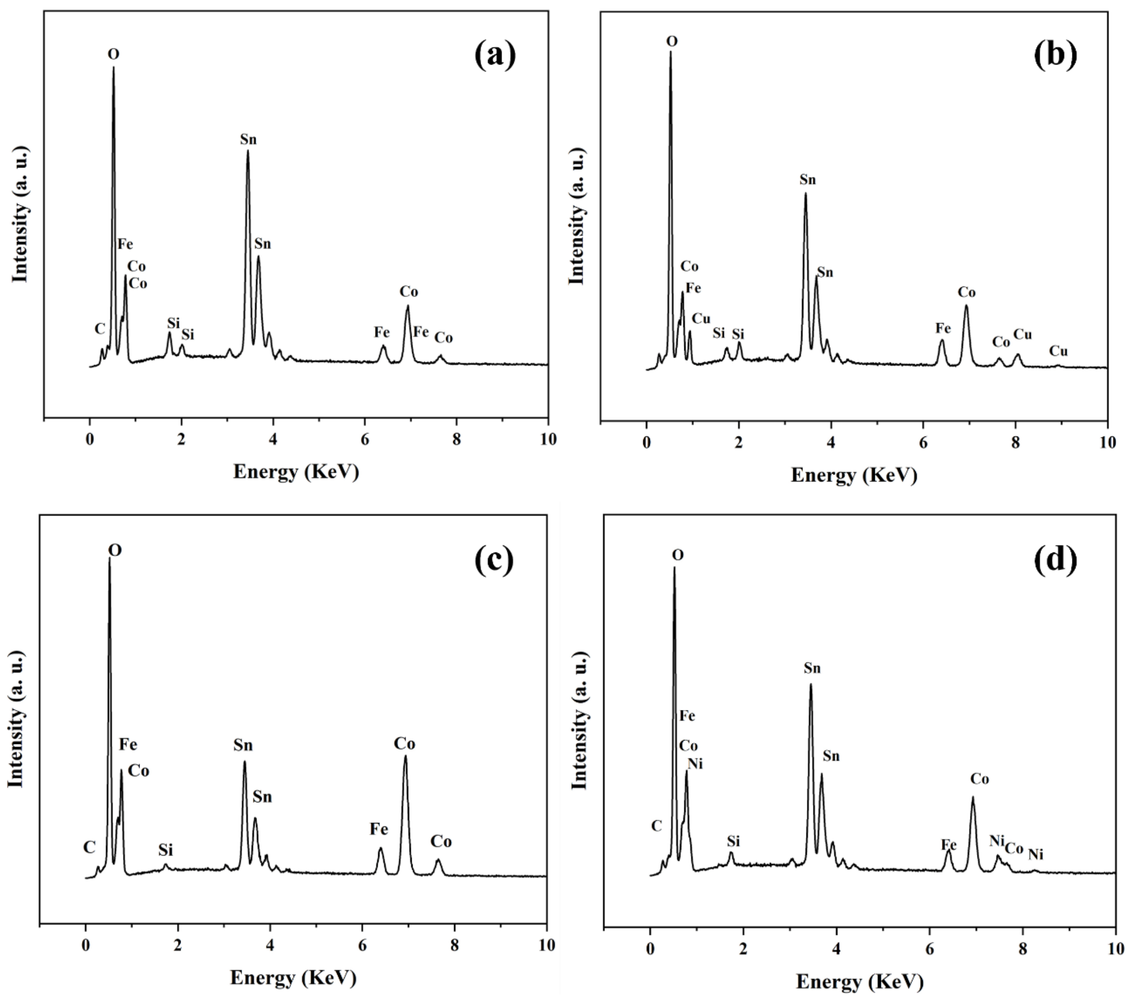

Figure A1.2. EDX spectra of a) $Fe_{0.5}Co_{2.5}O_x$, b) $Fe_{0.5}Cu_{0.5}Co_2O_x$, c) $Fe_{0.5}Co_{2.5}O_4$, and d) $Fe_{0.5}Ni_{0.5}Co_{2.5}O_4$

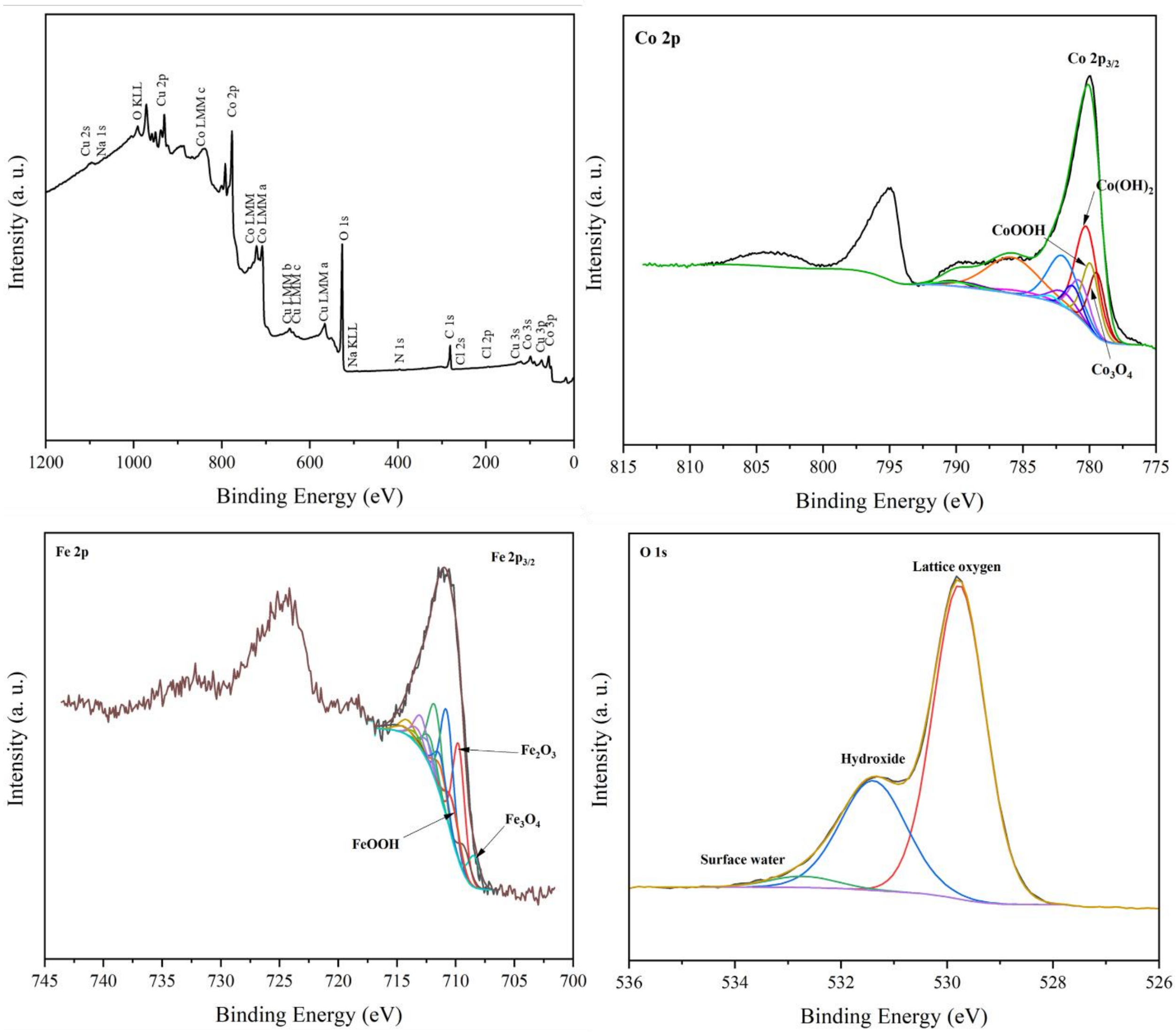

Figure A1. 3. XPS spectra of $Fe_{0.5}Cu_{0.5}Co_2O_4$ including survey spectrum and high-resolution spectra of Co 2p, Fe 2p, and O 1s

Table A1. Spectral fitting parameters of Co 2p, Fe 2p and O 1s for $Fe_{0.5}Co_{2.5}O_4$ electrode

		Peak1	FWHM	Peak2	FWHM	Peak3	FWHM	Peak4	FWHM	Peak5	FWHM
Co 2p	$Co(OH)_2$	780.45	1.94	782.25	2.65	786.04	4.57	790.44	2.23		
	Co_3O_4	779.70	1.49	781.00	1.65	782.30	2.08	785.30	4.54	789.60	3.39
	CoO	780.20	2.24	782.30	2.66	785.70	2.29	785.70	4.98		
	CoOOH	780.20	1.48	781.52	1.48	783.20	1.48	790.28	3.30		
O 1s		530.00	1.02	531.25	1.49	532.72	1.49				
Fe 2p	Fe_2O_3	709.75	1.20	710.75	1.30	711.75	1.40	712.95	1.40	714.05	1.70
	Fe_3O_4 (Fe^{2+})	708.35	1.20	709.15	1.20						
	Fe_3O_4 (Fe^{3+})	710.15	1.40	711.15	1.40	712.25	1.40	713.35	1.40	714.45	3.30
	FeOOH	710.30	1.40	711.30	1.30	712.20	1.40	713.30	1.40	714.40	1.80

Table A2. Spectral fitting parameters of Co 2p, Fe 2p, Cu 2p and O 1s for $Fe_{0.5}Co_{2.5}O_4$ electrode

		Peak1	FWHM	Peak2	FWHM	Peak3	FWHM	Peak4	FWHM	Peak5	FWHM
Co 2p	$Co(OH)_2$	780.20	2.14	782.00	2.65	785.79	4.57	790.19	2.23		
	Co_3O_4	779.56	1.49	780.86	1.72	782.16	2.28	785.16	4.54	789.46	3.39
	CoOOH	779.90	1.48	781.22	1.48	782.90	1.48	789.97	3.30		
O 1s		529.77	1.16	531.39	1.48	532.72	1.48				
Fe 2p	Fe_2O_3	709.75	1.20	710.75	1.30	711.75	1.40	712.95	1.40	714.05	1.70
	Fe_3O_4 (Fe^{2+})	708.35	1.20	709.25	1.20						
	Fe_3O_4 (Fe^{3+})	710.25	1.40	711.25	1.40	712.35	1.40	713.45	1.40	714.55	3.30
	FeOOH	710.30	1.40	711.30	1.30	712.20	1.40	713.30	1.40	714.40	1.80
Cu 2p	Cu_2O	932.62	1.52								
	CuO	933.31	2.07	934.68	3.05	940.72	1.03	941.85	1.13	943.90	1.17
	$Cu(OH)_2$	934.67	2.85	939.30	2.80	942.20	3.66	944.12	1.76		
	Cu spinel	940.46	2.65	943.53	2.26	936.60	3.00	934.15	1.94		

Appendix 2. Supporting documents for Chapter 4.2 Material Electrochemical Characterization

In this section CVs of eight electrodes (Co_3O_x, $Fe_{0.5}Co_{2.5}O_x$, $Fe_{0.5}Cu_{0.5}Co_2O_x$, $Fe_{0.5}Ni_{0.5}Co_2O_x$, $Fe_{0.5}Cu_{0.5}Co_2O_4$, $Fe_{0.5}Ni_{0.5}Co_2O_4$, Co_3O_4-300, Co_3O_4-400) and their cathodic current density plots. Moreover, Nyquist plots of these spinel and amorphous oxide electrodes are shown in this section to keep the length of the main text of Chapter 4.2 manageable.

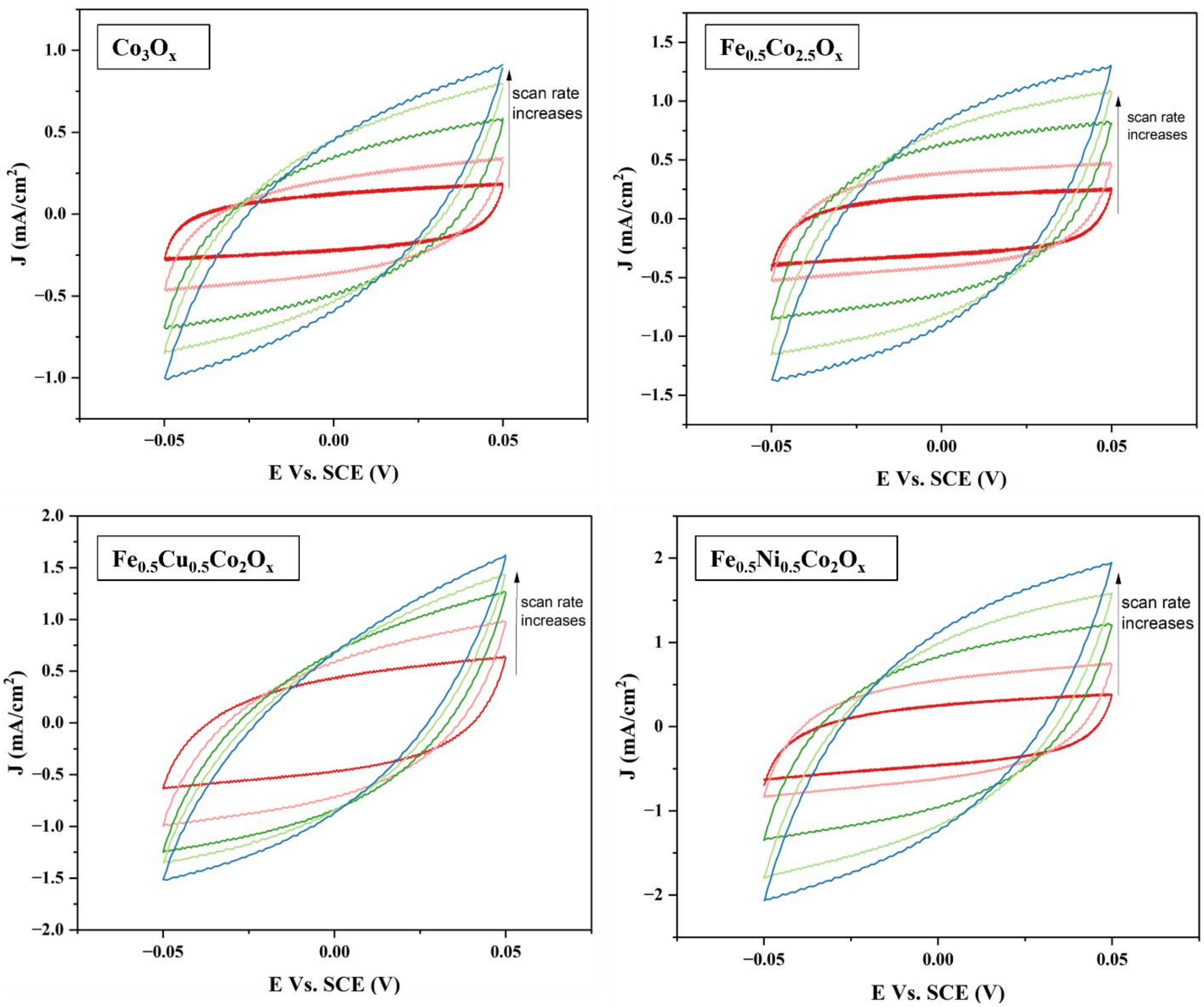

Figure A2.1. Cyclic voltammograms of the amorphous electrodes prepared in this work for the potential range of -50 mV to 50 mV (SCE) at different scan rates and in 1M KOH.

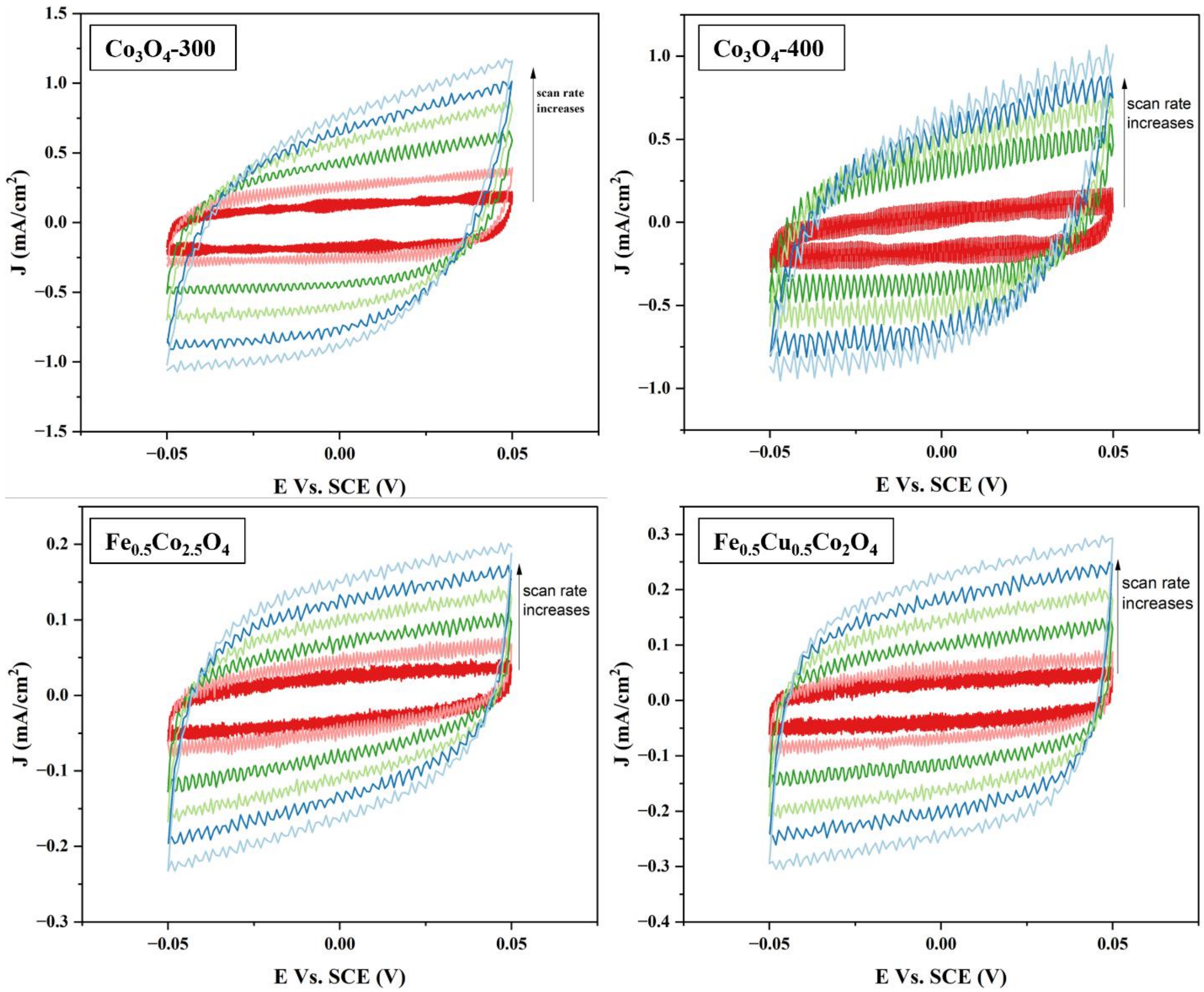

Figure A2. 2. Cyclic voltammograms of crystalline electrodes prepared in this work for the potential range of -50 mV to 50 mV (SCE) at different scan rates and in 1M KOH.

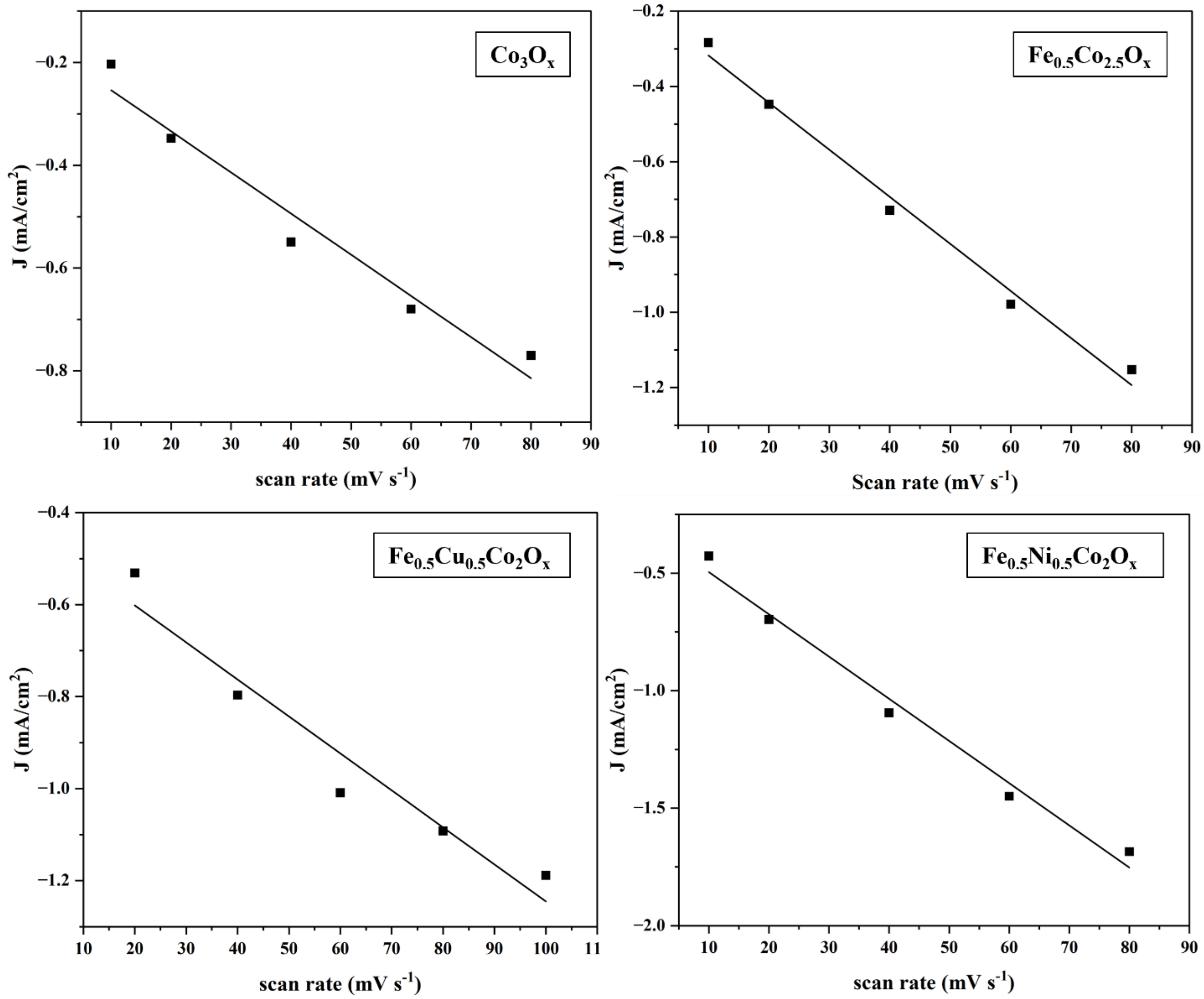

Figure A2. 3. Plots of cathodic current density versus scan rate at potential -25 mV (SCE) for amorphous electrodes prepared in this work.

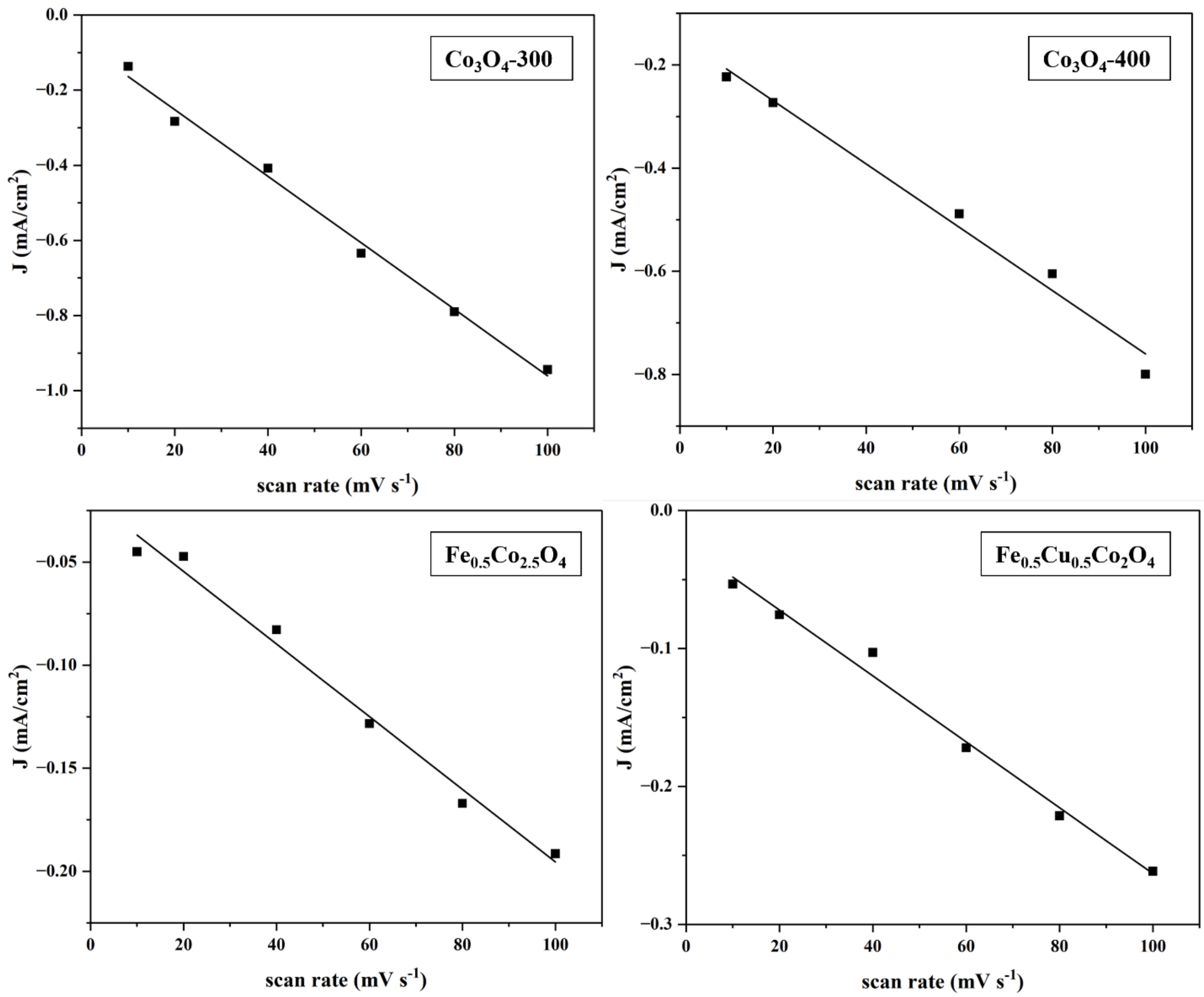

Figure A2. 3. Plots of cathodic current density versus scan rate at potential -25 mV (SCE) for spinel electrodes prepared in this work.

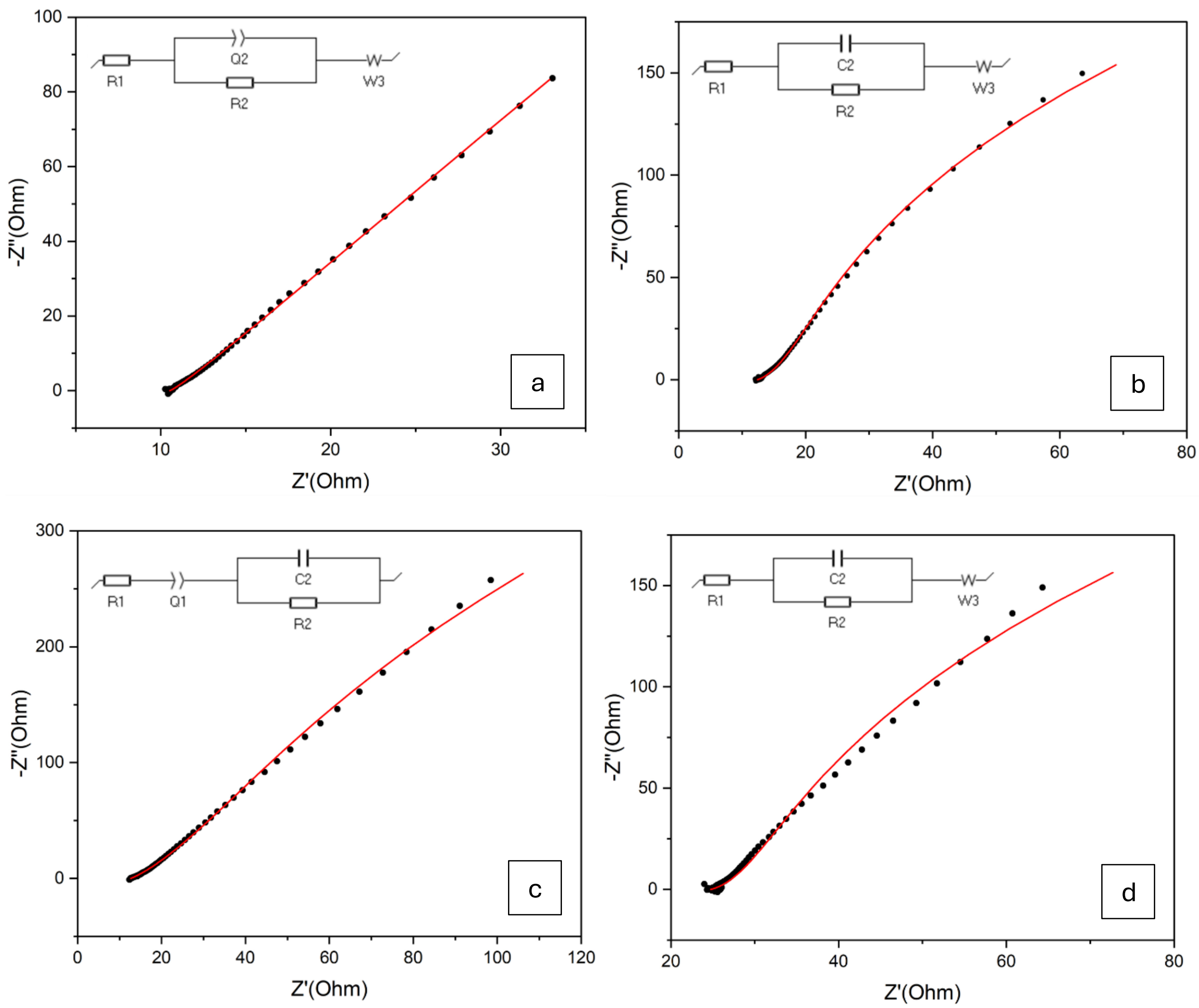

Figure A2. 4. Nyquist plots for spinel oxides a) Co_3O_4-300 °C, b) Co_3O_4-400 °C, c) $Fe_{0.5}Cu_{0.5}Co_2O_4$, d) $Fe_{0.5}Ni_{0.5}Co_2O_4$. The impedance is obtained at 0V in 1M KOH solution. The measured data are shown with black dots while the simulated fit is shown with red line with their respected circuits being displayed as an inserted picture in each graph.

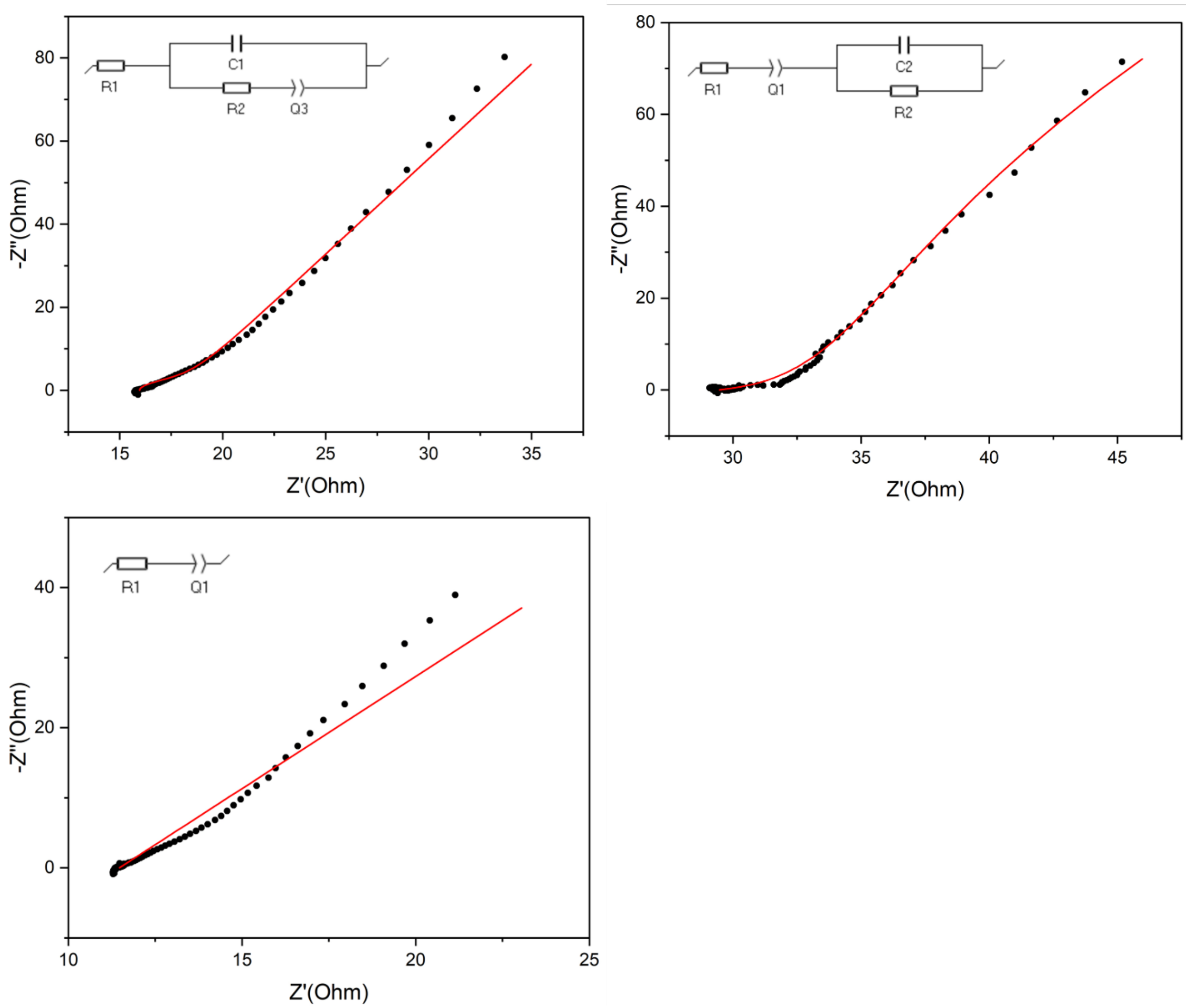

Figure A2. 5. Nyquist plots for amorphous oxides a) $Fe_{0.5}Co_{2.5}O_x$, b) $Fe_{0.5}Cu_{0.5}Co_2O_x$, c) $Fe_{0.5}Ni_{0.5}Co_2O_x$. The impedance is obtained at 0V in 1M KOH solution. The measured data are shown with black dots while the simulated fit is shown with red line with their respected circuits being displayed as an inserted picture in each graph.

Appendix 3. Supporting documents for Chapter 4.3 Electrocatalytic Properties

CVs of all electrodes (except $Fe_{0.5}Co_{2.5}O_4$) and Tafel slopes of three spinel electrodes (Co_3O_4, $Fe_{0.5}Cu_{0.5}Co_2O_4$, $Fe_{0.5}Ni_{0.5}Co_2O_4$) are shown here to keep the length of Chapter 4.3 manageable.

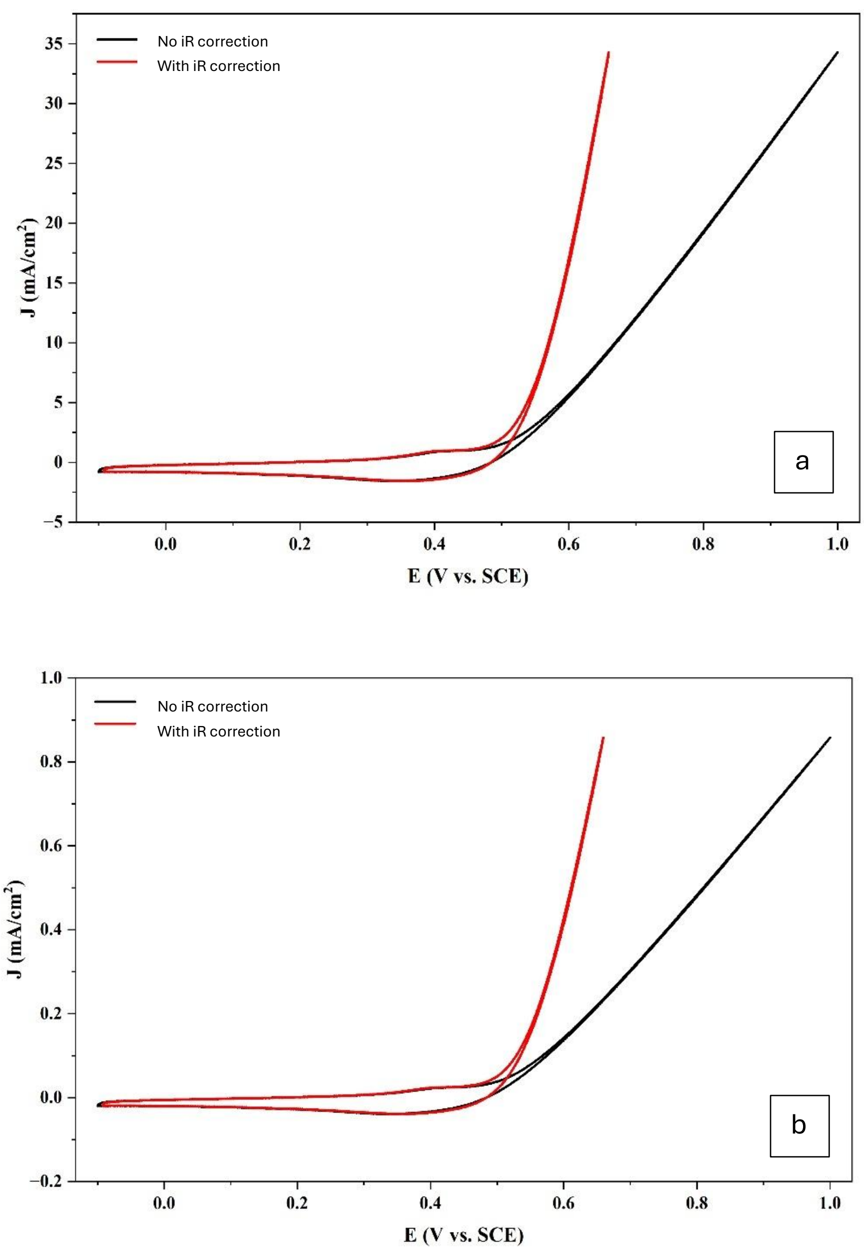

Figure A3.1. Cyclic voltammograms of $Fe_{0.5}Cu_{0.5}Co_2O_4$ electrode corrected for iR drop measured at 1M KOH at scan rate of 50 $mVs^{-1}$and a) geometric area b) real surface area (roughness factor).

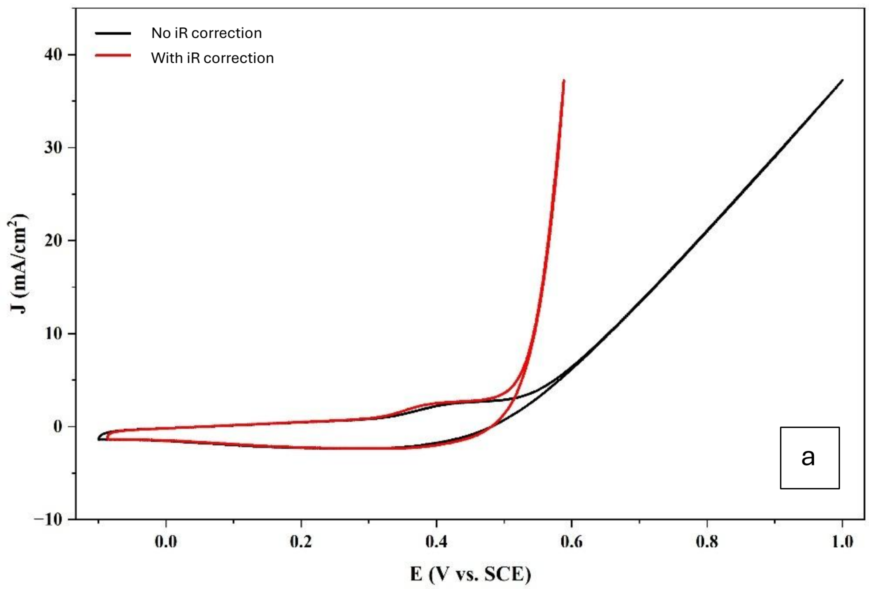

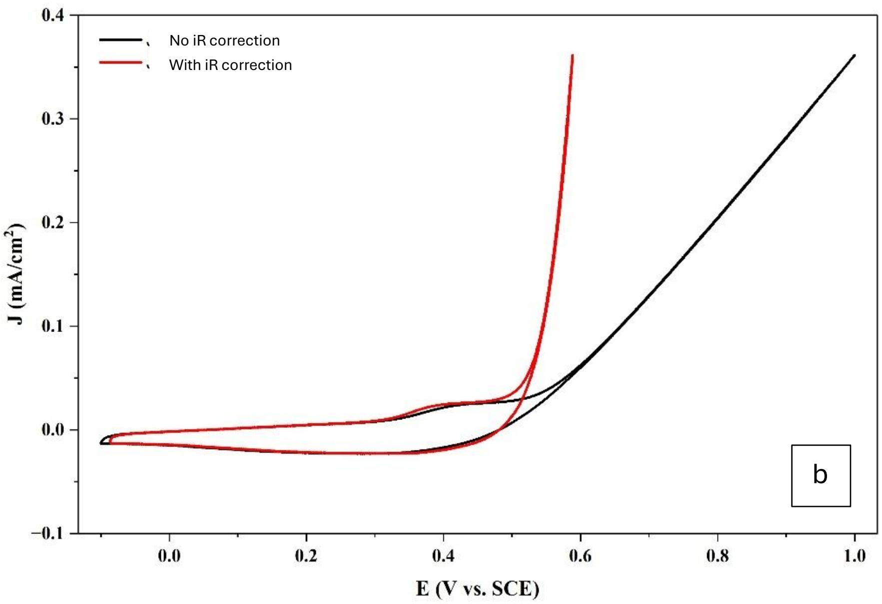

Figure A3.2. Cyclic voltammograms of $Fe_{0.5}Ni_{0.5}Co_2O_4$ electrode corrected for iR drop measured at 1M KOH at scan rate of 50 $mVs^{-1}$and a) geometric area b) real surface area (roughness factor).

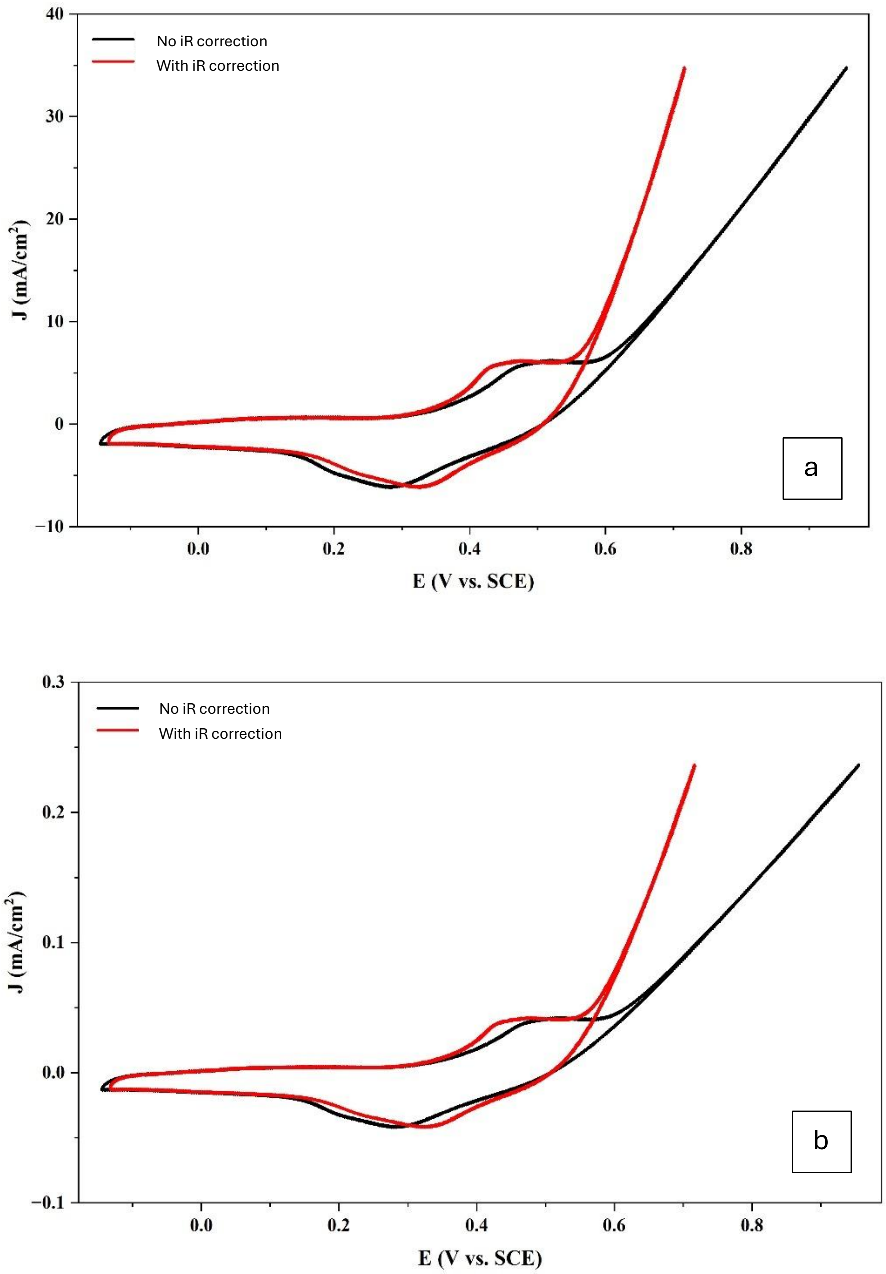

Figure A3.3. Cyclic voltammograms of Co_3O_4 – 300 °C electrode corrected for iR drop measured at 1M KOH at scan rate of 50 mVs^{-1}and a) geometric area b) real surface area (roughness factor).

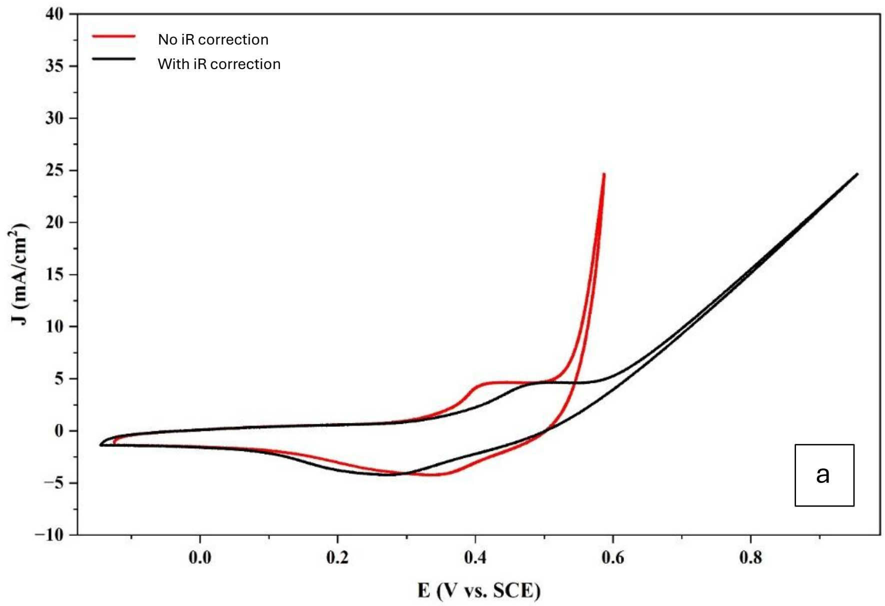

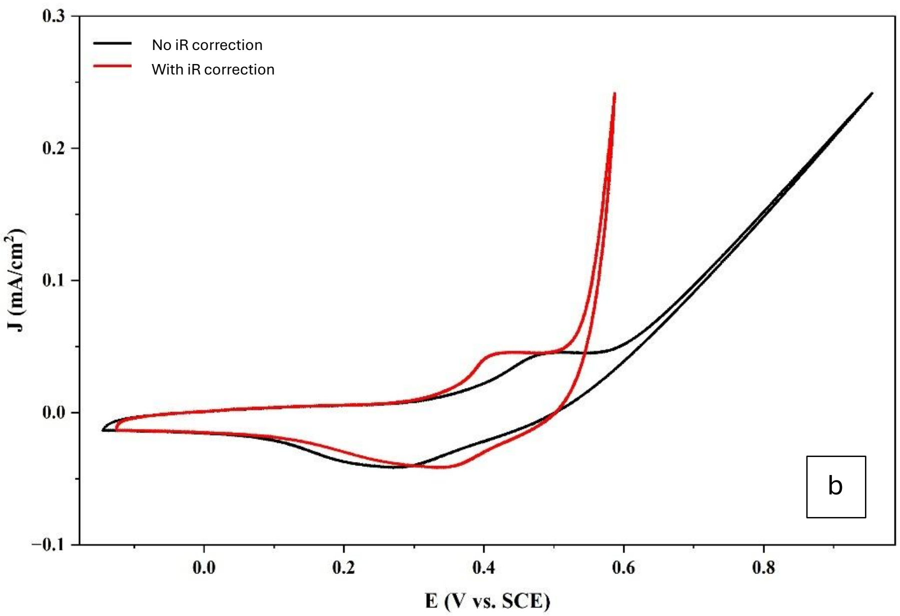

Figure A3.4. Cyclic voltammograms of Co_3O_4 – 400 °C electrode corrected for iR drop measured at 1M KOH at scan rate of 50 mVs^{-1}and a) geometric area b) real surface area (roughness factor).

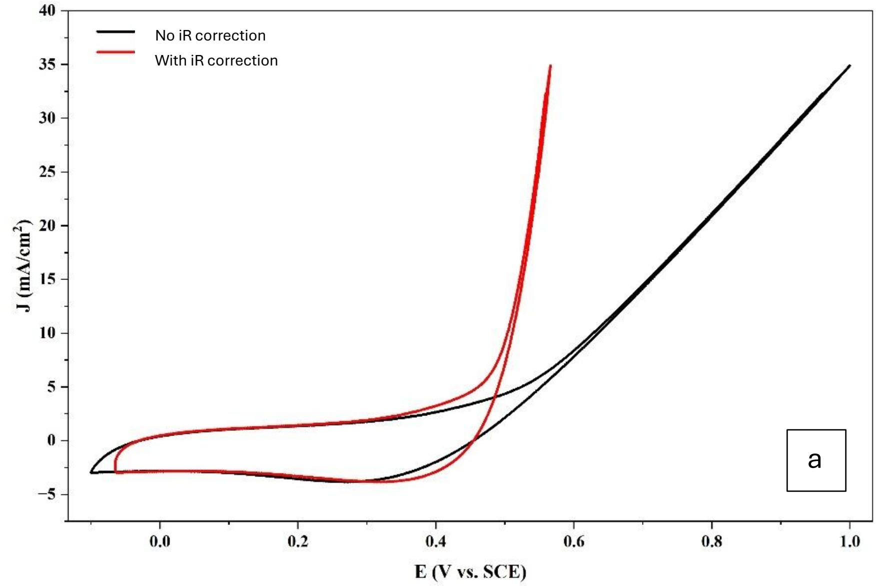

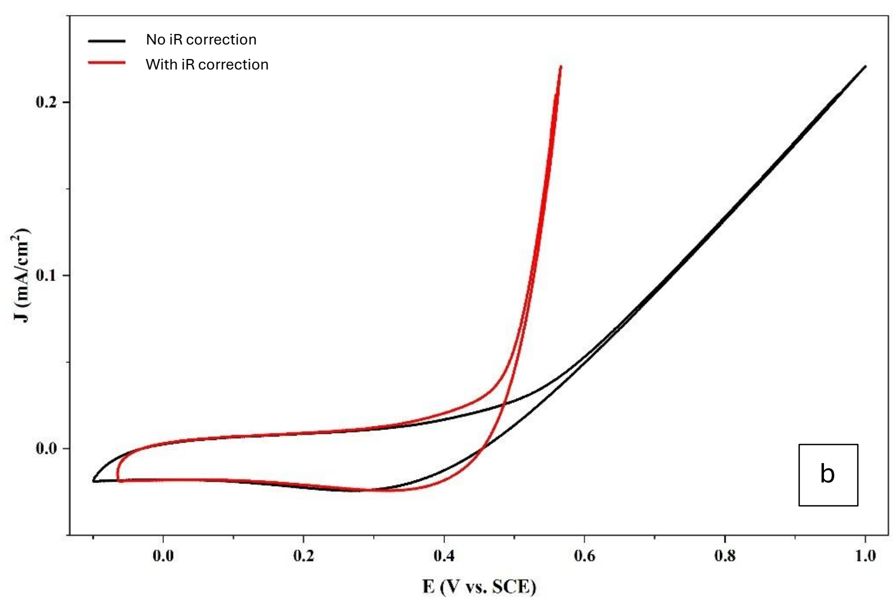

Figure A3.5. Cyclic voltammograms of $Fe_{0.5}Co_{2.5}O_x$ electrode corrected for iR drop measured at 1M KOH at scan rate of 50 $mVs^{-1}$and a) geometric area b) real surface area (roughness factor).

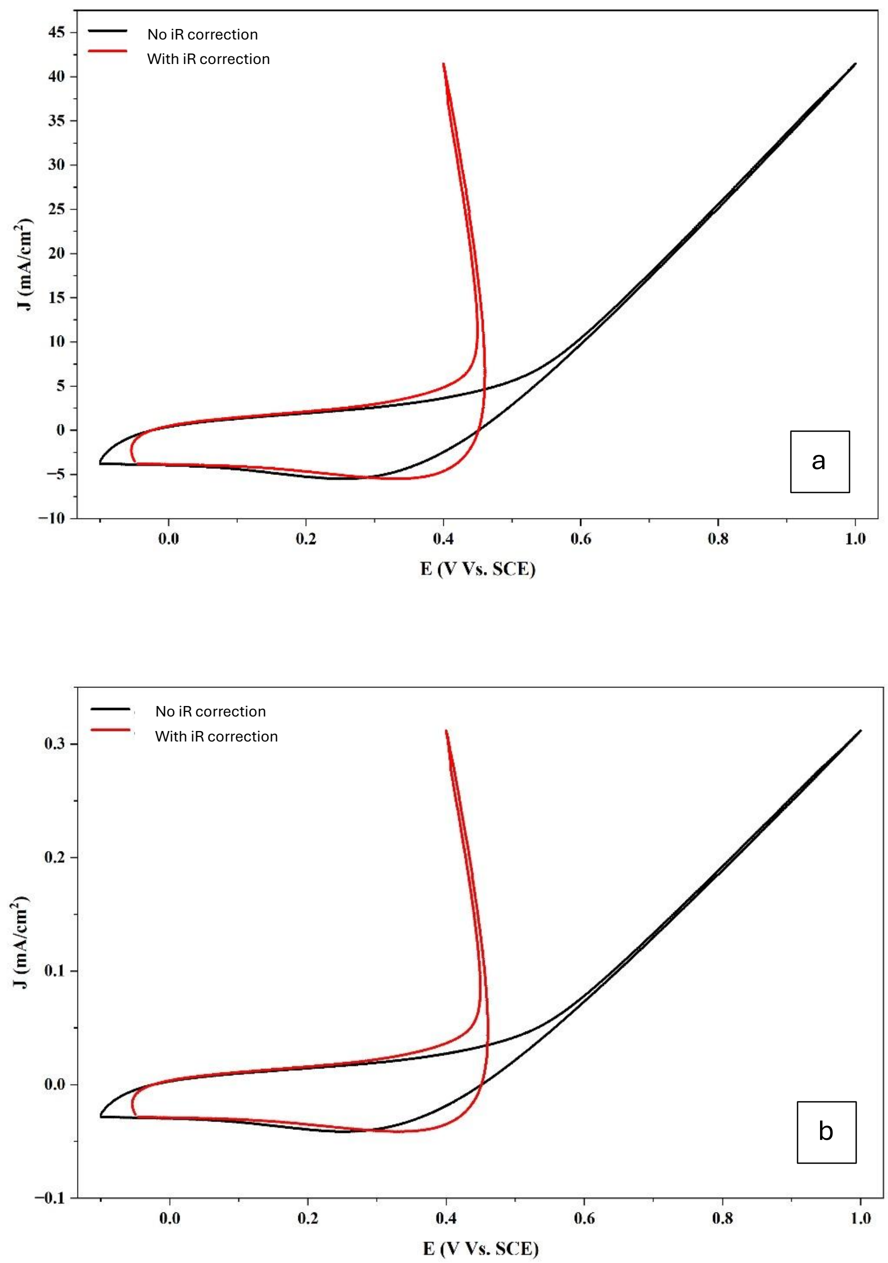

Figure A3.6. Cyclic voltammograms of $Fe_{0.5}Cu_{0.5}Co_2O_x$ electrode corrected for iR drop measured at 1M KOH at scan rate of 50 mVs^{-1}and a) geometric area b) real surface area (roughness factor).

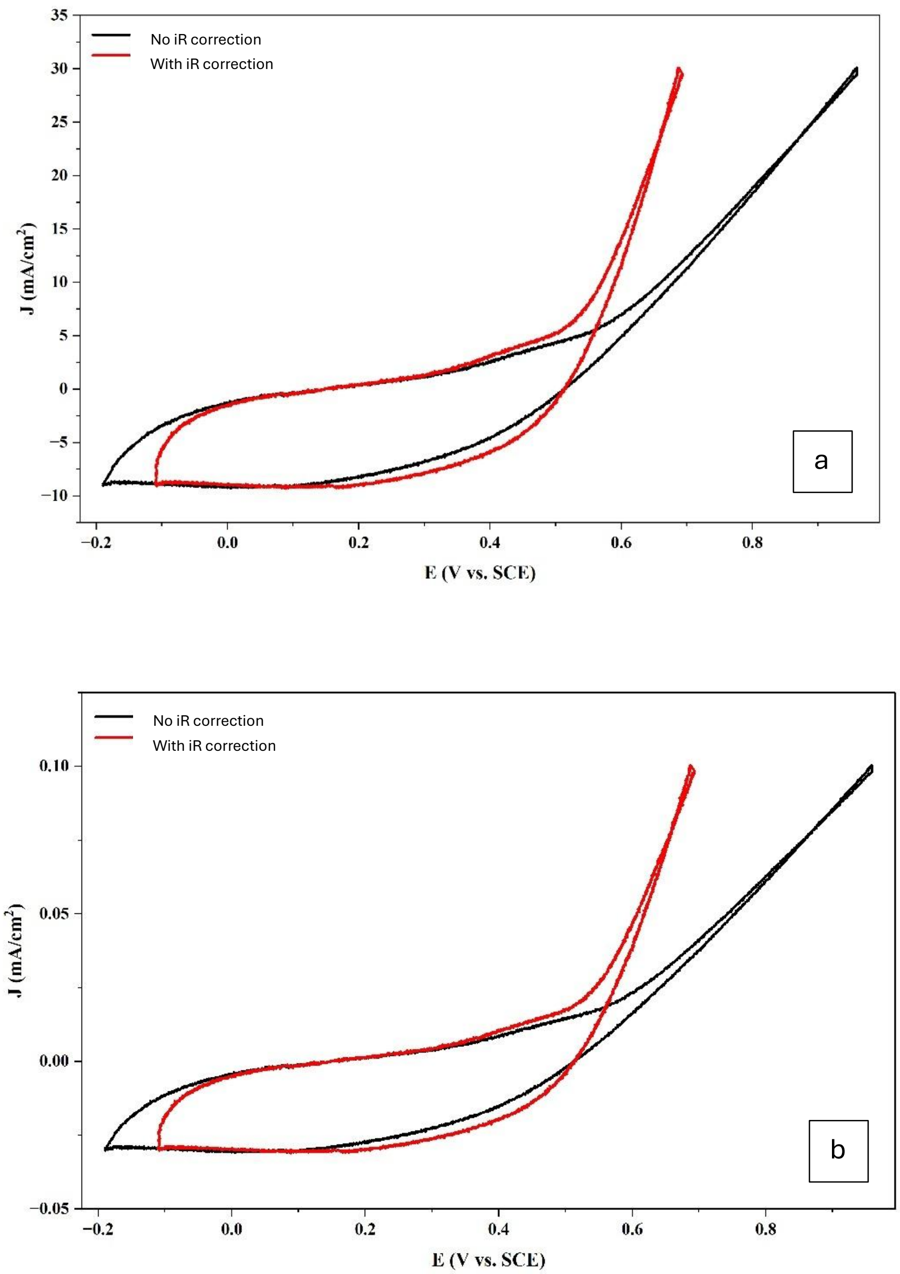

Figure A3.7. Cyclic voltammograms of $Fe_{0.5}Ni_{0.5}Co_2O_x$ electrode corrected for iR drop measured at 1M KOH at scan rate of 50 $mVs^{-1}$and a) geometric area b) real surface area (roughness factor).

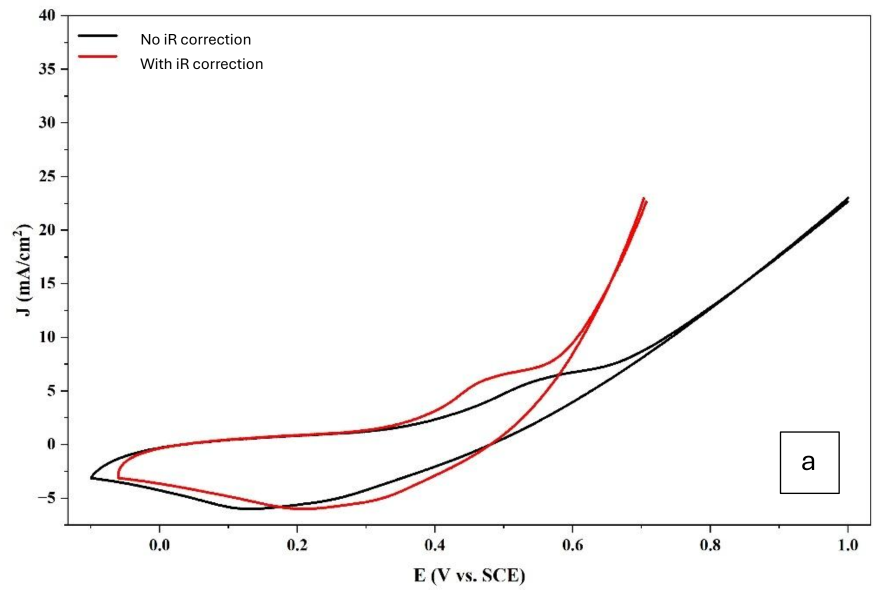

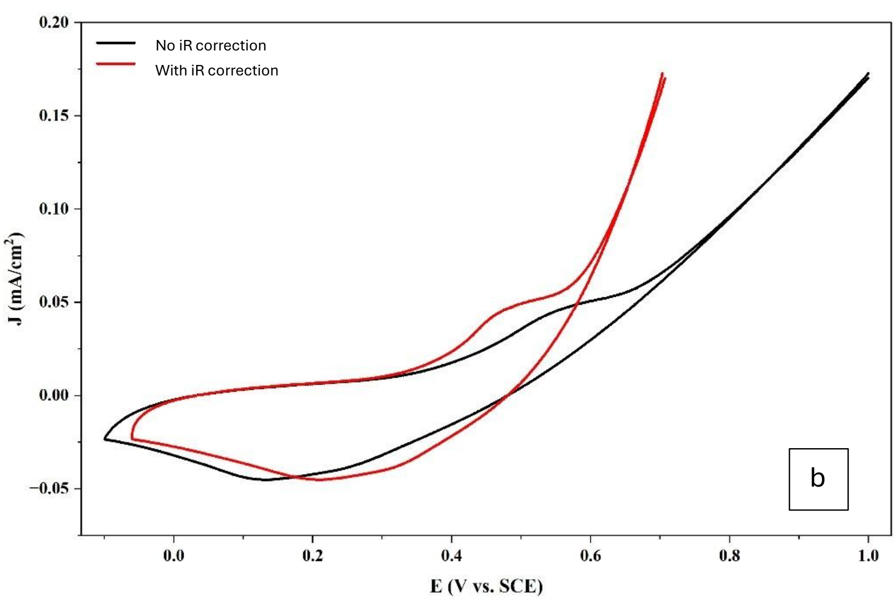

Figure A3.8. Cyclic voltammograms of Co_3O_x electrode corrected for iR drop measured at 1M KOH at scan rate of 50 $mVs^{-1}$and a) geometric area b) real surface area (roughness factor).

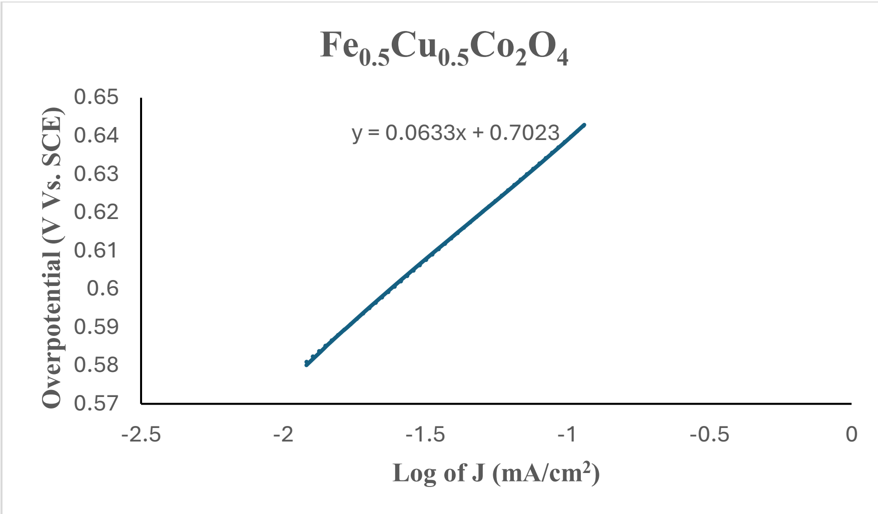
$Fe_{0.5}Cu_{0.5}Co_2O_4$
y = 0.0633x + 0.7023
Overpotential (V Vs. SCE)
0.65
0.64
0.63
0.62
0.61
0.6
0.59
0.58
0.57
-2.5
-2
-1.5
-1
-0.5
0
Log of J (mA/cm^2)

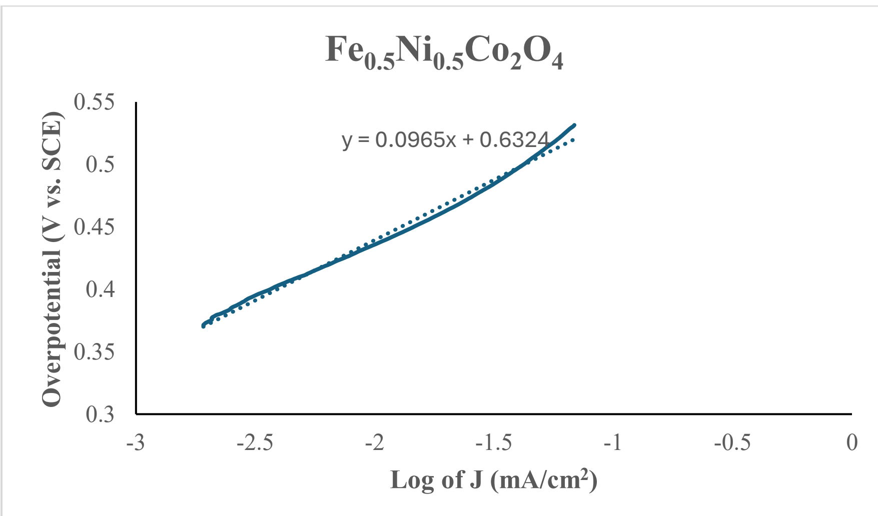
$Fe_{0.5}Ni_{0.5}Co_2O_4$
y = 0.0965x + 0.6324
Overpotential (V vs. SCE)
0.55
0.5
0.45
0.4
0.35
0.3
-3
-2.5
-2
-1.5
-1
-0.5
0
Log of J (mA/cm^2)

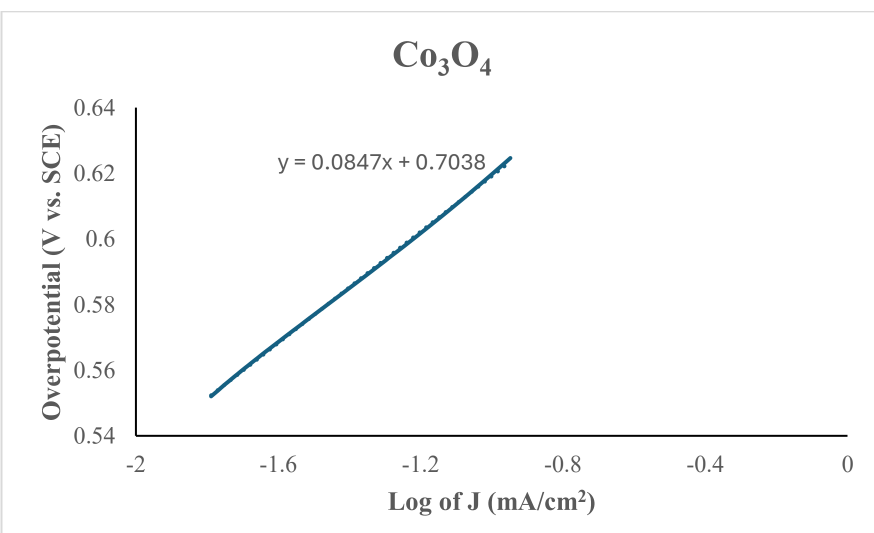
Co_3O_4
y = 0.0847x + 0.7038
Overpotential (V vs. SCE)
0.64
0.62
0.6
0.58
0.56
0.54
-2
-1.6
-1.2
-0.8
-0.4
0
Log of J (mA/cm^2)

Figure A3. 9. Tafel slopes of the spinel electrodes in 0.1 M KOH solution at 3000 rpm where the potential is corrected for iR drop.